University College London

Computational Studies of the Interaction of Pollutants with Iron Oxide Surfaces

Thesis submitted for the degree of Doctor of Philosophy (PhD) by

Asmaa Yahya Ibraheam Al-Baitai

Supervisor:

Prof. Nora H. de Leeuw

University College London

Department of Chemistry

November 2011

Declaration

I, Asmaa Yahya Ibraheam Al-Baitai confirm that the work presented in this thesis is the result of my own investigations and where information has been derived from other sources, this has been fully acknowledged.

Asmaa Yahya Ibraheam Al-Baitai

November 2011

Abstract

The broad aim of the work in this thesis is to apply atomistic simulation techniques to advance our understanding of the surface chemistry of two important iron oxide minerals, hematite (α-Fe_2O_3) and maghemite (γ-Fe_2O_3), which have important applications in many fields, including as remedial agents in the soil and catalysts.

First we have compared several interatomic potential models to describe the structures and properties of four iron oxide polymorphs, namely α-Fe_2O_3(hematite), β-Fe_2O_3, γ-Fe_2O_3 (maghemite) and ε-Fe_2O_3 to choose a suitable potential for these systems, where we have considered cell volume, angles, Fe-O bond distances and relative stabilities of the four polymorphs. Next, we have investigated the energetic of vacancy ordering in γ-Fe_2O_3 (maghemite), using a statistical approach to evaluate uptake and ordering as a function of temperature. Our results show clearly that full vacancy ordering, in a pattern with space group $P4_12_12$, is the thermodynamically preferred situation in the bulk material. This stability arises from a minimal Coulombic repulsion between Fe^{3+} cation sites for this configuration. Using this ordered model for maghemite, we have studied the surfaces of hematite (α-Fe_2O_3) and maghemite (γ-Fe_2O_3) both in dehydrated and hydroxylated form, and their interactions with two organic molecules, namely methanoic acid and hydroxyethanal, as models of organic pollutants. Finally, we have also considered the interaction of the same mineral surfaces with arsenate, another toxic pollutant found in soils and groundwater.

Table of Contents

Acknowledgments

First I want to thank my supervisor, Prof. Nora de Leeuw, for a great deal of support throughout my research years. I would also like to thank her for the great interest she took in my progress, and her enormous help and guidance during the writing of my thesis. I would not have been able to complete this work without her support.

I am also indebted to my second supervisor Dr Robert Bell for his support, and for useful discussions regarding my project.

Special mention should also go to Dr. Iman Saadoune and Dr. Ricardo Grau-Crespo for their invaluable help and guidance in the first year, Prof. Afaf Al Derzi and Mr Abbas Al-Shukry for their invaluable help, guidance and all their patience since I was in Iraq until now. Thank you also to Dr. Zhimei Du for her help, suggestions and guidance in the last years.

I would also like to thank the following people: Dr. Devis Di Tommaso, Dr. Neyvis Almora-Barrios, Dr. Donald Mikhonto and Dr. Alberto Roldan for their advice, conversation and encouragement, and other past and present members of Prof. de Leeuw's group. I am also grateful to all the members of the Embassy of the Republic of Iraq, Cultural office, especially Mr Ahmad Al-Baghdadi and Mr Ali Al-Rubaiy.

I am very grateful for the UCL Overseas Research Studentship and the Scholarship from the Ministry of Higher Education and Scientific Research in

Iraq, which generously provided the funds for the execution of this project and for my university fees and maintenance.

I am very grateful to my mum, sisters, brothers for their love, guidance and encouragement. All of you have been super and I hope this thesis makes you proud. A special thanks to my dad, although he has died, but his warmth and support was always there when I needed it most.

Finally, I would like to thank my husband Saifaldeen M. Abdalhadi without whose love and understanding I would never have completed my Ph.D. I shall dedicate this thesis to all my family and my first baby (Yousuf “Joseph”) whose arrival I am expecting soon.

List of Publications

(1) Journal

Ricardo Grau-Crespo, Asmaa Y Al-Baitai, Iman Saadoune and Nora H De Leeuw(2010). "Vacancy ordering and electronic structure of γ-Fe_2O_3 (maghemite): a theoretical Investigation". Journal of Physics: Condensed Matter, 22, 255401.

(2) Conferences (Oral presentation)

Spring Course 2008: Writing Workshop, Carcassonne, France, 4-9 May (2008). Computer Modelling of the Structure and Properties of Maghemite γ-Fe_2O_3 .

(3) Conferences (poster presentation)

CCP5 Summer School, Sheffield, United Kingdom, 5-14 July (2009). Computational Study of Maghemite γ-Fe_2O_3 .

Thermodynamics and Kinetics of Surfaces and Interfaces from Simulations. Thomas Young Centre (TYC) Workshop, University College London, UK 22June (2011) A computational Study of the Adsorption of Arsenate at Iron Oxide Surfaces.

Chapter 1

Introduction

This chapter introduces the main reasons for the research presented in this thesis. Iron oxide surface processes are of considerable importance in different fields, and it is therefore of interest to further our knowledge of surface reactions. This goal requires the most advanced experimental techniques and theoretical descriptions available: spectroscopy, computational chemistry and kinetic mechanisms. In this thesis we focus on the study of the structural properties and the surface reactivity of a number of iron oxide polymorphs and, in particular hematite (α-Fe_2O_3) and maghemite (γ-Fe_2O_3), using computational techniques, which can be an important support for experimental researchers.

1.1 Iron Oxides

1.1.1 Background

Iron oxides and hydroxides are among the most widespread metal oxides. These are of interest in a variety of scientific disciplines for applications in many scientific and industrial fields, including, environmental applications, corrosion, soil science and biology (Schwertmann & Cornell, 2000). The polymorphic nature of iron oxides has been known for a long time, and fifteen iron oxides, oxide

hydroxides and hydroxides are known to date. The polymorphs which are most frequently found in the nature as minerals are hematite (α-Fe_2O_3) and maghemite (γ-Fe_2O_3), which are introduced from the Earth's crust during rock weathering and are present in soils, rocks, lakes, rivers and seas. Other polymorphs, including beta (β-Fe_2O_3) and epsilon (ε-Fe_2O_3), as well as the nanoparticles of all forms have been synthesised and extensively investigated in recent years.

1.1.2 Applications of Iron Oxides

Iron oxides are important materials in catalysis (Twigg, 1989; Lei *et al*., 2005), where both hematite and maghemite are used as catalysts of industrial reactions. For example, in the manufacture of styrene through dehydrogenation of ethylbenzene hematite/K_2O is used as the catalyst (Mimura *et al*., 1998; Zscherpel *et al*., 1997; Chang *et al*., 1997; Jiang *et al*., 1998) whereas Fischer-Tropsch synthesis of hydrocarbons (Xu *et al*., 1994; Huang *et al*., 1993; Jung & Thomson, 1993) is also catalysed by Fe_2O_3.

Iron oxides are also important as pigments, where the natural and synthetic pigments are used in the manufacture of red, brown, and black paints or as admixtures, for example, in colored glasses (Mendoza *et al*., 1990; Morsi & El-Shennawi, 1993; Burkhard, 1997). However, the major synthetic iron oxide pigments are yellow (goethite), oranges (lepidocrocite), red (hematite), brown (maghemite) and black (magnetite).

Other industrial applications of iron oxides, are as magnetic devices (Suber *et al*., 2005; Xiong *et al*., 2008), or semiconductors, when the iron oxide can be incorporated into the interlayer of layered compounds as semiconductor pillars which show excellent photocatalytic activity(Fujishiro *et al*., 1999). Due to their hardness , iron oxides have been used as polishing agents for example, the lightly calcined form of hematite (Jeweler's rouge) is used to polish gold and silver, while a more strongly calcined hematite (crocus) serves to polish brass and steel (Schwertmann & Cornell, 2000).

Applications of iron oxides in soil science are their implementation as adsorbents of organic and inorganic compounds in the soil and sediments (Schwertmann &Cornell, 2000) for example, in water treatment. For example, iron-oxide coated sand filtration is one of the most viable technological methods for arsenic removal from drinking water in the United States.

1.1.3 Structure and Properties of Iron Oxides

Hematite (α-Fe_2O_3)

Hematite (α-Fe_2O_3) is the most stable iron oxide with a high resistance to corrosion, low cost, and non-toxicity, and it is the most common iron oxide mineral in nature. The crystal structure of hematite was determined by Pauling and Hendricks in 1925. It is isostructural with corundum (α-Al_2O_3) having a rhombohedrally centered hexagonal unit cell based on a close-packed oxygen lattice in which two-thirds of the octahedral sites are occupied by Fe^{3+} ions

(Schwertmann & Cornell, 2003; Mitra, 1992; Catlow *et al*., 1988; Bowen *et al*., 1993).The space group is $R\bar{3}c$, with lattice parameters $a = 5.0356$ Å, $c = 13.7489$ Å, and six formula units per unit cell (Syvinski & McCarthy, 1990) (**Figure 1.1**). Because of its ubiquity in the natural soil and clay environments, the adsorptive properties of hematite are of interest in the study of transport of contaminants in water and the remediation of waste (Eggleston *et al*., 1998; Hug, 1997; Lefevre, 2004; Lefevre & Fedoroff, 2006; Arai *et al*., 2004; Fukushi & Sverjensky, 2007). Also, hematite shows very interesting magnetic properties (Schwertmann and Cornell, 2003; Mitra, 1992; Catlow, 1988; Bowen *et al*., 1993; Vandenberghe *et al*., 1990; Murad & Schwertmann, 1986), it exhibits ferromagnetism in addition to antiferromagnetism below the Néel temperature of 950 K (Shirane *et al*., 1959). At temperatures known as the Morin temperature (T_M) around 260 K (Fysh and Clark, 1982), hematite is weakly ferrimagnetic.

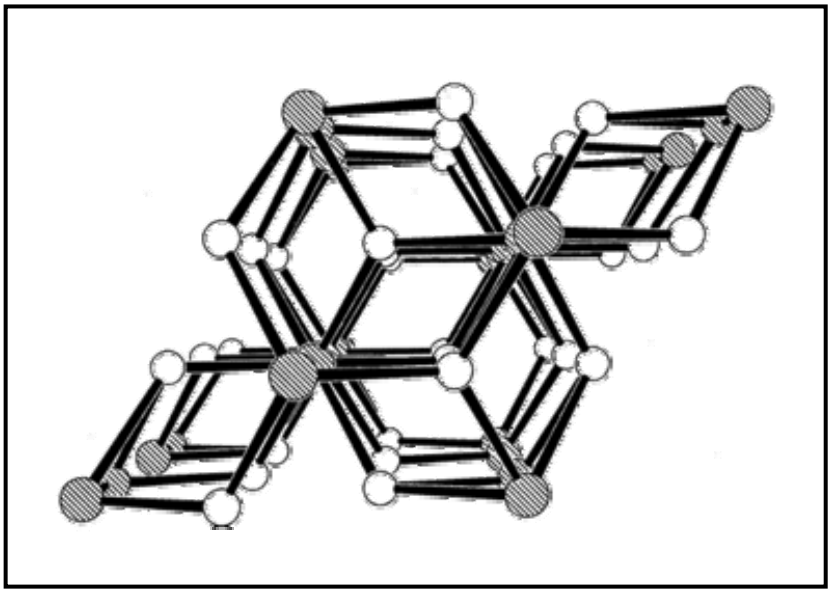

Figure 1.1: Crystal structure of α-Fe_2O_3, viewed onto the (0001) plane. Key: (Fe = shaded circles and Oxygen = white circles).

β-Fe_2O_3

β-Fe_2O_3 is the second polymorph of iron oxides, which was discovered by Bonnevie-Svendsen in 1956. It has only been prepared synthetically from the hydrolysis of $FeCl_3.6H_2O$ without any mention of a natural occurrence. β-Fe_2O_3 was also identified during thermal processing of Mn steel (Nakamori & Shibuya, 1990) as an intermediate product in the reduction of hematite by carbon(van Hien *et al*.,1971) among the products in a spray pyrolysis of an $FeCl_3$ solution (González-Carreño *et al*.,1994), and during the thermal decomposition of $Fe_2(SO_4)_3$ (Zboril *et al*., 1999). Another synthesis method for pure β-Fe_2O_3 is based on its isolation from a reaction mixture during a thermally induced solid-state reaction between NaCl and $Fe_2(SO_4)_3$ in air (Ikeda *et al*., 1986; Zboril *et al*., 1999,).

β-Fe_2O_3 has a body-centered cubic "bixbyite" structure, space group $Ia\bar{3}$, with two nonequivalent octahedral sites for Fe^{3+} in the crystal lattice , as displayed in **Figure 1.2** and **Figure 1.3** respectively. The cubic unit cell with a = 9.404 Å contains 32 Fe(III) ions, 24 of which have C_2 symmetry (d position) and eight C_{3i} symmetry (b position)(Ikeda *et al*., 1986 ; Ben-Dor *et al*.,1977; Maruyama & Kanagawa, 1996;González *et al*., 1994;Bauminger *et al*., 1977; Ben-Dor, 1976; Wiarda *et al*., 1992; Wiarda & Weyer, 1993). There are sixteen formula units per unit cell.

β-Fe_2O_3 is different from other iron oxides, and in particular, hematite, maghemite and ε-Fe_2O_3 because of it is magnetically disordered and exhibits paramagnetic

behaviour at room temperature. However, below the Neel temperature in the range of 100-119 K β-Fe_2O_3 is antiferromagnetic (Bauminger *et al*., 1977; Wiarda & Weyer, 1993; Ikeda *et al*., 1986).

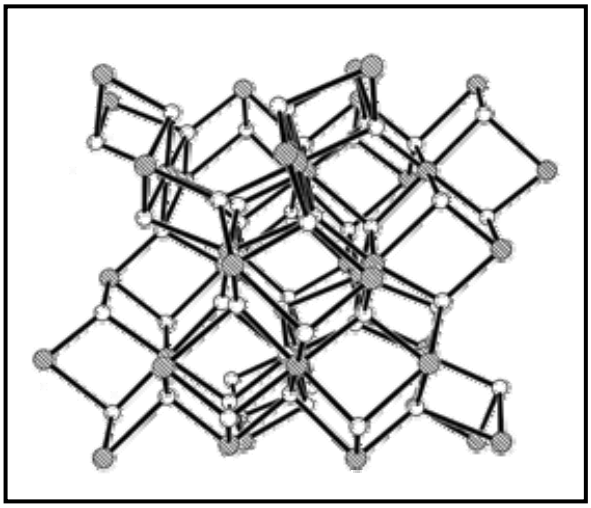

Figure 1.2: Crystal structure of β-Fe_2O_3, viewed onto the (110) plane. Key: (Fe = shaded circles and Oxygen = white circles).

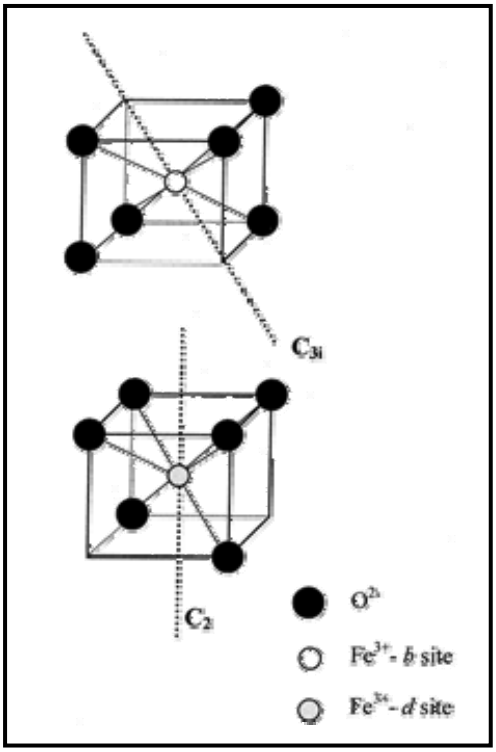

Figure 1.3: Schematic representation of non-equivalent sites of Fe in the structure of β-Fe_2O_3.

Maghemite (γ-Fe_2O_3)

Maghemite, similar to hematite, is a fully oxidized iron oxide polymorph where all iron is in the Fe^{3+} state (Schwertmann & Cornell, 2003). The maghemite crystal structure possesses 2 and 1/3 vacant iron sites within its unit cell (Schwertmann & Cornell, 2003). If these vacant sites are randomly distributed within the crystal structure, then maghemite possesses an inverse spinel structure, similar to magnetite (Glotch & Rossman, 2009; Pecharroman *et al*., 1995; Chamritski and Burns, 2005), which is its generally observed structure (Glotch & Rossman, 2009; Pecharroman *et al*., 1995). Maghemite is an important intermediate to hematite formation from the oxidation of magnetite or the dehydroxylation of goethite precursors (Schwertmann & Cornell, 2003). In **Chapter 3** we will present our investigation of the vacancy ordering in the structure of maghemite (γ-Fe_2O_3).

ε-Fe_2O_3

ε- Fe_2O_3 is similar to the β-Fe_2O_3 polymorph, and this polymorph too has only been synthesised in the laboratory but not so far in a pure form; it is always mixed with the alpha phase or gamma phase, and shows properties intermediate between alpha- and gamma-Fe_2O_3. Material with a high proportion of the epsilon phase can be prepared by thermal transformation of the gamma phase.

ε-Fe_2O_3 was first reported in 1934 (Forestier & Guillot-Guillain, 1934), and in 1963 Schrader and Bûttner prepared identical material from atomized iron in an

electric discharge under oxygen flux and named it ε-Fe_2O_3 (Schrader & Bûttner, 1963). However, the structure was first described completely by Tronc *et al*. in 1998.

ε-Fe_2O_3 has an orthorhombic structure, with space group $Pna2_1$, lattice parameters a = 5.095 Å, b = 8.789 Å, c = 9.437 Å, and eight formula units per unit cell. The structure derives from a close packing of four oxygen layers, and it is isomorphous with $AlFeO_3$, $GaFeO_3$, and presumably ε-Ga_2O_3. The ε-Fe_2O_3 structure as displayed in Figure **1.4** shows that the crystal consists of triple chains of octahedra sharing edges and simple chains of tetrahedra sharing corners which run parallel to the a direction (Tronc *et al*.,1998) In the structure there are three nonequivalent anion (A, B, and C) and four cation (Fe1, Fe2, Fe3, and Fe4) positions. Position Fe4 is tetrahedrally coordinated, and the other three positions are octahedrally coordinated (**Figure 1.5**). ε-Fe_2O_3 is a noncollinear ferrimagnet with Curie temperature close to 470 K (Schrader & Büttner, 1963; Tronc *et al*., 1998; Dézsi & Coey, 1973; Trautman & Forestie, 1965).

In the next chapter, we shall describe the calculated Fe-O bond lengths and relative stabilities and some of the physical properties of the above described four iron oxide polymorphs.

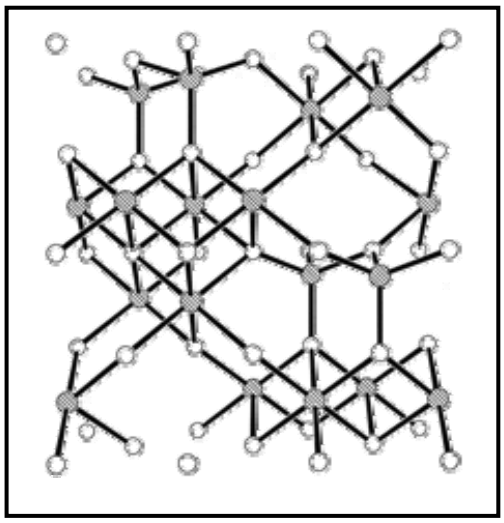

Figure 1.4: Crystal structure of ε-Fe_2O_3, viewed onto the (100) plane Key: (Fe = shaded circles and Oxygen = white circles).

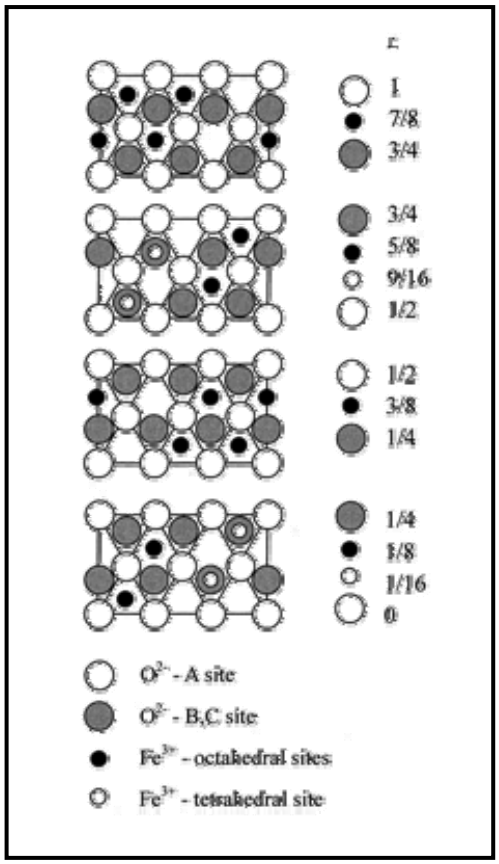

Figure 1.5: Schematic representation of non-equivalent sites of Fe in the structure of ε-Fe_2O_3.

1.1.4 Phase Transitions

The conversion of the different phases of iron oxides arises mainly due to the similarity of the structures of magnetite and maghemite, which further converts into hematite at high temperatures. In the water-gas shift reaction three different iron oxide phases are reported (Kundu *et al*., 1988; Liu *et al*., 2005); the starting material is hematite, which is then reduced to the active phase, magnetite, where some manufacturers have reported the presence of maghemite in this reaction (Kundu *et al*., 1988).

As mentioned, the conversion of magnetite to hematite occurs with the formation of maghemite as an intermediate. Maghemite is the meta-stable phase converted to hematite at about 350°C , as shown in the following reaction:

$$Fe_3O_4 \xrightarrow{200^oC} \gamma\text{-}Fe_2O_3 \xrightarrow{400^oC} \alpha\text{-}Fe_2O_3 \qquad (\mathbf{1.1})$$

In order to convert from maghemite to magnetite, either iron must be added or oxygen must be lost, in addition to the valence change of the iron occupying the tetrahedral sites. The reverse reaction is quite unlikely; the conversion from hematite to magnetite would involve a complete rearrangement of the lattice to create tetrahedral sites because hematite possesses only octahedral iron sites, while both magnetite and maghemite possess tetrahedral and octahedral iron sites. However, once a spinel is formed, conversion between magnetite and maghemite would not involve any lattice rearrangement and should proceed readily.

The epsilon phase is metastable, transforming to the alpha phase at between 500 and 750 °C. ε-Fe_2O_3 appears to be intermediate between γ-Fe_2O_3 and α-Fe_2O_3 and according to (Tronc *et al*., 1998) the structural transformation of γ-Fe_2O_3 to α-Fe_2O_3 occurs either directly or via ε-Fe_2O_3 , depending on the degree of particle agglomeration.

1.2 Surface Science

Research into surface science has made great efforts to further the understanding of, characterization and reactivity of catalysts, because of their importance in industrial processes. Surface science, however, is not only heterogeneous catalysis. The world of microtechnology and nanotechnology has become of particular interest in the last decades, especially for computer science, because experiments that probe the structure and stability at the atomic level are often difficult and hence computer simulation can been used as a complementary tool to gain understanding of the structure and properties of surfaces (Duffy, 1986; Tasker, 1987; Puls *et al*., 1977). Other important areas in the field of surface science are diffusion, creep, crystal growth, corrosion, adhesion, electrochemical reactions, etc (Duffy, 1986; Sakaguchi *et al*., 1992).

1.2.1 Experimental Surface Science Techniques

In this section some common experimental techniques for the analysis of surfaces are reported in the following sections. Experimental techniques can be classified into two categories, either destructive, where the surface structure is destroyed to analyse the components, or non-destructive, where the surface remains intact after the analysis.

Some of these techniques mainly provide information about surface structure and/or adsorbates. Atomic force microscopy (AFM) or scanning tunnelling microscopy (STM) have been developed in recent decades, and are very sophisticated devices. Reflection-adsorption infrared spectroscopy (RAIRS) has been used for more than 50 years and it is one of the most powerful surface techniques. RAIRS is a non-destructive, inexpensive technique, and it is very sensitive to the structure of the adsorbed molecule. Near-edge X-ray adsorption fine structure (NEXAFS) is a powerful, non-destructive technique which is highly sensitive to the adsorption mode of the molecule and its chemical environment. Despite the power of these techniques, their results depend on the capability of experimentalists to assign and resolve their spectra. The theoretical simulation of these spectra can be a great help for the assignation of the bands and the interpretation of the results.

1.2.1.1 Scanning Tunnelling microscope

Since the creation of the scanning tunneling microscope (STM) in 1982 it has proven to be useful tool in the field of surface science. The STM was originally intended as a way to learn about the structure, electronic and growth properties of very thin insulating layers.[26] The aim of this work was to invent a method where by the diversity of the surface could be detected on samples no bigger than a few nanometers in size. Reviews of early work carried out using this method have been written by Rohrer (1994) and Feenstra (1994). This method uses a fine metal tip positioned within 1 nm of the surface to be studied and a voltage is applied between the sample and the tip. Under these conditions a small electronic current will flow from tip to sample or *vice versa* due to electronic tunnelling. Scanning the tip over the surface yields a real space image of the surface, where the outer electron density is probed rather than the geometrical surface. This type of imaging can be thought of as macroscopically drawing a pencil over a rough surface. Electronically processed two-dimensional scanning images or line scans can give a clear impression of the roughness and general morphology of a surface right down to atomic dimensions. Typically, the spatial resolution parallel to the surface is approximately 1Å and < 0.1Å normal to the surface. A schematic diagram of a typical STM is shown below.

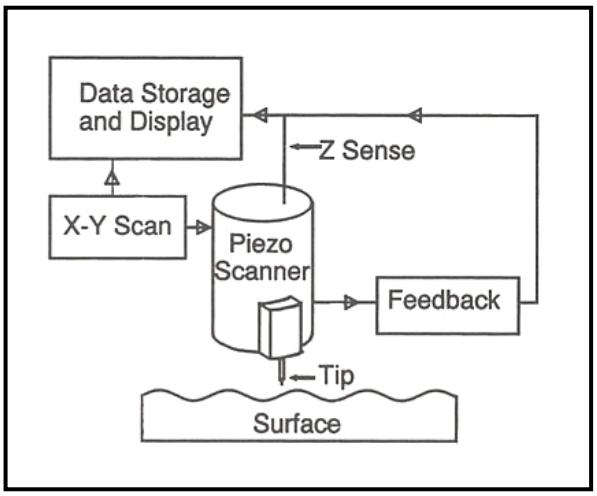

Figure 1.6: A schematic diagram of a Scanning Tunnelling Microscope (STM).

1.2.1.2 Scanning electron microscopy

Scanning electron microscopy (SEM) can provide direct image of film morphology down to dimensions of 10Å in favourable cases. The SEM resolution is determined by the diameter of the electron beam. SEM is usually performed ex situ, *i.e.* films prepared under ultra high vacuum conditions have to be transferred through the atmosphere into the microscope. This may give rise to contamination induced changes to the film structure. Only in special cases is SEM equipment available with ultra high vacuum conditions and transfer units from the preparation chamber. It should also be noted that the SEM picture is produced by secondary electrons, whose emission intensity is affected by a number of factors, such as, geometrical factors *i.e.* type of surface and the inclination of the primary beam, and also by electronic properties of the surface, such as work function and the surface state density. As a result some of the intensity contrast in the image may therefore be related to electronically inhomogeneous areas and not to geometrical inhomogeneities.

1.2.1.3 Temperature programmed Desorption

Thermal desorption spectroscopy (TDS), also known as temperature programmed desorption (TPD) is the method of observing desorbed molecules from a surface when the surface temperature is increased.

When molecules come in contact with a surface, they adsorb onto it, minimizing their energy by forming a chemical bond with the surface. The binding energy varies with the combination of the adsorbate and surface. If the surface is heated, at one point, the energy transferred to the adsorbed species will cause it to desorb. The temperature at which this happens is known as the desorption temperature. Thus TDS shows information on the binding energy (Redhead, 1962).

1.2.1.4 Atomic Force Microscope

The invention of the STM was quickly followed by the development of a whole family of related techniques (Quate, 1994). The most important of which is undoubtedly the atomic force microscope (AFM). AFM operates by measuring attractive or repulsive forces between a tip and the sample (Binning *et al*., 1986). In its repulsive contact mode, the instrument lightly touches a tip at the end of the cantilever to the sample. As a raster-scan drags the tip over the sample, a detection apparatus measures the vertical deflection of the cantilever, which indicates the local sample height. In contact mode the AFM measures hard sphere repulsion forces between the tip and the sample. Because the tip is in hard contact with the surface, the stiffness of the lever needs to be less that the effective spring

constant holding atoms together, which is on the order of 1 - 10 nN/nm. In drawback of the contact mode arises when the scans across a sample with a soft area, i.e. where the stiffness of the lever is greater than the spring constant, in this case the sample is easily deformed by the tip and a cavity or pit will appear in the AFM image. However, configurations AFM in contact mode with a force resolution of 1nN are able to give high quality scans with a depth resolution of 0.02nm.

In non-contact mode, the AFM derives topographic images from measurements of attractive forces, in this case the tip does not touch the sample (Albrecht *et al*., 1991). AFM can achieve a resolution of 0.01nm and unlike electron microscopes it is possible to use this method to image samples in both air and under liquids, the added advantage to the non-contact method compared to the contact method is there is no damage to the surface of the sample.

1.2.1.5 Energy Dispersive X-ray Analysis

An energy-dispersive x-ray analyser (EDX) is a common accessory which gives the SEM a very valuable capability for elemental analysis. The electron beam in an SEM has an energy typically between 5,000eV and 20,000eV. The energy holding electrons in atoms (the binding energy) ranges from a few eV up to many kilovolts. As the electron beam hits the sample many of these atomic electrons are dislodged, thus ionizing atoms of the specimen. Ejection of an atomic electron by an electron in the beam ionizes the atom, which is then quickly neutralised by other electrons. In the neutralisation process an x-ray with an energy

characteristic of the parent atom is emitted, and so by collecting and analysing the energy of these x-rays, the constituent elements of the specimen can be determined.

1.2.2 Computational Surface Science

Theoretical calculations of surface processes are usually carried out by computers, one of the most important inventions of the 20th century which have led to a revolution in science, education and industry. In this thesis, the focus is on atomistic simulations, and the computational techniques that have been used for the work in this thesis will be addressed in the next chapter.

One of the classical applications of surface science using theoretical methods is the surface-water interface, as the growing interest in crystal growth and dissolution processes means that we can no longer meaningfully model surfaces in a vacuum but have to take into account the rôle of water in these processes (e.g. de Leeuw & Parker, 1997, 1998; de Leeuw *et al*., 1999; Mkhonto & de Leeuw, 2002; Cooper & de Leeuw, 2003, 2004). More recently, the interactions of small molecules with mineral surfaces is also being addressed which can provide useful molecular-level insight into complex geochemical phenomena such as surface complexation, mineralization of organic species, mineral dissolution (Filgueiras *et al*., 2006; Cooper & de Leeuw, 2004; de Leeuw & Cooper, 2004; Mkhonto *et al*., 2006) as organic surfactants are well known contaminants in soils, flotation reagents for mineral separation, and crystal growth enhancers/inhibitors. The oxides and oxyhydroxides of iron constitute a broad

class of minerals for which many of theses processes are of direct relevance. For example, organics readily adsorb on ferric-containing minerals such as hematite (α- Fe_2O_3), and certain organic functional groups (e.g., acids) play a significant role in the reductive dissolution of ferric-containing minerals (Hering & Stumm, 1990; Stumm, 1992; 1997). Studies at the molecular level of how organics adsorb and react with minerals such as hematite provide much needed fundamental understanding into surface complexation. Other examples in this field are the adsorption of CO and water on TiO_2 (Pacchioni *et al*., 1996; Goniakowski & Gillan, 1996), NH_3 on MgO (Pugh & Gillan, 1994) and O_2 on $FeSbO_4$ (Grau-Crespo *et al*., 2007).

The increase of computer power and memory over the last few years has made it possible to model surfaces using electronic structure calculations, primarily employing methods based on the Density Functional Theory (DFT). For example, Manassidis & Gillan (1994) investigated surfaces of α-alumina while the work of Schroer *et al*. (1994) concentrated on ZnO and CdS surfaces.

1.3 Experimental and Theoretical Studies on Iron Oxides

Attempts to investigate the effect of water on the stability of iron oxide surfaces have been made by a number of experimental and theoretical studies. For example, Leist *et al.* (2003) have investigated the formation of ice layers on FeO, Fe_2O_3 and Fe_3O_4 films, while Jolivet *et al*. (2004) have focused on the condensation of aqueous clusters onto iron (hydr) oxides. Most theoretical studies

have focused on understanding the surface of the most stable iron oxide polymorph hematite (e.g. Wasserman *et al*., 1997, 1999; Parker *et al*., 1999; Rustad *et al*., 1999; Jones *et al*., 2000; Lado-Tourinˇo & Tsobnang, 2000), whereas some other studies have concentrated on the study of the bulk hematite structure and the water-hematite interface (de Leeuw & Cooper, 2007). Finally, some studies have investigated the effect of water on other reactions; Baltrusaitis & Grassian (2005) have studied the reaction of CO_2 at the water/oxide interface, whereas Archuleta *et al*. (2005) have studied the nucleation of ice at acid-coated iron oxide powders.

Speculation remains about the effect of water on the stability of different iron oxides phases. It is therefore one of the aims of this thesis, which will be treated in **Chapter 4**, to study the adsorption of water at maghemite and hematite surfaces, creating different low index surface structures of maghemite (γ-Fe_2O_3) and hematite (α-Fe_2O_3), followed by an examination of the hydroxylation of theses surfaces to understand the behaviour and the influence of water dissociation on the surface stability and reactivity of these two iron oxide minerals. We have chosen these minerals, firstly because hematite is the most thermodynamically stable iron oxide under aerobic conditions and has already been studied by several theoretical and experimental studies, while the bulk and surfaces of maghemite have not yet been studied.

Another interesting field is the adsorption of pollutants onto iron oxide surfaces, for example, the investigation of the mechanism for adsorption of arsenate onto different mineral surfaces, such as aluminum, iron, manganese, and titanium

(oxyhydr) oxides, which have been studied by several researchers using either experimental methods or theoretical calculations (Waychunas *et al*.,1993,1995,1996,2005;Manceau,1995; Sun & Doner,1996; Fendorf *et al*., 1997;Arai *et al*.,2001,2004; Ariai & Sparks,2002 ;Goldberg & Johnston,2001;O'Reilly *et al*., 2001;Randall *et al*., 2001; Farquhar *et al*., 2002; Manning *et al*., 2002; Foster *et al*., 2003; Sherman & Randall,2003; Pena *et al*.,2006).

Recently the adsorption of arsenate has been studied on the two most important hematite surfaces, the {0001} and $\{01\bar{1}2\}$ planes, using X-ray crystal truncation rod (CTR) scattering measurements showing the changes in the CTR data between the clean and As-sorbed surfaces. (Waychunas *et al*., 2005) which confirmed that the arsenate adsorbs on ordered surface sites.

1.4 Objectives of the Thesis

Work presented in this thesis uses atomistic simulation techniques to advance our understanding of the surface chemistry of two important iron oxide minerals, hematite (α-Fe_2O_3) and maghemite (γ-Fe_2O_3), which have important applications in many fields, including as remedial agents in the soil. We have employed computational techniques using interatomic potentials methods to perform a quantitative study of the adsorption of different pollutants at both hematite and maghemite surfaces.

The main objectives of this thesis are:

- To compare several interatomic potential models to describe the structures and properties of four iron oxide polymorphs, namely α-Fe_2O_3(hematite), β-Fe_2O_3, γ-Fe_2O_3 (maghemite) and ε-Fe_2O_3 to choose a suitable potential for these systems .
- To investigate the energetics of vacancy ordering in γ-Fe_2O_3 (maghemite), using a statistical approach to evaluate ordering as a function of temperature.
- To model the surface structures and stabilities of hematite and maghemite.
- To evaluate the effect of dissociatively adsorbed water on the surface structure and stabilities.
- To provide energetic and structural details of the adsorption of different pollutant molecules at the dominant mineral surfaces.

1.5 Thesis Outline

The thesis is divided into seven main chapters. The first two chapters serve as introduction to the materials and methods; chapter 1 provides background information on iron oxides, especially the main four polymorphs of Fe_2O_3: α-Fe_2O_3 (hematite), β-Fe_2O_3, γ-Fe_2O_3 (maghemite) and ε-Fe_2O_3; the importance of surface science and a brief review of the available experimental and computational studies on these materials.

Chapter 2 presents the theoretical techniques used in this work, focusing on interatomic potential (IP) methods which have been used to describe the structural details and physical properties of four iron oxide polymorphs in a comparison of three sets of interatomic potentials. This is followed by describing the methodology used in the latter parts of the thesis, for the generation of the surface and the adsorption of molecules at the mineral surfaces.

Chapter 3 presents our investigation of vacancy ordering in γ-Fe_2O_3 (maghemite) from an energetic point of view, whereas chapter 4, reports our results of the surface energies and the hydration energies of the surfaces of hematite and maghemite, were we use the ordered maghemite structure from Chapter 3.

Chapter 5 and 6, present results for the adsorption at the major surfaces of methanoic acid and hydroxyethanal, as examples of organic pollutants in the soil, and arsenic which is a toxic pollutant in groundwater. The final chapter provides a brief summary and the conclusions with future work.

Chapter 2

Methodology

2.1 Computational Techniques

Computational chemistry is the subfield of chemistry where mathematical methods are combined, ranging from the postulates and theorems of quantum mechanics to many theories of classical mechanics, to model the material. Materials modelling methods can be divided into two categories, electronic structure calculations and classical interatomic potential (IP) methodology, where the accuracy of the potential model defines the quality of the simulation results.

2.1.1 Density Functional Theory (ab initio)

The increase in computer power and memory over the last few years has made it possible to model surfaces using electronic structure calculations, usually employing methods based on the Density Functional Theory (DFT). The goal of *ab initio* methods is to solve the Schrödinger equation to some level of approximation to calculate the energy of an atom, molecules or a periodic system.

The Density Functional Theory (DFT) is based on the electronic density of the system, where the electron density itself is intimately related to the ground state energy of the entire system of electrons and nuclei. Once this energy is known, any physical property that can be related to a total energy, or to a difference between total energies, can be calculated (Parr &Yang, 1989, Koch & Holthausen, 2000). Such total-energy techniques have been used to predict properties such as equilibrium lattice constants, bulk moduli, phonon modes, piezoelectric constants, and phase-transition pressures and temperatures (see Payne *et al.,* 1992) for a discussion).

The Density Functional Theory is based on two theorems, published by Hohenberg and Kohn in 1964 (Hohenberg & Kohn, 1964), and further advanced by Kohn and Sham in the following year (Kohn & Sham, 1965), who introduced orbitals, thereby being able to develop a scheme which split the kinetic energy functional into two parts: the kinetic correlation energy which can be calculated exactly and the exchange correlation energy which is a small correction term which can be solved separately. This indirect approach to calculating the kinetic energy into two parts allowed DFT to be used as a practical tool for rigorous calculations.

The first Hohenberg-Kohn theorem proves that the two variables N (number of electrons) and external potential $v(r)$ can be replaced by the electron density, ρ, where the electron density is defined as the number of electrons per unit volume. As a result, $v(r)$ and N can be determined by the electron density. They also proved that v(r) and N uniquely determine (r), as well as the Hamiltonian.

Therefore, all properties of a physical system can be calculated if (r) is known and we can write the energy of the Schrödinger equation as a functional of the electron density:

$$E[\rho(r)\} = T[\rho(r)] + V_{ee}[\rho(r)] + V_{ext}[\rho(r)] \qquad \textbf{(2.1)}$$

$$F_{HK}[\rho(r)] + Vee[\rho(r)] \qquad \textbf{(2.2)}$$

where T is the total kinetic energy and V_{ee} is the functional describing the electron-electron interaction, together called the Hohenberg-Kohn fuctional (F_{HK}), which is not dependent on the external potential, and V_{ext} is the Coulombic attraction between electrons and nuclei.

Theorem 2 (the variational principle) states that in order to find the ground state energy for a given potential, it is necessary to vary the electron density with respect to the energy of the system. The minimum in this energy corresponds to the ground state electron density, $Eg[n(r)]$. Thus by minimising $Eg[n(r)]$ with respect to n(r) for a fixed v(r), the $n(r)$ which yields the minimum energy must be the electron density in the ground state. Taken together, these two theorems provide the means to find the ground state energy for any given external potential.

In principle, DFT is an exact theory, but in practice various approximations must be made in order to obtain a tractable form for the mathematics for real systems. These approximations all relate to the many-body interacting electron system, which by its nature is immensely complicated. This problem is approached by treating the many-body interactions as a simpler, one-body interaction, which

describes an "imaginary" non-interacting electron system which possesses the same density as the real, interacting one. In turn, the many-body interactions are modelled using further approximations. The choices that must be made in DFT calculations include the form of the exchange-correlation functional, the selection of a basis-set for the expansion of the Kohn-Sham orbitals and the algorithms adopted for solving the Kohn-Sham equations and for calculating energies, forces and stresses. These, as well as the degree to which the chosen functional accounts for many-electron correlations, and the completeness of the basis-set, determine the accuracy of the calculation whilst the numerical algorithms are decisive in regards to its efficiency (Hafner, 2007).

2.1.2 Interatomic Potential Methods (Force Fields)

The aim of this chapter is to introduce the basic concepts underlying the computational methods that have been applied during this thesis work.

In this study, we have employed atomistic simulation techniques based on the Born model of solids (Born & Huang, 1954) to investigate the bulk and surfaces of iron oxides and the interactions between the mineral surfaces and different types of pollutants. Throughout this thesis we have used both GULP (the General Utility Lattice Program) (Gale, 1997; 2005; Gale & Rohl, 2003) and METADISE (Minimum Energy Techniques Applied to Dislocations, Interface and Surface Energies) (Watson *et al*., 1996) to carry out the simulations. Atomistic simulations are widely used in the prediction of equilibrium structures, physical properties, defects, and surface stability.

Interatomic potential techniques are based on a number of assumptions, which together form what is usually called the Born model of solids (Born & Huang, 1954), which assumes that the ions in the crystal interact via long-range electrostatic forces and short-range forces, which include Pauli repulsions and van der Waals attractions between electron charge clouds, which can be described by the equation:

$$E(r_{ij}) = \sum_{ij} \frac{qiqj}{4\pi\varepsilon_0 \left(r_{ij} + 1\right)} + \sum_{ij} \Phi_{ij}(r_{ij}) \qquad \textbf{(2.3)}$$

The first term in equation (2.3) represents the long-range electrostatic interaction (Columbic interaction) between the charges of all the ions, where q_i and q_j are the charges on atoms i and j respectively, r_{ij} is the distance between atoms i and j, and ε_0 is the permittivity of free space. The second term is the short-range interactions between neighbouring electron clouds, which are described by a number of potential (below). Unfortunately, the long-range electrostatic part of the potential (the first term of equation 2.3) does not converge quickly in real space. The method of Ewald (Ewald, 1921), provides a solution to this problem, which divides the electrostatic sum into two parts: the first (at short distance) is summed in real space, while the second (at longer distance) is computed in reciprocal space.

2.1.2.1 Ewald Summation

The electrostatic energy is an important term in many inorganic materials, particularly in oxides and the accuracy of the calculation of this energy is

achieved through introduction of the Ewald summation (Ewald, 1921). This method recast the potential energy into the sum of two rapidly converging series plus a constant term, one in the real space and one in the reciprocal space. Therefore, the Ewald summation is written as the sum of three parts as below:

$$U_{Ewald} = U^r + U^m + U^o \qquad \textbf{(2.4)}$$

where U^r is the real (direct) space sum, U^m the reciprocal (imaginary, or Fourier) sum, and U^o is the constant term, which is known as the self-term.

$$U^r = \frac{1}{2}\sum_{i,j}^{N}\sum_{n} q_i q_j \frac{erfc(\alpha r_{ij,n})}{r_{ij,n}} \qquad \textbf{(2.5)}$$

$$U^m = \frac{1}{2\pi V}\sum_{i,j}^{N} q_i q_j \sum_{m\neq 0} \frac{\exp(-\pi m/\alpha)^2 + 2\pi i m(r_i - r_j))}{m^2} \qquad \textbf{(2.6)}$$

$$U^o = \frac{-\alpha}{\sqrt{\pi}}\sum_{i=1}^{N} {q_i}^2 \qquad \textbf{(2.7)}$$

where V is the volume, m is the reciprocal space vector, and N the number of particles. The self-term is a correction term, which cancels out the interaction of each of the introduced counter charges. *erfc(x)*, is the complimentary error function (Catlow & Norgett ,1976; Karasawa & Goddard, 1992) which can be evaluated and truncated in real space.

$$exfc(x) = 1 - erf(x) = 1 - \frac{2}{\sqrt{\pi}}\int_0^x \exp(-u^2)du \qquad \textbf{(2.8)}$$

2.1.2.2 Parry Method

The Parry method (Parry 1975; 1976) is a special application of the Ewald method, which is used for two-dimensional system, for example, surfaces. With the Parry method the vectors are divided into in-plane vectors (p_{ij}), and vectors perpendicular to the plane, (u_{ij}), with the summation of the columbic energy given by:

$$U_p = \frac{\pi}{A}\left[\begin{array}{l} -2u_{ij}erf(\eta u_{ij}) - \dfrac{2\exp(-\eta^2 u^2{}_{ij})}{\eta\sqrt{\pi}} + \\ \displaystyle\sum_{k\neq 0}\frac{\exp(ik\rho_{ij})}{k}\left[\exp(ku_{ij})erfc(\frac{k}{2\eta}-\eta u_{ij}) + \exp(-ku_{ij})erfc(\frac{k}{2\eta}-\eta u_{ij})\right] \end{array}\right] \quad \textbf{(2.9)}$$

where A is the area of the unit cell, and η a parameter chosen to obtain rapid convergence.

2.2 Interatomic Potential Functions

Interatomic potential describe in both analytical and numerical form, the forces between atoms, and by evaluating theses forces, it will be possible to calculate the total energy with respect to the nuclear coordinates. The potential energy function is made up of two-body potential functions, which depend only on the relative position of pairs of atoms, three-body and four-body potential functions, with the total short-range energy expressed as:

$$U^{short-range}(r_1,...,r_N) = \sum_{A,B} U_{AB}(r_A, r_B) + \sum_{A,B,C} U_{ABC}(r_A, r_B, r_C) + ... \qquad \textbf{(2.10)}$$

where U_{AB} refers to the two-body interactions, U_{ABC} to three-body interactions, and so on. The most important contribution to the above expression is the two-body interaction, which include non-bonded interactions (repulsion and van der Waals attraction) between neighbouring electron charge clouds.

Harmonic Potential

The simplest potential of the two-body potential functions is the harmonic potential, which is proportional to the square of the difference of the separation of the two atoms from the equilibrium value in the form:

$$U(r_{ij}) = \frac{k_{ij}}{2}(r_{ij} - r_0)^2 \qquad \textbf{(2.11)}$$

where k_{ij} is the bond force constant between atoms i and j, with r_{ij} the distance between atoms i and j, and r_0 the equilibrium separation of the atoms.

Morse Potential

To describe the interaction between ions bonded by a (partially) covalent bond, a Morse potential is sometimes preferable. It is a two-body potential function, where the energy is exponentially related to the interatomic spacing (r_{ij}) and the equilibrium distance (r_0), which is given by expression:

$$U(r_{ij}) = D\left(1-\exp\left[-\alpha_{ij}\left(r_{ij}-r_0\right)\right]\right)^2 - D \qquad \textbf{(2.12)}$$

where D is the dissociation energy between atoms i and j , and α_{ij} is a constant term which controls the width of the potential well and which can be obtained from spectroscopic data (Morse ,1929).

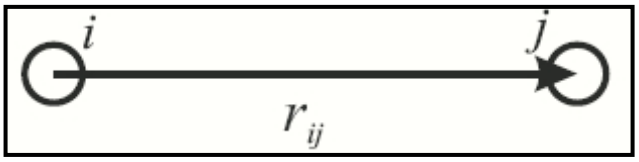

Figure2.1: Interatomic bond vectors.

Lennard-Jones Potential

This widely used potential function for non-bonded interactions, especially for large systems such as molecular crystals, has the following expression:

$$U(r_{ij}) = \frac{A}{r_{ij}^{12}} - \frac{B}{r_{ij}^{6}} \qquad \textbf{(2.13)}$$

where A and B are variable parameters, which are usually derived empirically.

Buckingham Potential

For ionic or semi-ionic solids (Buckingham, 1936), the most frequently used functional form for the short-range two-body potential is the so-called

Buckingham potential, where the r^{-12} repulsive term of the Lennard-Jones potential is replaced by an exponential term:

$$U(r_{ij}) = A_{ij} \exp\left(\frac{-r_{ij}}{\rho_{ij}}\right) - \frac{C_{ij}}{r_{ij}^6} \qquad \textbf{(2.14)}$$

in which the exponential expression represents the size and hardness of the ion, while the r^{-6} term represent the longer range van der Waals interactions. When the $\frac{C_{ij}}{r_{ij}^6}$ term is omitted, the potential function is known as a Born-Mayer potential.

In both Buckingham potential and Lennard-Jones potentials, the first term models the repulsive interactions due to the Pauli forces, and the second one represents the attractive interactions due to the van der Waals dispersion forces. At short distances the repulsive forces become much higher than the attractive ones.

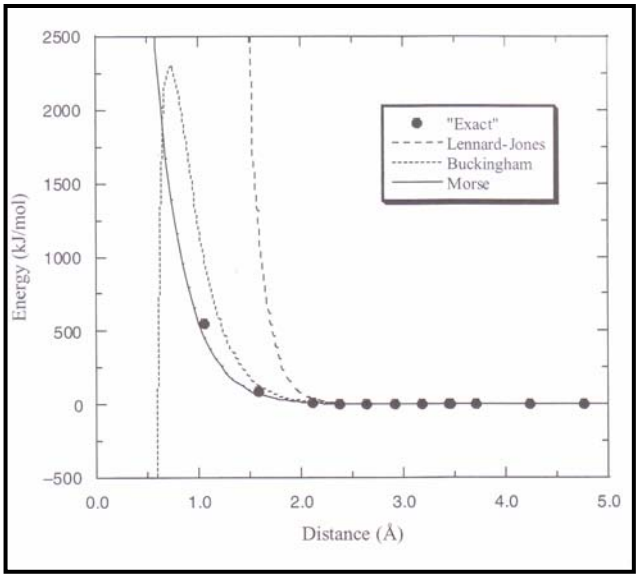

Figure 2.2: Show sketch of the three different interatomic potentials.

Three-Body Interaction

The second main contribution to the short-range energy is the three-body potential, which is used to describe the bond bending within a system of three atoms. The simplest form of this potential is:

$$U(\theta_{ijk}) = \frac{k_{ijk}}{2}\left(\theta_{ijk} - \theta_0\right)^2 \qquad \textbf{(2.15)}$$

where θ_{ijk} is the angle between the two bonds i-j and i-k (**Figure 2.3**) , and both atoms j and k are joined in the middle by a third atom i .Then the bond-bending force (k_{ijk}) is proportional to the deviation of the bond from equilibrium , and θ_0 is the equilibrium angle between the three atoms, as shown in **Figure 2.3**.

.

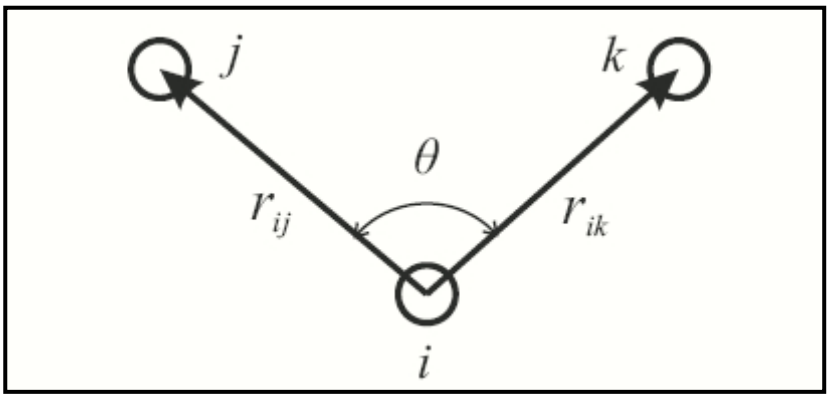

Figure 2.3: The valence angle and associated vectors.

Four-Body Interaction

For molecules and molecular solid systems, the expansion of the potential energy could be extended to include four-body terms, which are used to describe the dihedral angle between four atoms as displayed in **Figure 2.4**. This four-body potential has the following form:

$$U(\phi_{ijkn}) = k_{ijkn}\left(1 - s\cos\left(n\phi_{ijkn}\right)\right) \qquad \textbf{(2.15)}$$

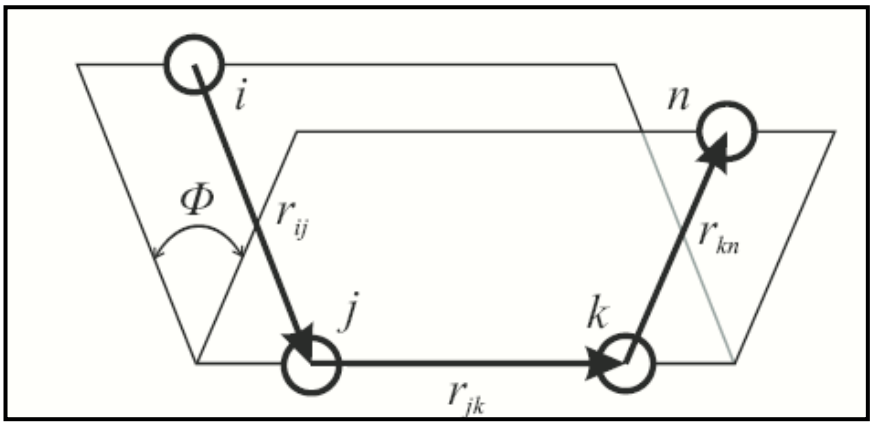

Figure 2.4: Showing the dihedral angle between the plane containing atoms, i, j and k, and plane containing the j, k and n.

2.3 The Electronic Polarisability

In many situations the electronic polarisability of the atoms has an important effect on the accurate calculations on a system which contains polarisable ions, for example, when simulating defect or surface properties. The electronic polarisability of the oxygen atoms in the iron oxide polymorphs, water and arsenate molecules, in this work is included via the shell model of Dick and

Overhauser (Dick & Overhauser, 1958), where each polarisable ion, is represented by a massive core charged q_{core} which bears the mass of the ion, and a massless shell charged q_{shell}, connected by a spring. This simple mechanical treatment of the atomic polarisability by the shell model is illustrated in **Figure 2.5**. The free atom polarisability α, is given by following expression:

$$\alpha = \frac{q^2}{k} \qquad \textbf{(2.16)}$$

where k is the force constant for the spring connecting the core and the shell, and q is the total charge on the shell.

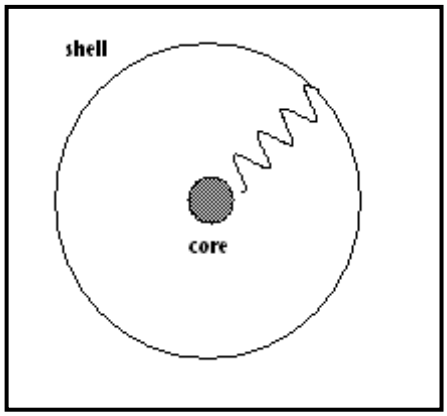

Figure 2.5: Illustration of the shell modal of ionic polarisability.

2.4 Modelling Methods

2.4.1 Energy Minimization Techniques

If potentials precisely reproduce the ionic structure, then the lattice energy of the simulated crystal will be at a minimum point when ionic distances exactly match the observed crystal structure and any movement away from this minimum point

would give a configuration with a higher energy. However, this is seldom the case and the calculated lattice energy at minimum point can be achieved in two ways:

Constant Pressure Minimization:

In this approach, the pressure is kept constant. The unit cell is repeated throughout space using periodic boundary conditions and the total energy is minimized by removing all strain through allowing relaxation of both the ions in the unit cell and the lattice vectors.

Constant Volume Minimisation:

When this approach is followed, no variation in the cell dimension is allowed as the volume is kept constant.

The system is always relaxed until it reaches the minimum energy configuration. However, the potential energy surface is very complex as it is a multi-dimensional function of the coordinates of the system, which can contain several maximum and minimum points; the latter can be either local or global, as displayed in **Figure 2.6**.

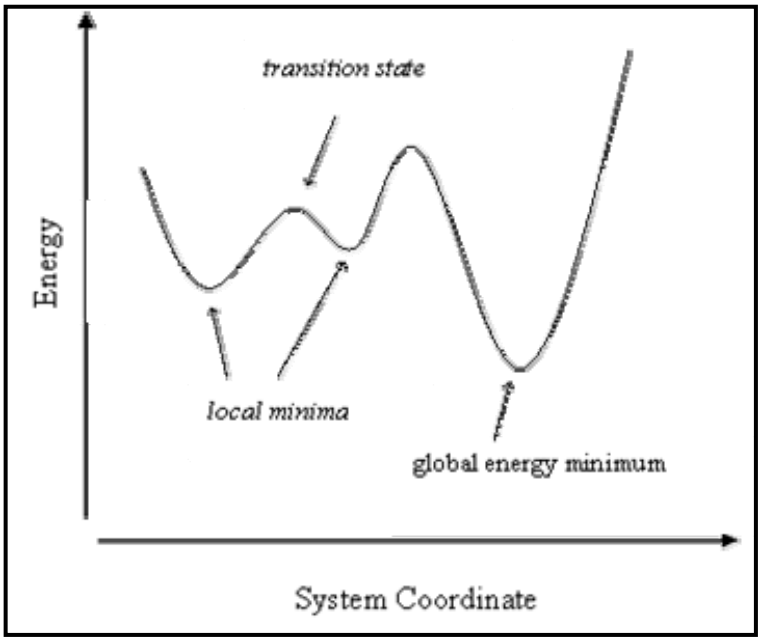

Figure 2.6: A simplified (ID) representation of the potential energy surface with local minima and transition state.

At a minimum point on the potential energy surface the first derivative of the energy function with respect to all nuclear coordinates is zero and the second derivates are all positive:

$$\frac{\partial U}{\partial r_i} = 0; \frac{\partial^2 U}{\partial^2 r_i} > 0 \qquad \textbf{(2.17)}$$

where U is the lattice energy and r is the coordinate system. However, the term zero force is used since the derivative of lattice energy with respect to distance is force, and this point is useful when we want to calculate some physical properties such as the elastic constants.

There are many different algorithms that can be used to find a minimum energy structure from an initial configuration. The most common alghorithms used for

energy minimisation are the Conjugated Gradients, or Newton Raphson Methods (Hayward, 2002; Leach, 1996; Jensen 1999).

The Newton-Raphson method is widely used in both perfect and defect lattice energy minimization, as it is rapidly convergent. This method requires a gradient (first derivative) and a Hessian (second derivative) of the energy in the minimisation procedure. Sometimes the Hessian is large, and then we can use the alternative method, the Conjugate Gradients method (Fletcher & Powell 1963) which requires only the first derivative, not the Hessian and is hence less compute-intensive, although less accurate. In our METADISE calculations to obtain the surface energies and adsorption energies, we have used both Conjugated Gradients, and Newton Raphson methods as discussed in section 2.6.2.

Within this thesis, the structures of the iron oxide polymorphs were simulated by energy minimisation, using an interatomic potential model. As stated above classical models make use of pair potentials, as opposed to electronic structure (*ab initio*) methods where the probability of finding electrons are described by wavefunctions, or in terms of electron densities. The main advantage of interatomic potential methods over *ab initio* methods is that the calculations are computationally inexpensive, allowing more and larger systems to be considered, and if the potential models are parameterised correctly, they are very reliable and give accurate results.

2.4.2 Monte Carlo

Monte-Carlo simulation is a useful technique for financial modelling that uses random inputs to model uncertainty. The use of MC methods to model physical problems allows us to examine more complex systems than we could otherwise. Solving equations which describe the interactions between two atoms is fairly simple; solving the same equations for hundreds or thousands of atoms is impossible. With MC methods, a large system can be sampled in a number of random configurations, and these data can be used to describe the system as a whole. This method has been used successfully in modelling a wide variety of applications (Gillespie, 1977).

The success of the MC procedure hinges upon the ability to generate all possible chemical events or configurations that could occur in the system under study. Assuming that there are N possible chemical events possible, then the MC procedure, based on a probability distribution function for events (Gillespie,1977) expresses the probability of occurrence of each event as follows:

$$P(r_i) = 1 - \exp(-R_i \delta t_i) \qquad \textbf{(2.18)}$$

where Pi represents the probability of occurrence of the ith event, r_i is a random number extracted from a uniform random number generator, R_i is its corresponding rate, and δt_i is the time associated with the ith event. Based on Eq. (**2.18**), δt_i is estimated stochastically as given in equation:

$$\delta t_i = -\frac{1}{R_i}\log(1-r_i) \qquad \textbf{(2.19)}$$

Next only the event with the smallest δt is chosen to occur and the system is propagated for a time equaling the size of the smallest time step. The above steps are repeated and the system is propagated in time until it attains equilibrium as shown in **Figure 2.7**.

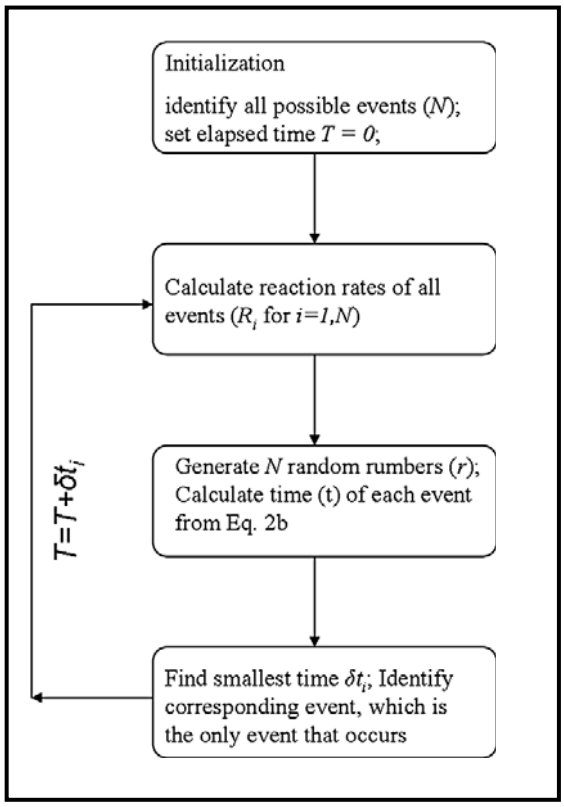

Figure 2.7: Flowchart representing the workings of a MC simulation to determine reaction rates.

2.5 Simulation Codes

In this study we have used two computer simulation codes, GULP (Gale, 1997; 2005; Gale & Rohl, 2003) (the General Utility Lattice Program) and METADISE (Watson *et al*., 1996) (Minimum Energy Techniques Applied to Dislocations, Interface and Surface Energies) and the choice of code is determine by the type of the problem that we wish to solve and to calculate the properties of interest. We therefore, describe the main features of each code has used.

Gulp

GULP is a molecular modelling program which is based on interatomic potentials. We have used GULP to model the bulk structure of iron oxide polymorphs. With this code we have minimised the lattice energy of the crystal in order to obtain the optimum ion coordinates and cell parameters at zero or finite temperature. Later we have used GULP with the S.O.D program (Site Occupancy Disorder) (Grau-Crespo *et al*., 2007) to investigate the vacancy ordering in the structure of maghemite, and the main features of this program will be described in **Chapter 3**.

METADISE

The lattice energies of the pure and hydroxylated surfaces and their interaction with the pollutant molecules were calculated using the energy minimisation code METADISE, where periodic boundary conditions and sufficiently large supercells

are employed to avoid surface and finite size effects and interactions between the repeating images.

2.6 Simulating Surfaces and Interfaces

To model the surfaces with interatomic potential (IP) models, we have used the METADISE program (Watson *et al.*, 1996), which is designed to model dislocations, interfaces and surfaces. This code determines unrelaxed and relaxed surface energies and surface structures. We have followed the approach of Tasker (Tasker, 1979) where the simulation model consists of a series of charged planes parallel to the surface and periodic in two dimensions. Tasker classified surfaces as three different types:

1. ***Type I surfaces***, where the repeat unit is a charge neutral stoichiometric layer (**Figure 2.8**(**a**)).
2. ***Type II surfaces***, which comprise charged layers but in such a way that there is no dipole moment perpendicular to the surface (**Figure 2.8**(**b**)).
3. ***Type III surfaces***, where there is a dipole moment perpendicular to the surface (**Figure 2.8**(**c**)).

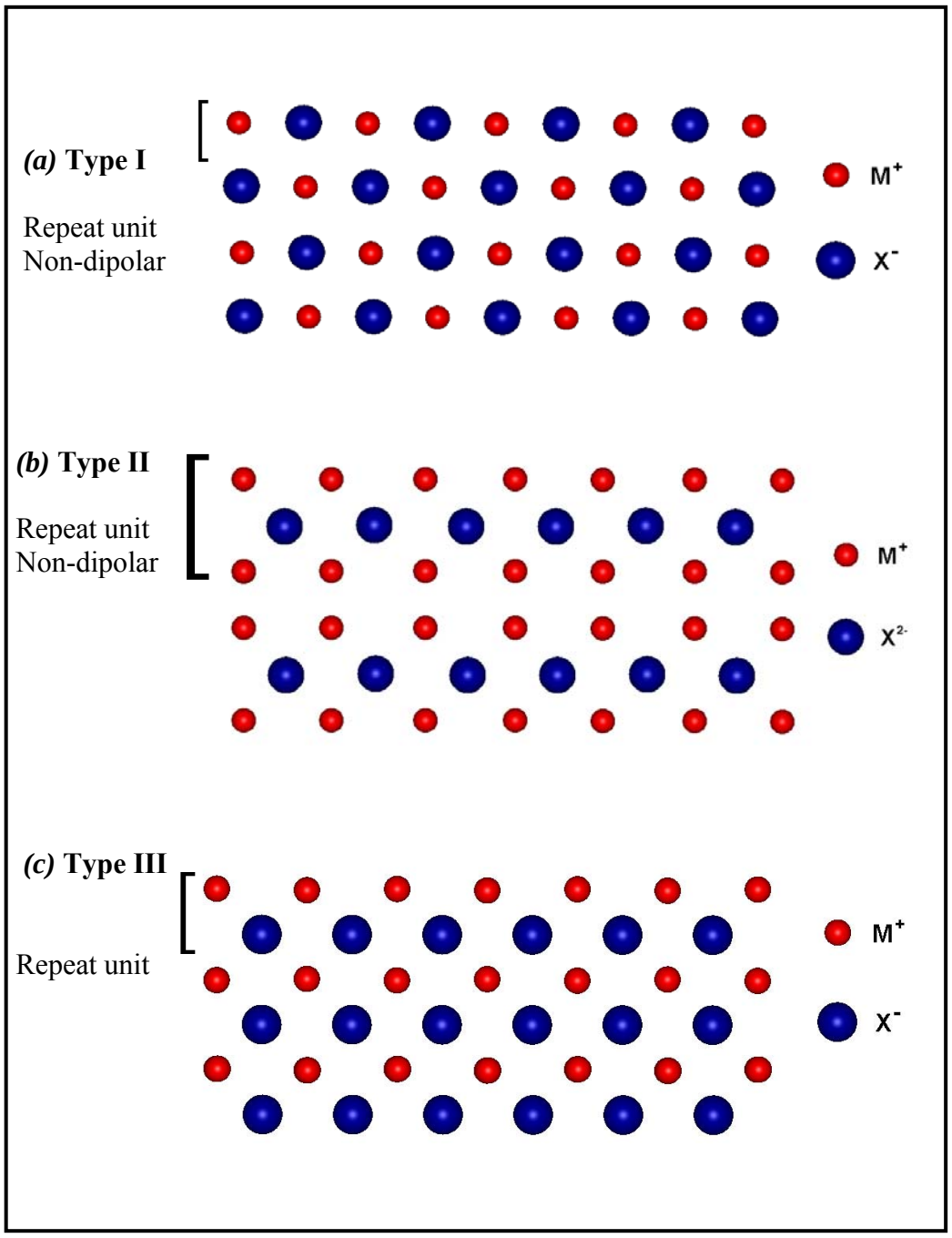

Figure 2.8: The three different types of surfaces as classified by Tasker.

In type III surfaces (**Figure 2.8(c)**), the stack of charged planes produces a net dipole moment perpendicular to the surface. When a dipole moment is perpendicular to the surface of a unit cell, its surface energy diverges and is

infinite (Bertaut, 1958). So Type III surfaces must be modified to remove the dipole moment before any energy can be calculated. In order to remove the surface dipole, half of the ions from the surface layer at the top of the repeat unit are shifted to the bottom layer resulting in the formation of a surface, which is partially vacant in either cations or anions. These partially vacant surfaces are usually very unstable and reactive towards impurities or the addition of water and are often found to reconstruct into different surface geometries (Tasker, 1979).

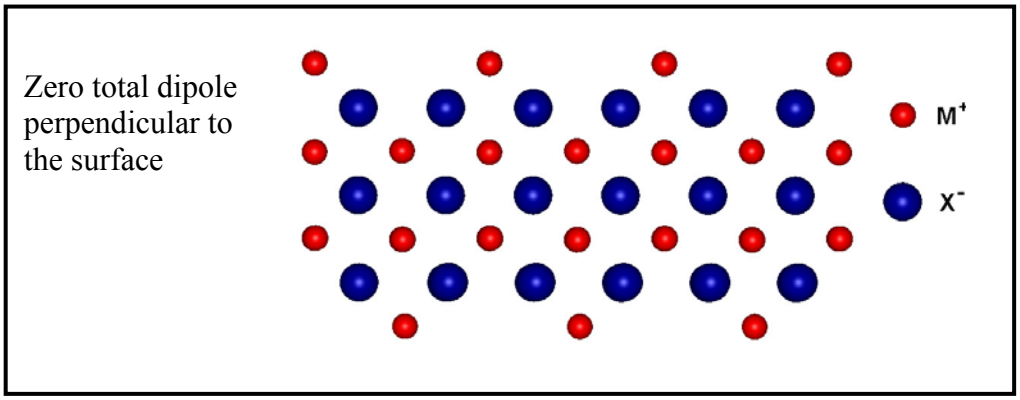

Figure 2.9: Stacking sequences showing a reconstructed Type III surface where half the surface ions have been shifted to the bottom of the unit cell, which has removed the dipole in the reaped unit.

The METADISE code (Watson *et al*., 1996), considers the crystal as a stack of charged planes of atoms, periodic in two dimensions and parallel to the surface being investigated. A block of such stacks is chosen which extends into the crystal and models a specific area of the surface. This block is further separated into two regions, region I and region II, where region I is a the block of atoms near the surface. Region II is a "bulk" region below region I (**Figure 2.10**). In the simulations we need to include the region II to ensure that atoms at the bottom of region I are modelled correctly. The atoms of region 1 are permitted to relax to

their surface equilibrium positions, while those of the bulk are fixed at the bulk equilibrium positions. The sizes of both blocks are increased until the surface energy no longer varies, signifying convergence.

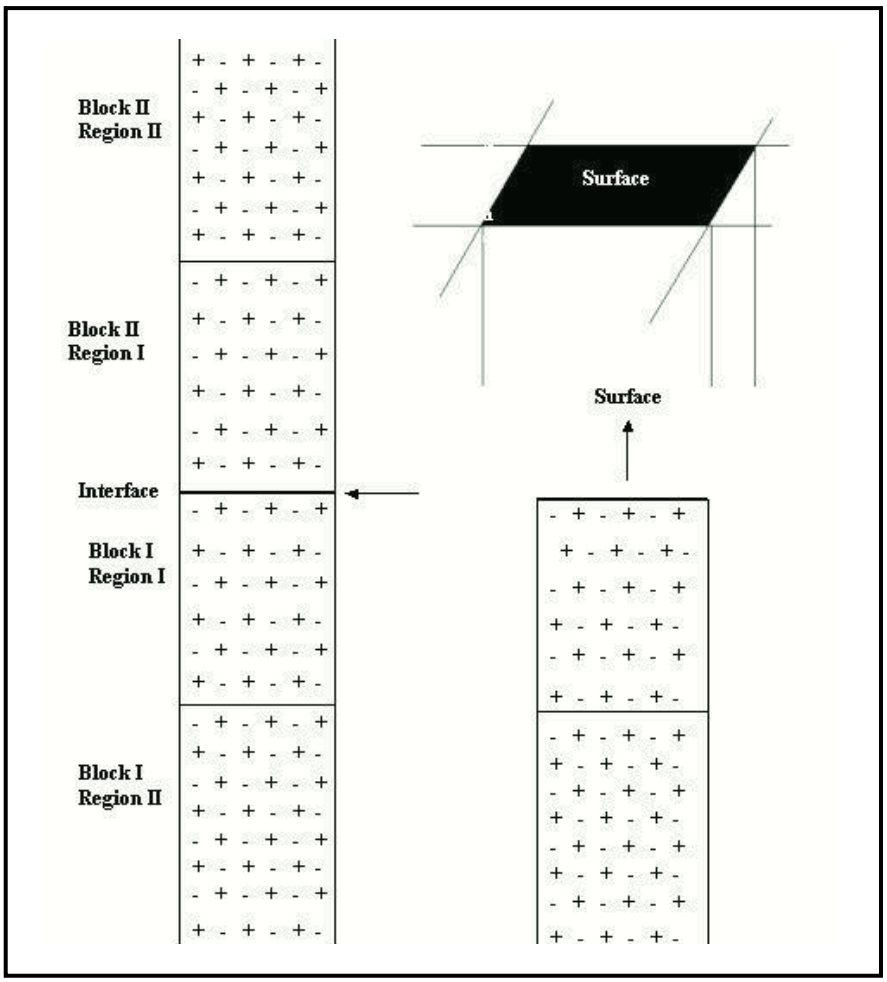

Figure 2.10: The two-region approach, complete crystal (left), half a crystal, exposing the surface (right).

2.6.1 Surface and Adsorption Energies

The stability of the crystal surfaces can be determined by calculating the surface energy, denoted by γ, which experimentally is defined as the energy required to cleave the bulk crystal exposing the surface. This is given by:

$$\gamma = \frac{(U_{surf} - U_{bulk})}{A} \qquad \textbf{(2.20)}$$

where U_{surf} is the energy of the simulation cell containing the surface, U_{bulk} the energy of the bulk crystal containing *an* equivalent number of atoms as the surface block, and A is the surface area. A low positive value for γ indicates a stable surface.

In our study, we have investigated the hydroxylation of both hematite and maghemite surfaces through the adsorption of water molecules, when a water molecule dissociates on the surface of Fe_2O_3, the OH will become bonded to the cation and the proton will bind to a surface oxygen atom. Usually, there is a strong interaction between water and ionic surfaces. As the most stable surface structure has the lowest surface energy, the difference in surface energy between the dry and hydroxylated surface provides information on which surfaces are stabilised by the reaction with water. In this case we need to include extra term to calculate the surface energy (de Leeuw & Cooper, 2007):

$$\gamma_{hydrated} = \frac{(U_{surf+water} - nU_{water} - U_b)}{A} \qquad \textbf{(2.21)}$$

The adsorption energies of different molecules at a surface can be calculated by comparing the energy of the surface with the adsorbed surfactant, and the sum of the energies of the pure surface and that of a free molecule.

$$U_{ads} = U_{surf+molcule} - (U_{surf} + U_{molecule}) \quad \textbf{(2.22)}$$

where $U_{surf+molecule}$ is the energy of the surface with the adsorbed molecule, U_{surf} is the energy of the simulation cell containing the surface only and $U_{molecule}$ is the energy of the molecule in its optimised geometry**,** calculated using the same conditions. A negative adsorption energy thus indicates that adsorption of the molecule at the surface is energetically favourable.

2.6.2 Modelling the Interaction between the Adsorbing Molecules and Mineral Surfaces

The adsorption of the molecules to the surfaces of the two iron oxide minerals was investigated through static energy minimisation techniques using the METADISE simulation program. In order to allow the relaxed organic molecule to accommodate itself onto the surface, we generated surface supercells of sufficient sizes to ensure the absence of any computational artefacts due to the periodic boundary conditions parallel to the surface. If the cells were too small, the adsorbed organic molecule could have interfered with its images in the periodically repeated surface cell, which would affect the geometries and energies. The generated bigger surface systems without adsorbates were modelled using the two minimisation methods of Conjugated Gradients (CG), and Newton Raphson consecutively. However, we also tested the use of only the Newton Raphson method to obtain the converged system energy but we did not find any difference in structures or energies. As initial use of the CG method is much

faster, we therefore decided to use both Conjugated Gradients and Newton Raphson techniques consecutively to relax the surfaces and calculate the adsorption energy.

In each case, we first scanned the adsorbing molecule over the surfaces by generating a grid of locations of approximately 1 Å apart and at each grid point the program calculated the interaction energy of the surface with the organic molecule without geometry optimization. The three initial lowest energy positions thus identified are then fully optimised to obtain the relaxed structures and energies of the surface/ adsorbate system. Here, we use only the Newton Raphson method for the relaxation of the surface. Although this increases the computational time, because of the need to calculate the second derivate term, the calculated adsorption energies using initially the Conjugated Gradients method followed by the Newton Raphson method did not match those from previous work. Upon comparing the adsorption energy uses both Conjugated Gradient and Newton Raphson methods with the calculated adsorption energy using only the Newton Raphson method we found that the latter protocol gives energies that are both lower and closer to those from previous work.

In our calculations, we have calculated a large number of initial starting positions through introducing two or three different heights and eight different orientations for each molecule at the different surface sites to identify the energetically most favourable location, and configuration, rather than a local minimum.

2.7 Potentials Used in This Work

2.7.1 Potentials of Iron Oxide Polymorphs

The potentials used in this study are shown in **Table 2.1**

Table 2.1: Interatomic potentials used to model the iron oxides.

Interactions		**Charges(e)**		**Core-Shell interactions (eV Å^{-2})**
		Core	**Shell**	
Fe(III)		+3		
O(oxygen)		0.86	-2.86	74.72
O(oxygen)		0.21	-2.21	27.29
Buckingham Potential				
Potential Types	**Interactions**	**A /eV**	**ρ/ Å**	**C/ eV Å^6**
Type1	Fe^{+3}-O^{-2}	1677.94	0.3084	0.0
Type2	Fe^{+3}-O^{-2}	1102.4	0.3299	0.0
Type3	Fe^{+3}-O^{-2}	1102.4	0.3299	0.0
	O^{-2}-O^{-2}	22764.00	0.14900	27.88

The Fe^{+3}-O^{-2} in type 2 and 3 are the same but the spring constants are different: with IP2 it is 74.92 and IP3 it is 27.29. On IP1 and IP2 we have used the same spring constant but the Fe^{+3}-O^{-2} is different as seen in **Table 2.1**.

2.7.2 Comparison of Interatomic Potentials Available for Iron Oxide Polymorphs

First we have compared three different interatomic potential models to describe the structures and properties of four iron oxide polymorphs, namely α-Fe_2O_3 (hematite), β-Fe_2O_3, γ-Fe_2O_3 (maghemite) and ε-Fe_2O_3, which in the following discussion we will refer to them as IP1, IP2, IP3.

In the first potential (IP1) Fe(II)-O were used from Lewis and Catlow (1985), Fe(III)-O scaled for this work , and second potential (IP2) and (IP3) parameters used in this study for the Fe(II)(III)-O were derived by Lewis and Catlow (Lewis and Catlow, 1985),while the Fe(II)(III)-OH were derived by de Leeuw and Cooper (de Leeuw & Cooper, 2007). The complete potential model used in this work is given in **Table 2.1**. In addition, these materials have been studied experimentally and their crystallographic structures are well characterised (Yanagihara *et al*., 2006; Woodley *et al*., 1999; Cox *et al*., 1962; Finch & Sinha, 1957; Shin, 1998; Chaneac & Jolivet, 1998; Shmakov *et al*., 1995).

The structures of the four polymorphs have been energy minimised, using constant pressure minimisation with all the three potentials, where we have considered cell volume, angles, Fe-O bond distances and relative stabilities of the four polymorphs and compared with the experimental data, all reported in **Table 2.2**.

Table 2.2: Comparison of the calculated and experimental average Fe-O bond distances (r/Å), cell volumes (V/ Å^3), and lattice cell parameters a, b, c of α-Fe_2O_3, β-Fe_2O_3, γ-Fe_2O_3, and ε-Fe_2O_3.

α-Fe_2O_3				
		Interatomic potentials		
Parameters	**Exp**	**IP1**	**IP2**	**IP3**
V	302.50	307.60	296.44	296.60
a	5.04	5.13	5.06	5.06
b	5.04	5.13	5.06	5.06
c	13.75	13.49	13.37	13.36
α	90.00	90.00	90.00	90.00
β	90.00	90.00	90.00	90.00
γ	120.00	120.00	120.00	120.00
(Fe-O)oct	2.03	2.04	2.02	2.02
β-Fe_2O_3				
		Interatomic potentials		
Parameters	**Exp**	**IP1**	**IP2**	**IP3**
V	603.70	501.20	524.80	511.50
a	5.56	5.67	5.58	5.57
b	5.56	5.67	5.58	5.57
c	22.55	18.01	19.48	19.02
α	90.00	90.00	90.00	90.00
β	90.00	90.00	90.00	90.00
γ	120.00	120.00	120.00	120.00
(Fe-O)oct	2.64	2.09	1.99	2.19
(Fe-O)teh	2.45	2.04	2.06	2.03
γ-Fe_2O_3				
		Interatomic potentials		
Parameters	**Exp**	**IP1**	**IP2**	**IP3**
V	1743.90	1816.30	1736.70	1670.60
a	8.35	8.49	8.36	8.49
b	8.36	8.50	8.36	8.49
c	25.04	25.14	24.85	23.16
α	90.00	90.00	90.00	90.00

Table 2.2-(Continued)

B	90.00	90.00	90.00	90.00
γ	90.00	90.00	90.00	90.00
(Fe-O)oct	2.03	2.04	2.01	2.05
(Fe-O)teh	1.88	1.91	1.88	1.91
ε-Fe_2O_3				
		Interatomic potentials		
Parameters	**Exp**	**IP1**	**IP2**	**IP3**
V	422.60	427.90	418.20	417.70
a	5.09	5.32	5.11	5.10
b	8.79	8.98	8.70	8.70
c	9.44	8.95	9.42	9.50
α	90.00	90.0	90.00	90.00
β	90.00	90.0	90.00	90.00
γ	90.00	90.0	90.00	90.00
(Fe-O)oct	2.07	2.07	2.07	2.07
(Fe-O)teh	2.00	2.03	2.00	1.96

The pair potential which best describes the structural properties of all the systems studies is that proposed by Lewis and Catlow (IP2) (Lewis & Catlow, 1985). We shall therefore use this pair potential to investigate the vacancy ordering in the structure of maghemite (γ-Fe_2O_3). In addition, in the case of α-Fe_2O_3, experimental data on elastic constants (bulk modulus and shear modulus) (Liebermann & Schreiber, 1968; Anderson *et al*., 1968) are available, which have been compared with our results and found to be in reasonable agreement. Although we have calculated these properties for the other iron oxide polymorphs as well there is no experimental data to compare with.

Table 2.3: Bulk modulus, K, and shear modulus, μ, for α-Fe_2O_3, β-Fe_2O_3, γ-Fe_2O_3, and ε-Fe_2O_3.

Polymorphs	Experimental		Gulp	
	K(GPa)	μ (GPa)	K(GPa)	μ (GPa)
α-Fe_2O_3	207.0	91.0	262.7	120.6
β- Fe_2O_3	-	-	25.9	-8.2
γ- Fe_2O_3	-	-	217.1	98.6
ε- Fe_2O_3	-	-	224.8	77.7

Finally, we have calculated the lattice energies to compare the relative stabilities of the four Fe_2O_3 polymorphs, whose values are reported in **Table 2.4**.

Table 2.4: Lattice energies per formula unit of Fe_2O_3 polymorphs (kJ/mol^{-1})

	IP1	IP2	IP3
α-Fe_2O_3	0.0	0.0	0.0
β-Fe_2O_3	469.1	392.5	434.4
γ-Fe_2O_3	55.9	26.6	0.4
ε-Fe_2O_3	39.0	13.1	15.8

All three potential models predict that the α-Fe_2O_3 polymorph is the most stable, in agreement with experiment (Cornell & Schwertmann, 2003), with the order of stability of the Fe_2O_3 polymorphs α-Fe_2O_3 > ε -Fe_2O_3 > γ-Fe_2O_3 > β-Fe_2O_3 according to IP1and IP2 , whereas IP3 predicts α-Fe_2O_3 > γ-Fe_2O_3 > ε -Fe_2O_3 > β-Fe_2O_3.

2.7.3 Potentials for Pollutants

The consistent valence force field (cvff) potential parameters are used to describe the organic molecules (Dauber-Ostguthorpe *et al*., 1988).

In this work, the short range interactions within the mineral and the interactions between the organic molecule and the mineral surface were modelled using the Buckingham potential. The covalent interactions between neighbouring atoms in the organic molecule are calculated using the Morse potential, and Lennard-Jones potentials for interactions between surface oxygen atoms and the carbon and hydrogen atoms of both methanoic and hydroxyethanal molecules.

(a) (b)

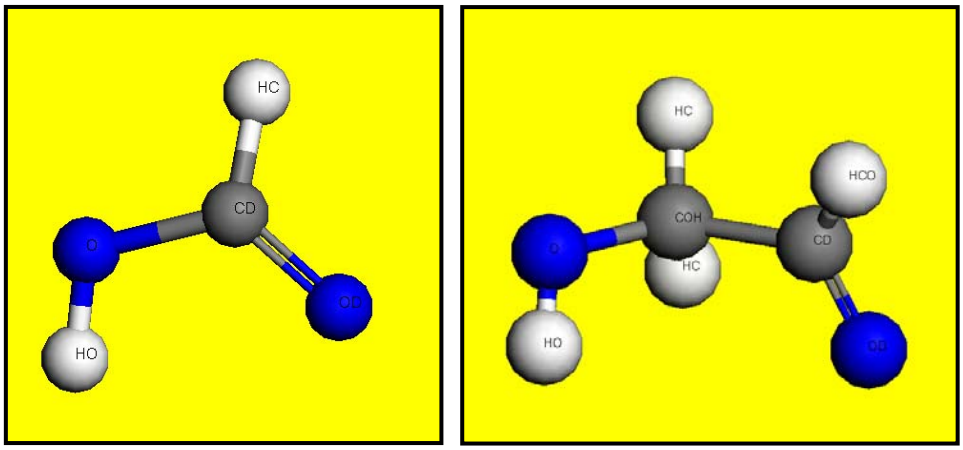

Figure 2.11: The structures of organic molecules. (a) methanoic acid and (b) hydroxyethanal. The name of the atoms as labelled in Tables 2.5 and 2.6, respectively.

Methanoic acid

Table 2.5: Interatomic potentials used to model the methanoic acid molecule with the iron oxide minerals.

Interactions	**Charges(e)**		**Core-Shell interactions (eV Å^{-2})**
	Core	**Shell**	
OX(oxygen)(surface)	1.000	-3.000	60.78
Fe(III)(surface)	3.000		
OH	0.9000	-2.300	74.92038
H	0.4000		
OD	-0.380		
O	-0.380		
CD	0.310		
HC	0.100		
HO	0.350		
Buckingham Potential			
Ion Pair	**A /eV**	**ρ/ Å**	**C/ eV Å^6**
Fe(III)-OX(shell)	1102.4	0.3299	0.0
Fe(III)-OH	771.7	0.3299	0.0
Fe(III)-OD	209.5	0.3299	0.0
OX (shell)-OD	1199.40	0.213	24.55
OX(shell)-O	11994.0	0.213	24.55
OH(shell)-OD	8395.8	0.213	12.27
OH(shell)-O	8395.8	0.213	12.27
OX(shell)-CD	2237.5	0.26	0.0
OH(shell)-CD	1566.25	0.26	0.0

Table 2.5-(continued)

OX(shell)-HO	396.27	0.25	0.0
OX(shell)-HC	396.27	0.25	0.0
OH(shell)-HO	311.97	0.25	0.0
OH(shell)-HC	311.97	0.25	0.0
Ion Pair	**Lennard-Jones Potential Parameters**		
	A(eV Å^{12})		**B(eV Å^{6})**
OD-H	1908.1		5.55
O-H	1908.1		5.55
OD-OD	11822.565		21.613
OD-CD	38994.306		35.232
OD-HC	1908.103		5.55
OD-HO	1908.103		5.55
OD-O	11822.565		21.613
O-CD	38994.306		35.232
O-HC	1908.103		5.55
O-HO	1908.103		5.55
O-O	11822.565		21.613
Ion Pair	**Mores Potential Parameters**		
	D (eV)	**A(Å^{-1})**	**r_0(Å)**
H-OH	7.0525	3.1749	0.9258
CD-HC	4.66	1.77	1.10
O-HO	4.08	2.28	0.96
CD-O	4.29	2.0	1.37
CD-OD	6.22	2.06	1.23
Ion Pair	**Three-Body Potential Parameters**		
	K_{ijk}(eV rad^{-2})		**Θ_0(^{0})**
O-HO-CD	4.29		112.0

Table 2.5-(continued)

HC-CD-O	4.72	110.0
OD-CD-HC	4.72	120.0
OD-CD-O	12.45	123.0

Key: OH mineral hydroxyl oxygen, H mineral hydroxyl hydrogen, OX mineral oxygen, Fe (III) mineral iron, CD organic carbon, OD organic doubly bonded oxygen, O organic oxygen of the hydroxyl group, HO organic hydrogen of the hydroxyl group, HC organic hydrogen attached to the carbon.

Hydroxyethanal

Table 2.6: Interatomic potentials used to model the hydroxyethanal molecule with the iron oxide minerals.

Interactions	**Charges(e)**		**Core-Shell interactions (eV Å^{-2})**
	Core	**Shell**	
OX (oxygen)(surface)	1.000	-3.000	60.78
Fe(III)(surface)	3.000		
OH	0.900	-2.300	74.92038
H	0.400		
COH	-0.17		
HCO	0.213		
OD	-0.380		
O	-0.380		

Table 2.6-(continued)

CD	0.167		
HC	0.100		
HO	0.350		
Buckingham Potential			
Ion Pair	**A /eV**	**ρ/ Å**	**C/ eV Å^6**
Fe(III)-OX(shell)	1102.4	0.3299	0.0
Fe(III)-OH	771.7	0.3299	0.0
Fe-(III)-COH	93.7	0.3299	0
Fe(III)-OD	209.5	0.3299	0
Fe(III)-O	209.5	0.3299	0
OX (shell)-COH	5365.73	0.213	25.26
OX(shell)-OD	11994.0	0.213	24.55
OX(shell)-O	11994.0	0.213	24.55
OH(shell)-COH	3756.0	0.213	12.63
OH(shell)-OD	8395.8	0.213	12.27
OH(shell)-O	8395.8	0.213	12.27
OX(shell)-CD	2237.5	0.26	0
OH(shell)-CD	1566.25	0.26	0
OX(shell)-HCO	396.27	0.25	0
OX(shell)-HO	396.27	0.25	0
OX(shell)-HC	396.27	0.25	0
OH(shell)-HCO	311.97	0.25	0
OH(shell)-HO	311.97	0.25	0
OH(shell)-HC	311.97	0.25	0
Ion Pair	**Lennard-Jones Potential Parameters**		
	A(eV Å^{12})	B**(eV Å^6)**	

Table 2.6-(continued)

COH-H	1908.1	5.55
OD-H	1908.1	5.55
O-H	1908.1	5.55
OD-OD	11822.565	21.613
OD-CD	38994.306	35.232
OD-HC	1908.103	5.55
OD-HCO	1908.103	5.55
OD-HO	1908.103	5.55
OD-O	11822.565	21.613
O-CD	38994.306	35.23
O-HC	1908.103	5.55
HC-HC	1908.103	5.55
O-HCO	1908.103	5.55
O-HO	1908.103	5.55
O-O	11822.565	21.613

Ion Pair	**Mores Potential Parameters**		
	D (eV)	**A($Å^{-1}$)**	**r_0(Å)**
CD-HCO	4.66	1.77	1.10
H-OH	7.0525	3.1749	0.9258
COH-O	4.12	2.0	1.42
COH-HC	4.66	1.771	1.105
O-HO	4.08	2.28	0.96
CD-OD	6.22	2.06	1.23
CD-COH	3.26	1.93	1.52

Ion Pair	**Three-Body Potential Parameters**	
	K_{ijk}(eV rad^{-2})	**$\Theta_0(^0)$**
OD-CD-HCO	4.72	120.0

Table 2.6-(continued)

HC-COH-HC	3.39	106.4
OD-CD-COH	5.84	120.0
HO-O-COH	5.02	106
O-COH-HC	4.89	109.5
CD-COH-HC	3.86	109.5
HCO-CD-COH	3.86	120.0
Ion Pair	**Four-Body Potential Parameters**	
	K_{ijkl}(eV)	
HO-O-COH-CD	0.39	
HO-O-COH-HC	0.39	

Key: OH mineral oxygen, H mineral hydroxyl hydrogen, OX mineral oxygen, Fe (III) mineral iron, CD organic carbon attached to the doubly bonded oxygen, OD organic doubly bonded oxygen, O organic oxygen of hydroxyl group, HO organic hydrogen of the hydroxyl group, COH organic carbon attached to the hydroxyl group, HC organic hydrogen attached to COH, HCO organic hydrogen attached to CD.

Arsenate

The interactions between an arsenate molecule and both the hematite and maghemite surfaces shown in **Table 2.7**, The Buckingham potentials were used for interactions between surface Fe atoms and the oxygen atoms of the arsenate molecule and between the As (V) and surface oxygen atoms, and Morse potentials for interactions between hydrogen and oxygen, while the three-body potentials for the interactions between the As (V) and oxygen atoms of the molecule.

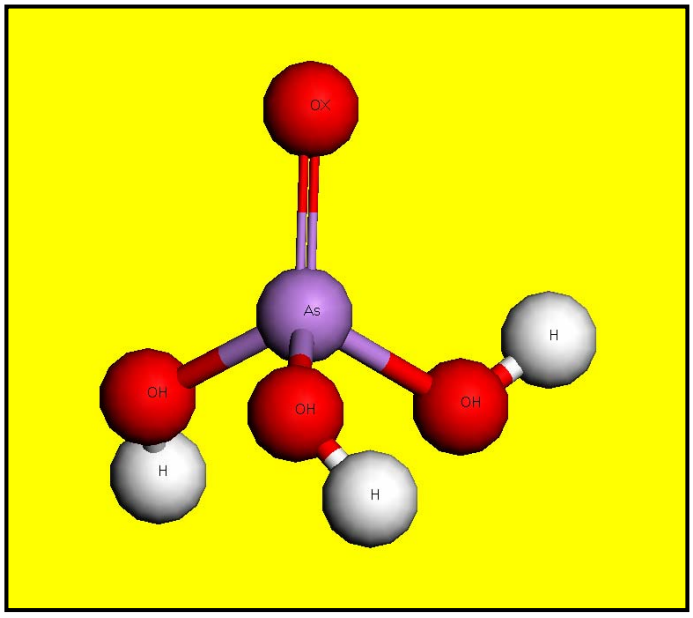

Figure 2.12: The structure of arsenate molecule, the name of the atoms as labeled in Table 2.7.

Table 2.7: Interatomic potentials used to model the arsenate molecule with the iron oxide minerals.

Interactions	**Charges(e)**		**Core-Shell interactions ($eV\ Å^{-2}$)**
	Core	**Shell**	
As (IV)	5.000		
OX(oxygen)(surface)	1.000	-3.000	60.78
Fe(III)(surface)	3.0		
OH	0.9000	-2.300	74.92038
H	0.4000		
Buckingham Potential			
Ion Pair	**A /eV**	**ρ/ Å**	**C/ $eV\ Å^6$**
As(IV)-OX(shell)	2796.57	0.2775	0.0
As(IV)-OH(shell)	1957.60	0.2775	0.0
Fe(III)-OX(shell)	1102.4	0.3299	0.0
Fe(III)-OH	771.7	0.3299	0.0
OX(shell)-H	396.27	0.25	0.0
OH(shell)-H	311.97	0.25	
Ion Pair	**Mores Potential Parameters**		
	D (eV)	**$A(Å^{-1})$**	**$r_0(Å)$**
H-OH	7.0525	3.1749	0.9258
Ion Pair	**Three-Body Potential Parameters**		
	$K_{ijk}(eV\ rad^{-2})$		**$Θ_0(^0)$**
As-OX-OX	5.5		109.5

2.8 Chapter Conclusions

This chapter has described the computational techniques and modelling methods employed throughout this study, including the interatomic potentials used to describe the interactions in the bulk and the surfaces of the iron oxide systems studied in this thesis.

Chapter 3

Vacancy ordering in the Structure of Maghemite (γ-Fe_2O_3)

Abstract

The crystal structure of the iron oxide γ-Fe_2O_3 is usually reported in either the cubic system (space group $P4_332$) with partial Fe vacancy disorder or in the tetragonal system (space group $P4_12_12$) with full site ordering and $c/a \approx 3$. Using a supercell of the cubic structure, we obtain the spectrum of energies of all the ordered configurations which contribute to the partially disordered $P4_332$ cubic structure. Our results show that the configuration with space group $P4_12_12$ is indeed much more stable than the others, and that this stability arises from a favourable electrostatic contribution, as this configuration exhibits the maximum possible homogeneity in the distribution of iron cations and vacancies. Maghemite is therefore expected to be fully ordered in equilibrium, and deviations from this behaviour should be associated with metastable growth, extended anti-site defects and surface effects in the case of small nanoparticles.

3.1 Introduction

Maghemite (γ-Fe_2O_3) is the second most stable polymorph of Fe_2O_3. Contrasting with antiferromagnetic hematite (α-Fe_2O_3), maghemite exhibits ferrimagnetic ordering with a net magnetic moment (2.5 μ_B per formula unit) and high Néel temperature (~950 K), which together with its chemical stability and low cost led to its wide application as magnetic pigment in electronic recording media since the late 1940's (Dronskowski, 2001). Maghemite nanoparticles are also widely used in biomedicine, because their magnetism allows manipulation with external fields, while they are biocompatible and potentially non-toxic to humans (Pankhurst *et al*., 2003; Levy *et al*., 2008). Another promising application is in the field of spintronics, where it has been suggested that γ-Fe_2O_3 can be used as a magnetic tunnelling-barrier for room-temperature spin-filter devices (Wiemann *et al*., 2000; Yanagihara *et al*., 2006).

Maghemite occurs naturally in soils as a weathering product of magnetite (Fe_3O_4), to which it is structurally related (Cornell & Schwertman,2003). Both maghemite and magnetite exhibit a spinel crystal structure, but while the latter contains both Fe^{2+} and Fe^{3+} cations, in maghemite all the iron cations are in trivalent state, and the charge neutrality of the cell is guaranteed by the presence of cation vacancies. The unit cell of magnetite can be represented as $(Fe^{3+})_8[Fe^{2.5+}]_{16}O_{32}$, where the brackets () and [] designate tetrahedral and octahedral sites, respectively, corresponding to 8a and 16d Wyckoff positions in space group Fd3m. The maghemite structure can be obtained by creating 8/3 vacancies out of the 24 Fe sites in the cubic unit cell of magnetite. These vacancies are known to be located

in the octahedral sites (Waychunas ,1991) and therefore the structure of maghemite can be approximated as a cubic unit cell with composition $(Fe^{3+})_8[Fe^{3+}_{5/6}\ _{1/6}]_{16}O_{32}$.

The nature and degree of ordering of the iron vacancies in the octahedral sites has been the subject of investigations for several decades. If the cation vacancies were randomly distributed over the octahedral sites, as it was initially assumed, the space group would be Fd3m like in magnetite (Hagg, 1935; Verwey, 1935). The first indication of a departure from the Fd3m symmetry was reported by Haul and Schoon (Haul & Schoon ,1939), who noticed extra reflections in the powder diffraction pattern of maghemite prepared by oxidising magnetite. Braun (Braun, 1952) later noticed that maghemite exhibits the same superstructure as lithium ferrite ($LiFe_5O_8$), which is also a spinel with unit cell composition $(Fe^{3+})_8[Fe^{3+}_{3/4}Li^{1+}_{1/4}]_{16}O_{32}$, and suggested this was due to similar ordering in both compounds. In the space group $P4_332$ of lithium ferrite, there are two types of octahedral sites, one with multiplicity 12 in the unit cell, and one with multiplicity 4, which is the one occupied by Li. In maghemite, the same symmetry exists if the Fe vacancies are constrained to these Wyckoff 4b sites, instead of being distributed over all the 16 octahedral sites. It should be noted, however, that some level of disorder persists in this structure, as the 4b sites have fractional (1/3) iron occupancies.

Van Oosterhout and Rooijmans (van Oosterhout & Rooijmans, 1958) first suggested a spinel tetragonal superstructure with c/a=3, where the Fe atoms are completely ordered. A neutron diffraction study by Greaves (Greaves, 1983)

confirmed a higher degree of ordering than the one implied by the cubic $P4_332$ structure, and described this departure as a tetragonal distortion. The positions of the vacancies in the fully-ordered maghemite structure were obtained by Shmakov *et al.* (1995) using synchrotron X-ray diffraction. This ordered maghemite structure has the tetragonal space group $P4_12_12$ with a=8.347 Å and c=25.042 Å (spinel cubic cell tripled along the c axis). The ion coordinates in the $P4_12_12$ structure have been recently refined by Jorgensen *et al.* based on synchrotron X-ray powder diffraction data (Jorgensen *et al*., 2007).

Despite this progress in the structure determination of maghemite, the phenomenon of vacancy ordering in the lattice is not yet fully understood. It is not clear, for example, under which conditions, if any, vacancy disorder occurs. It has been suggested that the degree of ordering depends on crystal size, and that very small particles of maghemite do not show vacancy ordering (Cornell & Schwertman, 2003; Bastow *et al*., 2009), although a recent investigation of needle-shaped maghemite nanoparticles with average size 240nm x 30nm has found the same tetragonal distortion with space group $P4_12_12$ as in the ordered crystal (Somogyvari *et al*., 2002). The thermodynamics of vacancy ordering in maghemite has not been investigated so far, in part because of the difficulty to control experimentally the level of ordering of the iron vacancies.

In this chapter, we present a computational investigation of the energetics of vacancy ordering in maghemite. We will show that a fully ordered structure with tetragonal space group $P4_12_12$ is indeed the most stable configuration among all the possible ionic arrangements that are compatible with the partially disordered

$P4_332$ structure, and that this stability arises from a most favourable electrostatic contribution.

3.2 Computational Details

The thermodynamics of ion disorder was investigated by the direct evaluation of the lattice energies of different ionic configurations, using interatomic potentials. The investigation of site-disordered structures using computer-modelling methods poses the problem of the large number of possible configurations that can exist for a particular supercell. We have used the methodology implemented in the program SOD (Site Occupancy Disorder (Grau-Crespo *et al*., 2007)), which generates the complete configurational space for each composition of the supercell, and then extracts the subspace of symmetrically equivalent configurations. The criterion for the equivalence of two configurations is the existence of an isometric transformation that converts one configuration into the other and the transformations considered are simply the symmetry operators of the parent structure (the structure from which all configurations are derived via site substitution). This method typically reduces the size of the configurational space by one or two orders of magnitude, making the problem more tractable.

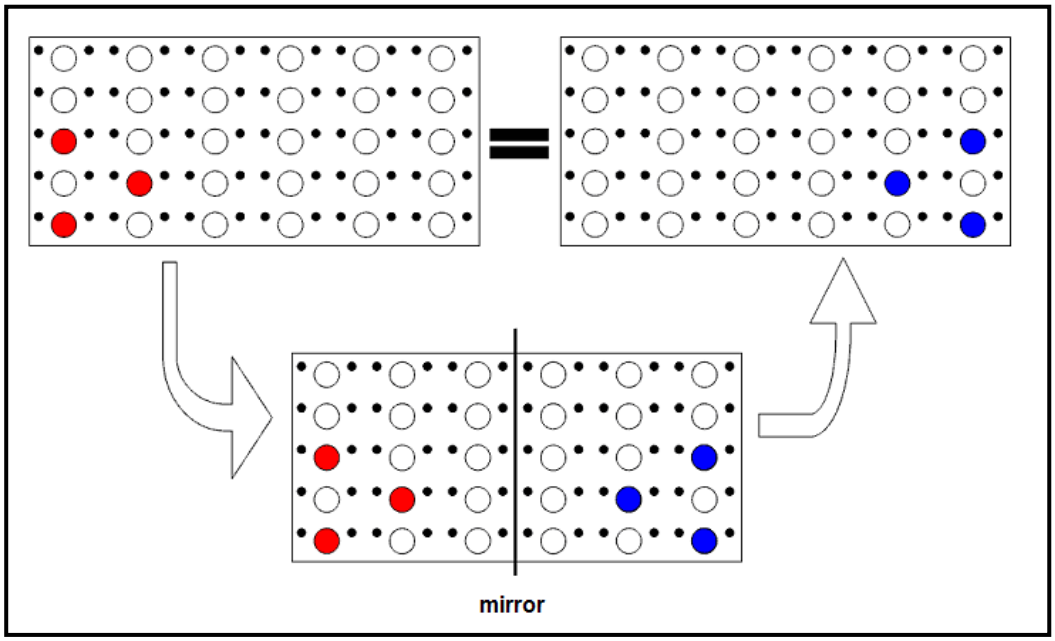

Figure 3.1: Illustration of identical configurations related by an isometric 12 transformation.

3.3 Results and Discussion

3.3.1 Configurational Spectrum

Our starting point for the calculations of the ordering of cation vacancies in γ-Fe_2O_3 is the partially disordered cubic spinel structure with space group $P4_332$ initially suggested by Braun (1952), where Fe ions and vacancies are distributed in the Wyckoff 4b octahedral positions. This structure is equivalent to lithium ferrite $LiFe_5O_8$, where the 4b positions are occupied by the Li cations. For this reason, we will call these positions "L" (for lithium) sites, even though we have no Li in the structures investigated in this work. An iron occupancy of 1/3 on the L sites makes the stoichiometry $Fe^{L}_{1/3}Fe_5O_8$. In the partially disordered cubic cell

of maghemite, the 2.667 (or 8/3) iron vacancies are randomly distributed over the four L sites, together with 1.333 (or 4/3) iron cations. In order to have integer occupancies, we triple the unit cell along one axis (chosen to be *c*, to be consistent with the traditional convention for tetragonal systems). This 1x1x3 supercell thus contains 8 vacancies, which are now distributed, together with 4 iron cations, over the 12 L sites, and the coordinates of these positions for the 1x1x3 supercell are given in **Table 3.1**.

Table 3.1: Coordinates of the L sites in the calculation supercell. These positions correspond to the Wyckoff 4b sites of cubic space group P4332, expanded to a 1x1x3 supercell.

Position Label	Coordinates		
	x	*y*	*z*
L1	7/8	3/8	1/24
L2	1/8	7/8	3/24
L3	5/8	5/8	5/24
L4	3/8	1/8	7/24
L5	7/8	3/8	9/24
L6	1/8	7/8	11/24
L7	5/8	5/8	13/24
L8	3/8	1/8	15/24
L9	7/8	3/8	17/24
L10	1/8	7/8	19/24
L11	5/8	5/8	21/24
L12	3/8	1/8	23/24

Note that there are 12 layers, perpendicular to the <001> direction, containing octahedral sites with only one L-type site in each layer per simulation cell (**Figure 3.2**).

The total number of combinations of the 4 Fe ions on the L sites of the supercell is 12!/(4! ×8!)=495, but only 29 of these are inequivalent, as determined using the SOD program. Table 3.2 lists the positions of the cations in each of the inequivalent configurations, together with their space groups, their degeneracies (how many times they are repeated in the full configurational space) and their relative lattice energies. This information defines a multi-configurational model of vacancy ordering in maghemite, which is capable of describing the two extreme cases: if the energies of all the configurations are very similar, or differ very little compared with the thermal energy at the equilibration temperature, then the system is expected to be fully disordered. On the other hand, if one of the configurations is much more stable than the others, then the system should be ordered. A number of intermediate situations can also be described within the same framework, depending on the distribution of configuration energies.

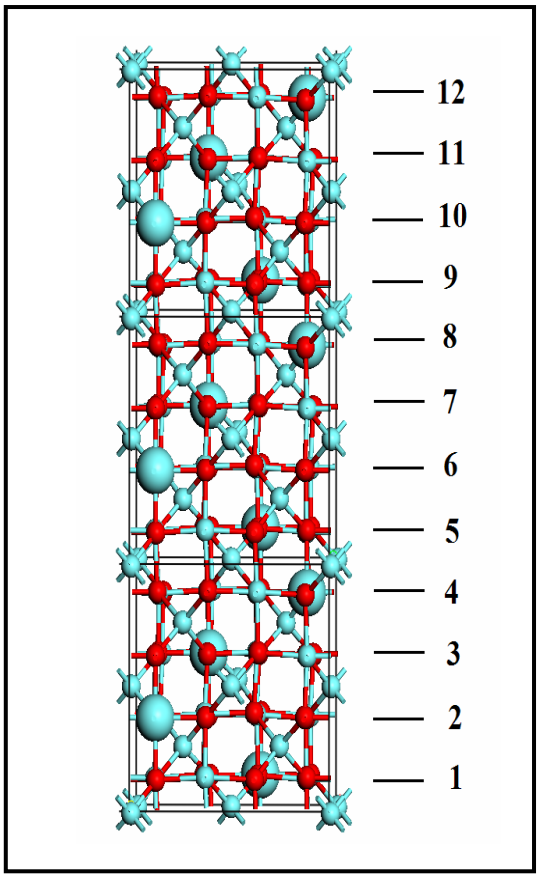

Figure 3.2: Possible positions for the iron vacancies in the 1x1x3 supercell. The 12 L sites, which should be populated with 4 iron ions and 8 vacancies, are marked as larger spheres.

Table 3.2: Fully ordered configurations in the 1x1x3 supercell. The labels of the iron positions in the L sites follow the convention given in Table 3.1. Energies are given with respect to the lowest energy configuration.

Iron positions	Degeneracy	Space group	ΔE/kJ.mol^{-1}
L1, L4, L7, L10	3	$P4_12_12$	0
L1, L3, L7, L9	6	$C222_1$	32
L1, L3, L7, L10	24	P1	53
L1, L5, L6, L10	12	$P2_1$	77
L1, L5, L6, L8	12	C2	87
L1, L3, L7, L11	12	C2	106
L1, L2, L5, L9	24	P1	116
L1, L3, L7, L8	24	P1	136
L1, L2, L5, L8	24	P1	149
L1, L2, L7, L8	6	$P2_12_12_1$	167
L1, L3, L6, L8	12	$P2_1$	182
L1, L2, L5, L10	12	$P2_1$	213
L1, L3, L5, L10	12	P1	215
L1, L2, L6, L7	12	C2	235
L1, L3, L7, L12	24	P1	276
L1, L3, L6, L7	24	P1	280
L1, L4, L5, L6	24	P1	310
L1, L3, L5, L7	12	C2	343
L1, L3, L4, L10	24	P1	380
L1, L3, L4, L7	24	P1	413
L1, L2, L5, L6	12	$P2_1$	425
L1, L2, L3, L8	12	C2	470
L1, L2, L3, L7	24	P1	501
L1, L3, L5, L6	24	P1	560
L1, L2, L3, L6	24	P1	608
L1, L3, L4, L6	12	$P2_1$	640
L1, L2, L4, L5	12	P1	652
L1, L2, L3, L5	24	P1	722
L1, L2, L3, L4	12	$P2_1$	847

The full configurational spectrum is shown in **Figure 3.3**. Only one of these configurations has the space group $P4_12_12$, found by Shmakov *et al*. (1995) for fully ordered maghemite. This configuration is indeed the most stable one, with a significant energetic separation from the second most stable configuration (32 kJ/mol). The energy range covered by the configurational spectrum is quite wide (~850 kJ/mol), indicating that full disorder is very

unlikely. A more detailed analysis of the consequences of this energy spectrum will be given in section 3.3.3.

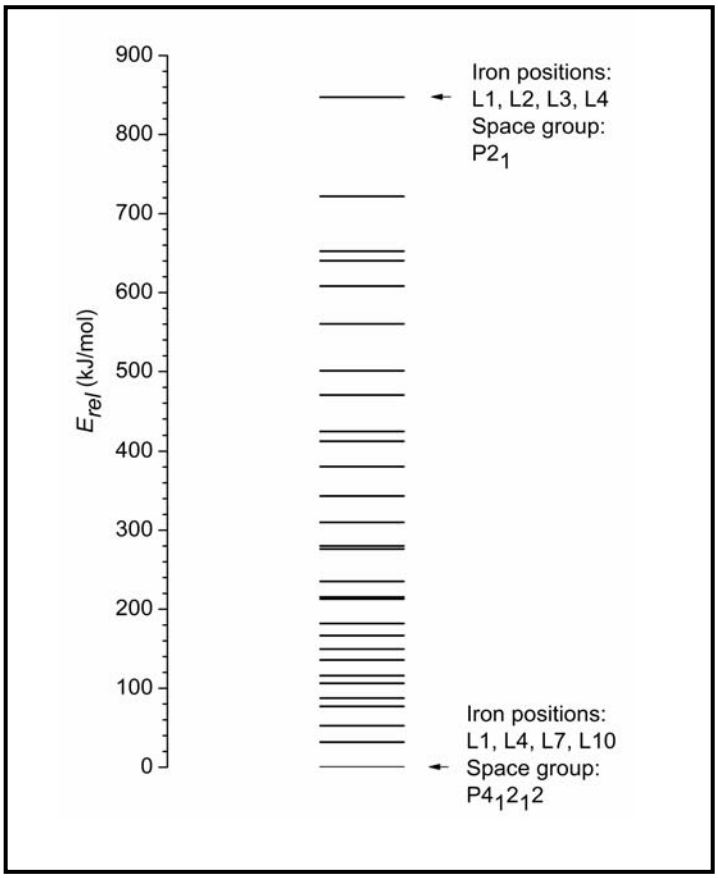

Figure 3.3: Energetic spectrum of configurations for 4 iron ions and 8 vacancies distributed over the L sites in a 1x1x3 supercell of the cubic maghemite structure.

3.3.2 The Fully Ordered Maghemite Structure: Origin of Its Stabilisation

The distinctive feature of the most stable configuration ($P4_12_12$) is the maximum possible homogeneity of iron cations and vacancies over the L sites. This configuration is the only one in which vacancies never occupy three consecutive layers; there are always two layers containing vacancies separated by a layer without vacancies, which instead contains Fe^{3+} cations in the L sites (*e.g.* positions L1 - L4 - L7 - L10) and the $P4_12_12$ configuration is therefore the one that minimizes the electrostatic repulsion between these cations.

It is possible to check that the electrostatic interactions indeed dominate the relative stability of the different configurations over the whole spectrum: the total energies correlate well with the Coulomb-only energies obtained using formal charges for all ions (**Figure 3.4**). The polarization of the anions is mainly responsible for the difference in the two energy scales, as polarization is known to compensate for the introduction of formal ionic charges in interatomic potential models (Gale, 1997). Deviations from the straight line are mainly caused by relaxation effects, which are stronger for the least stable configurations. Based on this analysis, it is not surprising that the least stable configuration is the one with the maximum segregation of iron ions and vacancies over the L sites (iron cations in consecutive layers, e.g. L1 to L4, and vacancies in consecutive layers, L5 to L12), with an energy 847 kJ/mol above the $P4_12_12$ configuration.

The relaxed cell parameters for the ordered $P4_12_12$ structure are a=8.359 Å and c=24.854 Å. The ratio $c/3a$=0.991 shows a small but significant deviation from the cubic symmetry. In the paper by Shmakov *et al*. (1995) no cell parameters are precisely given for the $P4_12_12$ structure, apart from stating that the cell is tripled along the c axis with respect to the original cubic structure (with a=8.347 Å). However, our result of $c/3a < 1$ is consistent with the observation by Greaves from neutron diffraction, that the tetragonal distortion accompanying vacancy ordering in maghemite slightly shrinks the crystal along the c axis with respect to a (Greaves, 1983). The bulk modulus obtained from our calculation of the ordered structure (211 GPa) is also in good agreement with the experimental value of Jiang *et al.* (203 GPa) (Jiang *et al*., 1998).

Finally, we should note that, besides the ordered structure described here, there is another possible distribution of vacancies that gives the same $P4_12_12$ symmetry. This distribution, which is not listed in **Table 3.2** as a configuration because it is partially disordered, can be described as follows. In the $P4_12_12$ space group, the L sites are divided into two symmetrically distinct positions, one with four-fold degeneracy, and the other with eight-fold degeneracy. While the ordered structure described above corresponds to full iron occupancy of the fourfold position, the distribution with half occupancy of the eightfold position also leads to $P4_12_12$ symmetry. However, we will show below that our calculated energetic spectrum of configurations strongly supports the full order scenario.

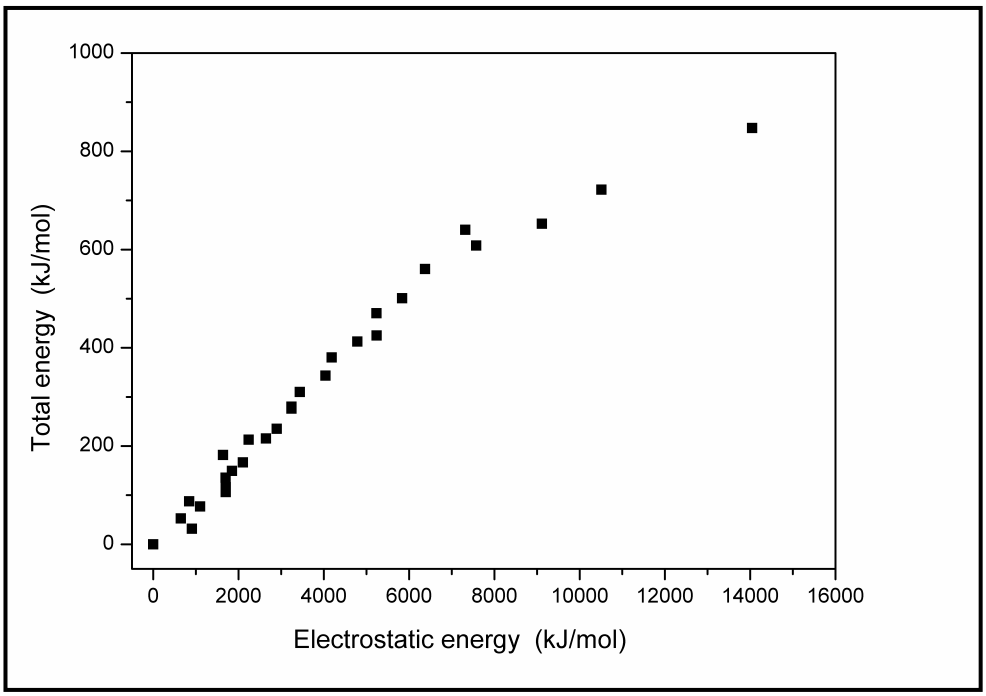

Figure 3.4: The relationship between the total lattice energies and the electrostatic energies of the different vacancy configurations.

3.3.3 Thermodynamics of Ordering from Canonical Statistical Mechanics

In order to interpret the energy differences in the configurational spectrum in terms of the degree of vacancy ordering in the solid, we can estimate the probability of occurrence of each independent configuration *m* as a function of its energy E_m, its degeneracy Ω_m and the equilibration temperature *T*, using Boltzmann's statistics (Grau-Crespo *et al*., 2000; Grau-Crespo *et al*., 2003; Grau-Crespo *et al*., 2007):

$$P_m = \frac{\Omega_m}{Z}\exp(-E_m / k_B T) \qquad \textbf{(3.1)}$$

where k_B=8.314×10^{-3} kJ/mol K is Boltzmann's constant, and

$$Z = \sum_m \Omega_m \exp(-E_m / k_B T) \qquad \textbf{(3.2)}$$

is the canonical partition function, which ensures that the sum of probabilities equals one. **Figure 3.5** shows the probabilities of the most stable configuration ($P4_12_12$) and of the second most stable configuration (with space group $C222_1$) as a function of temperature. At 500 K, a typical synthesis temperature for maghemite (Shmakov *et al*., 1995), the cumulative probabilities of all the configurations excluding the most stable $P4_12_12$ is less than 0.1%. This contribution increases slowly with temperature, but at 800 K this cumulative probability, which measures the expected level of vacancy disorder, is still less than 2%. At temperatures above 700-800 K maghemite transforms irreversibly to hematite (α-Fe_2O_3), and considering higher temperatures is therefore irrelevant. It thus seems clear that perfect crystals of maghemite in configurational equilibrium should have a fully ordered distribution of cation vacancies.

It is important to realize that, in real samples, several factors can prevent this ordering to develop completely. First, synthesis temperatures are typically too low and preparation times too short to allow complete equilibration of the ionic configurations during the synthesis. Second, the nature of the ordering in the structure means that disorder of anti-site type is expected to be abundant. For example, if the ordering sequence along the *c* axis (two layers including vacancies plus one layer including iron cations in the L sites) is locally broken every few unit cells (for example, leading to two layers with iron cations in the L sites separated by only with vacancy layer), the overall symmetry of the crystal is not

retained and the sample will appear disordered to diffraction methods. Third, in very small particles, surface effects might also alter the preferential distribution of cations, which could contribute to the absence of ordering reported in some maghemite nanoparticles (Cornell & Schwertman ,2003; Bastow *et al*., 2009) .

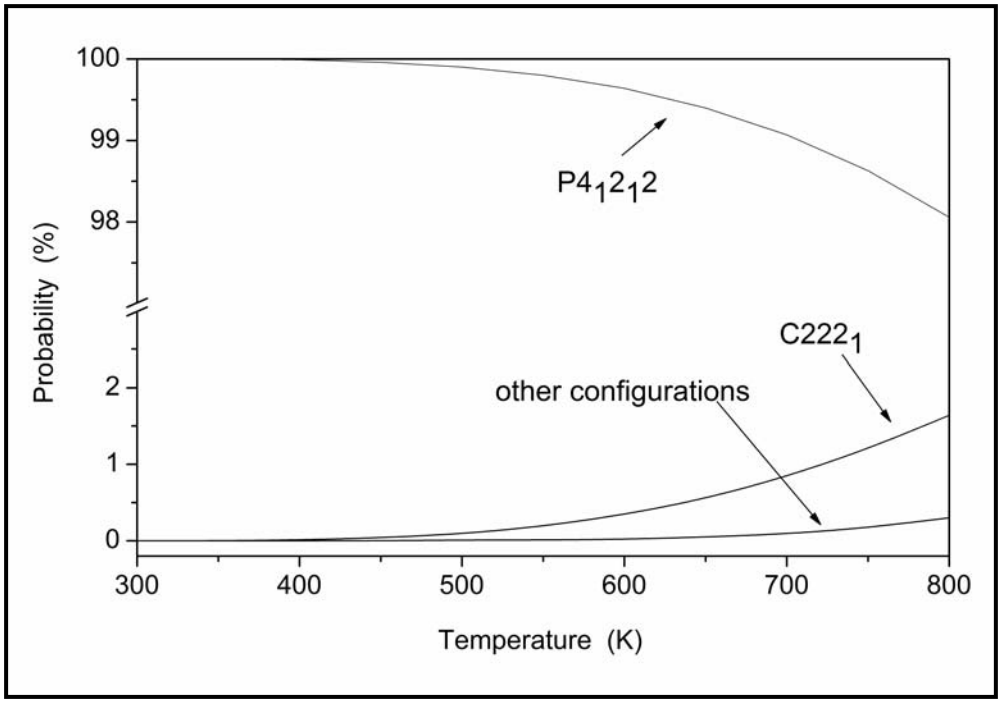

Figure 3.5: Probabilities of the configurations as a function of temperature.

3.4 Chapter Conclusions

In this work we present the first attempt to investigate the phenomenon of vacancy ordering in γ-Fe_2O_3 (maghemite) from an energetic point of view. As a result we can make the following observations.

- Our results show clearly that full vacancy ordering, in a pattern with space group $P4_12_12$, is the thermodynamically preferred situation in the bulk material. This stability arises from a minimal Coulombic repulsion

between Fe^{3+} cations for this configuration. However, deviation from perfect order can be expected because the low-temperature formation of maghemite does not guarantee an equilibrium growth of the crystals. Also, the presence of anti-site type disorder and surface effects in nanocrystals could contribute to deviation from the ideal ordering of the vacancies.

- In the next chapters we will present our calculations of the surfaces of maghemite, were we will use this ordered structure to create a range of low Miller index surfaces.

Chapter 4

Structures and Stabilities of Unhydrated and Hydroxylated Hematite and Maghemite surfaces

Abstract

Using the earlier results of our investigation of the vacancy-ordered structure of maghemite (γ-Fe_2O_3), which have been discussed in chapter three, in this chapter we continue to focus on maghemite by examining the surfaces, where we have studied a number of low index surfaces of pure maghemite (γ-Fe_2O_3) and compared their structures and stabilities with the dominant Fe_2O_3 polymorph hematite, which has been investigated already in several theoretical and experimental studies. Iron oxides are powerful catalysts and understanding of the surface stabilities and reactivities of these materials is interesting for different applications, not only in catalysis, but also in thin film preparation and corrosion, therefore. Our study also includes an examination of the hydroxylation of the surfaces of hematite and maghemite via dissociative adsorption of water, which has a significant effect on the surface stabilities and may affect the catalytic performance.

4.1 Introduction

Hematite and Maghemite are iron oxide polymorphs and of interest to various disciplines, including environmental and industrial applications, such as chemistry, biology and soil science (Cornell & Schwetmann, 2003) because their presence in the soil, lakes, rocks, sea and in rivers as weathering products of the Earth's crust makes these iron oxide minerals very important regulators of the concentration of organic and inorganic pollutants. Hematite α-Fe_2O_3, which is the most stable polymorph of iron oxide, has been used , for example, as a catalyst (Lei *et al*.,2005), in magnetic materials (Suber *et al*.,2005), as passivating thin films and pigments, as well as in environmental remediation agents (Hendy *et al*.,2005).

4.2 Surface and Hydration Energies

4.2.1 Dissociatively Adsorbed Water

There are two stages involved to calculate the surfaces stabilities. First, the crystals were cut to obtain different surface terminations and then the surface structures were relaxed and the surface energies calculated for the pure surfaces. In the second stage the surface is hydroxylated via dissociative adsorption of water molecules at the oxides surfaces. In this study, each surface was hydroxylated to full monolayer coverage, where a dissociated water molecule was adsorbed on every surface cation-oxygen pair as follows:

$$H_2O + O_o^x \rightarrow (OH)_o^{\bullet} + (OH)_i^{'} \qquad \textbf{(4.1)}$$

The O_o^x represent the lattice oxygen atom, $(OH)_o^{\bullet}$ refers to the hydroxylated lattice oxygen and the $(OH)_i^{'}$ is the interstitial hydroxyl group adsorbed onto the surface cation which is the Fe in this case. In our study, the interaction between the dissociated water and the surface is through bonding of an OH group to surface Fe ions and the proton to surface oxygen ions. There is another strong interaction which will occur during hydroxylation of the surface, namely hydrogen–bonding between surface species. The difference in energy between the hydroxylated surface and the bulk , and the energy of the dissociation of a water molecule, multiplied by the number of water molecules which have been added to the surface is used it to calculate the surface energy.

4.2.2 Hydration Energies

In order to determine whether dissociative adsorption of water is an energetically favourable process, we must calculate the energy of hydration. If the energy of hydration is exothermic, hydroxylation of the surface is predicted, whereas if the energy of hydration is endothermic, the surface is predicted to be more stable in its unhydroxylated state. The reaction which takes place during hydration of the surface can be defined as following:

$$\text{Unhydroxylated Surface} + \text{Water} \xrightarrow{\Delta E_{Hydration}} \text{Hydroxylated Surface} \qquad \textbf{(4.2)}$$

The energy of hydration cannot be determined directly by subtracting the total energy of reactants from the total energy of the products, since the oxygen atoms on the surface of the unhydroxylated surface have been represented by formal charges, whereas the hydroxyl oxygen in the hydroxylated surface are modelled using partial charges. This change in charge has to be accounted for when determining the energy of hydration. The following Born-Haber cycle illustrates the alternative route taken to calculate the energy of hydration:

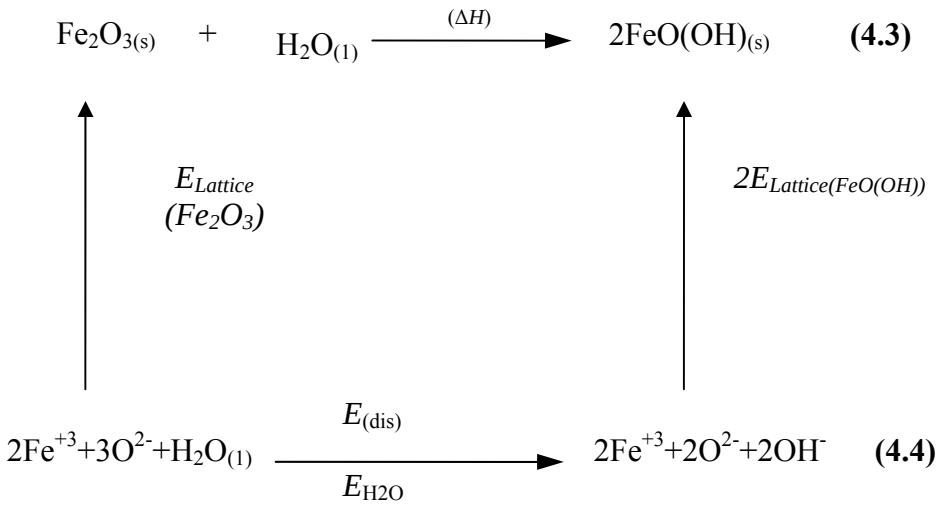

where ΔH is the experimental enthalpy of reaction (**4.3**) (Lide, 2000; Majzlan *et al*., 2003), which was found to be -6.3 kJ mol^{-1}, E_{latt} {FeO(OH)} and E_{latt} {Fe_2O_3}, are the calculated lattice energies of FeO(OH) and Fe_2O_3, which were calculated to be -6917.7 and -14510.6 kJ mol^{-1}, respectively. This energy cycle is used to obtain the energy of the reaction of one surface oxygen ion with one water molecule to form two hydroxy groups (de Leeuw & Cooper, 2007) :

$$O^{2-} + H_2O_{(l)} \xrightarrow{E_{H_2O}} 2OH^{-1} \qquad \textbf{(4.5)}$$

which is calculated at E_{H_2O} = -681.4 kJ mol^{-1}. This energy, which represents the energy for the dissociation of one water molecule, is used to calculate the energy released (per water molecule) upon adsorption of dissociative water at the iron (hydr)oxide surfaces as follows:

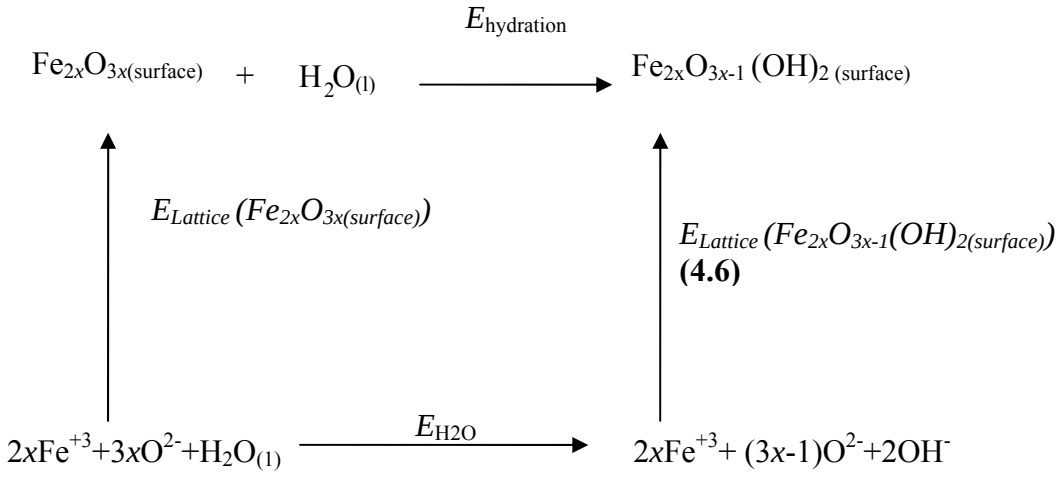

where $E_{latt}(Fe_{2x}O_{3x(surface)})$ is the energy of the dehydrated surface (shown here for hematite) and $E_{latt}(Fe_{2x}O_{3x-1}(OH)_{2(surface)})$ is the energy of hydroxylated surface, both obtained from the simulations, and E_{H2O} is the dissociation energy of one water molecule which was calculated from (eqn 4.5).

4.3 Hematite (α-Fe_2O_3)

The structure of hematite is the same as (α-Al_2O_3), the corundum structure, which is based on a hexagonal close-packed (hcp) anion packing. The unit cell is hexagonal, with a= b=5.04 Å and c=13.75Å, $\alpha=90^0$, $\beta=90^0$, $\gamma=120^0$ which on energy minimisation relaxed to a=b=5.06 Å, c=13.38 Å, $\alpha=\beta=90^0$ and $\gamma=120^0$. There is only one kind of Fe in hematite, Fe^{+3} which is located in octahedral sites.

(see **Chapter 1 and 2**) .In maghemite and hematite all the iron cations are in a trivalent state Fe(III) but in the γ-phase of iron oxide, the Fe^{3+} cations are arbitrarily distributed over octahedral and tetrahedral sites of the cubic close-packed oxygen anions (see **Chapter 3**).

The structure and the hydration of hematite α-Fe_2O_3 surfaces have been investigated before by a number of researchers (De Leeuw & Cooper, 2007; Jones *et al*., 2000; Lado-Touriño & Tsobnang, 2000; Parker *et al*., 1999; Rustad *et al*., 1999; Wasserman *et al*., 1999; Wasserman *et al*., 1997). Becker *et al*. (1996) have studied the electronic structure of the hematite surface using ab-initio methods to interpret experimentally collected STM data, but also to gain insight into atomic level changes in electronic structure that are associated with heterogeneous surface reactions. Their calculations show that the local electronic structure of surfaces can be very different from bulk electronic properties and that conclusion drawn from cluster calculations representing the bulk can be misleading. In addition, this theoretical approach helps to explain the increased reactivity at specific sites on hematite, such as steps and kinks, in terms of the electronic surface structure of this mineral. Bergermayer and Schweiger (2004) have used Density Functional Theory with the generalized gradient approximation to study the oxygen coverage, structure and thermodynamic stability of the {0001} surface of hematite as a function of temperature and oxygen pressure, while the stabilities, structures, electronic, and magnetic properties of the {0001} surfaces of hematite and iso-structural chromia or eskolaite (Cr_2O_3) have been investigated using ab initio methods by Rohrbach *et al*. (2004). Alvarez- Ramírez *et al*. (2004) have used four different DFT approximation levels, namely, the non-selfconsistent

Harris functional, the local spin-density approximation, LSDA, the PW91 or BP meta GGA functional and the hybrid B3LYP method, to study the geometric structure of the {0001} hematite surface and they found that the Harris functional can be used to explore the adequacy of a given model but not to provide an accurate enough structure of the relaxed hematite {0001} surface. Lo *et al*. (2007) have studied the structures of the clean and hydrated hematite α-Fe_2O_3 $\{11\bar{0}2\}$ surface using DFT. They have calculated free energies of the surfaces in chemical equilibrium with water as a function of temperature and oxygen partial pressure, using *ab initio* thermodynamics and they found that the hydroxyl groups lead to large differences in energetic stability and layer relaxations of the oxide substrate. Experimentally, Watanabe and Seto (1988) have studied the heat of immersion in water and the nature of the surface hydroxyl group of maghemite and hematite, whereas Eggleston *et al*. (2003) have studied the structure of hematite {0001} surface in aqueous media using scanning tunnelling microscopy and resonant tunnelling calculations to show that under some conditions the oxygen-termination can be present whereas the other studies find no evidence for an oxygen-termination. The structure and reactivity of the hydrated hematite {0001} surface were investigated via combined theoretical and experimental techniques using DFT and crystal truncation rod diffraction by Trainor *et al*. (2004) and their results show that the surface is dominated by two hydroxyl moieties: hydroxyls that are singly coordinated and doubly coordinated to Fe.

However, the most important growth and cleavage surfaces require attention, where the calculated surface energies are used to investigate the importance of surface relaxation and enable comparison with other works. Here the focus is on

two iron oxide minerals; hematite (α-Fe_2O_3) and maghemite (γ-Fe_2O_3). The emphasis is first on the experimentally defined surfaces and the creation of a wide range of surfaces with low Miller indices, since these surfaces have large inter-plane spacing, which are generally the most stable surfaces. For hematite we have studied the $\{0001\}$ and $\{10\bar{1}0\}$ surfaces (which is the same as the $\{01\bar{1}0\}$ surface), as well as the $\{11\bar{2}0\}$, $\{10\bar{1}1\}$ and $\{01\bar{1}2\}$ surfaces.

4.3.1 Dehydrated Surfaces

Table 4.1: Calculated surface energies (Jm^{-2}) and hydration energies ($kJmol^{-1}$) of dehydrated and hydroxylated hematite surfaces.

Surface	Termination	γ_{pure}	$\gamma_{dissociative}$	$E_{dissociative}$
$\{0001\}$Fe	Fe	1.78	1.21	-75.8
$\{0001\}$Ox	Ox	2.63	0.51	-189.0
$\{10\bar{1}0\}$a	Fe/Ox	1.99	1.01	-80.5
$\{10\bar{1}0\}$b	Fe/Ox	3.19	1.40	-114.1
$\{10\bar{1}1\}$a	Fe/Ox	2.34	0.67	-119.3
$\{10\bar{1}1\}$b	Fe/Ox	2.64	1.68	-185.1
$\{10\bar{1}1\}$c	Fe/Ox	2.75	1.56	-187.6
$\{11\bar{2}0\}$Ox	Ox	2.03	0.81	-107.0
$\{01\bar{1}2\}$a	Fe/Ox	1.88	0.97	-87.9
$\{01\bar{1}2\}$b	Fe/Ox	2.36	1.15	-75.2
$\{01\bar{1}2\}$c	Fe/Ox	2.75	1.02	-105.5
$\{11\bar{2}1\}$a	Fe/Ox	1.93	0.94	-79.1
$\{11\bar{2}1\}$b	Fe/Ox	2.07	0.84	-97.8

We have concentrated our discussion on three of the most significant surfaces of the hematite mineral, namely the $\{0001\}$, $\{01\bar{1}2\}$ and $\{10\bar{1}1\}$ surfaces. These three surfaces are important in the experimentally morphology.

The dry {0001} surface of hematite is particularly dominant, as reported in previous studies (e.g. Mackrodt, 1992; Coustet & Jupille, 1994; Godin & LaFemina, 1994; Manassidis & Gillan, 1994; Nygren *et al*., 1997; Parker *et al*., 1999. Cutting the hematite {0001} plane offers two possible surface terminations, which are labelled according to their species - {0001}Fe for the iron-terminated plane which is a non-dipolar surface and {0001}Ox for the oxygen-terminated dipolar plane . The Fe-terminated {0001} surface is the natural plane of hematite and has been studied by a number of researchers (Wasserman *et al*., 1997;Wasserman *et al*., 1999; Parker *et al*., 1999; Rustad *et al*., 1999; Jones *et al*., 2000; Lado-Touriño & Tsobnang, 2000; de Leeuw & Cooper, 2007). **Table 4.1** shows that the Fe-termination has a lower surface energy of 1.78 Jm^{-2} than the oxygen-terminated and all other surfaces of hematite considered here. This surface shown in (**Figure 4.1**(**a**)) is flat and has the smallest unit cell area of all the surfaces considered. Because of the small surface area there is only one surface iron atom, which is equally bonded to three neighbouring oxygen atoms and accessible to adsorbing species such water molecules.

The calculated interatomic distances are compared with experiment in **Table 4.2**. The surface Fe-O bond length perpendicular to the surface plane is 1.80 Å, shorter than the normal bond length in the bulk (1.940 Å), and the Fe-O bond distances vary from 1.80 Å to 2.14 Å depending on whether the anions are in four- or six-fold coordination. The short Fe-Fe distance is 2.89 Å and the bond from the top oxygen atom to the top Fe located to the surface is 1.94 Å, while the long Fe-Fe distance is 3.79 Å and the O-O has decreased from 2.92 Å in the bulk to 2.88 Å in the surface. These results have been compared with experimental work and any

slight difference may be due to the overestimation of the relaxation in the computational model.

The oxygen-termination is the second termination of the {0001} plane, which is dipolar. In order to remove the dipole of this plane, oxygen vacancies are created in the oxygen-terminated surface where half of the oxygen ions are moved to the bottom of the unit cell as described in **Chapter 2**. As a result, the {0001}Ox surface is not flat, as displayed in **Figure 4.1**(**b**) and has the largest surface energy of all the surfaces considered (2.63 Jm^{-2}) where, some of the oxygen surface ions are two-coordinated and accessible to adsorbing species, while the cations (Fe^{+3}) in the second layer of the surface are three- to five-coordinated .

Table 4.2: Selected interatomic distances for the geometry optimised {0001} Fe surface of the hematite structure (Å), compared with experimental data.

	Fe-O nearest	**Fe-Fe inplane**	**Fe-Fe short**	**Fe-Fe long**
Our Calculation	1.94	2.96	2.89	3.79
Experimental *	1.94	2.97	2.90	3.98

*** Data from Finger and Hazen (1980)**

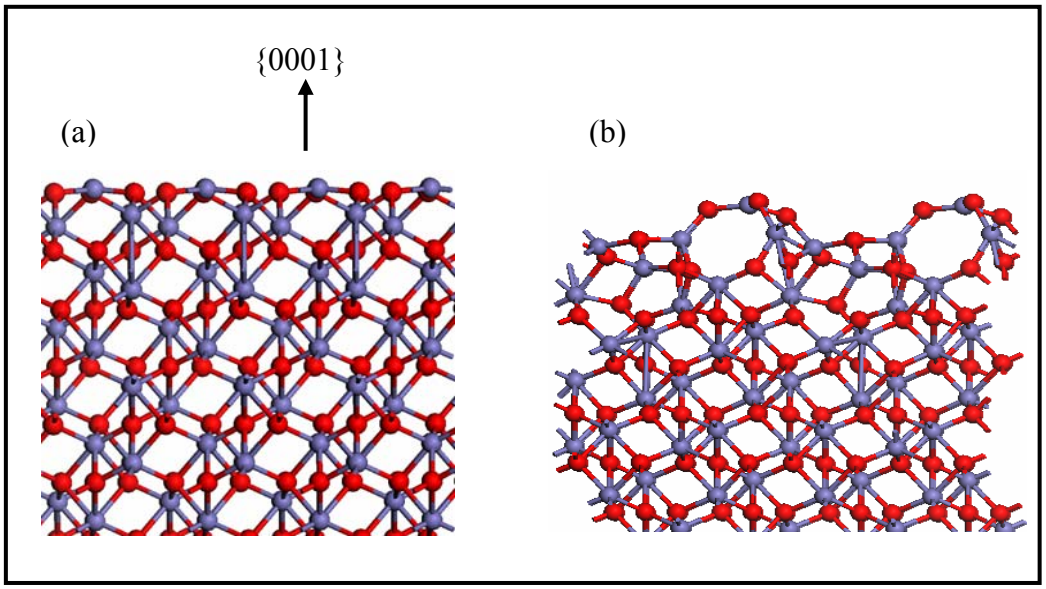

Figure 4.1: Geometry-optimised dehydrated hematite {0001} surface. (a) Fe- and termination (b) Ox- termination. Key: (Iron = blue and Oxygen = red).

The other important dehydrated hematite surface is the $\{01\bar{1}2\}$ surface, which has three possible terminations, all of them a mixture of iron and oxygen ions, and labelled $\{01\bar{1}2\}a$, $\{01\bar{1}2\}b$ and $\{01\bar{1}2\}c$ as listed in **Table 4.1**, de Leeuw and Cooper (2007) have discussed only one termination $\{01\bar{1}2\}a$, which is the most stable termination .This termination is consistently calculated to be more stable, whether the surface is dehydrated or after it is hydroxylated.

The $\{01\bar{1}2\}a$ surface is more stable than the other two terminations for two reasons. Firstly it is a well ordered layered structure as displayed in **Figure 4.2**(**a**); with an interlayer distance of approximately 2.70 Å between the top oxygen ion in the one layer and the layer beneath. The top Fe-O bond length has slightly increased from 1.94 Å, in the bulk to 1.96 Å in the surface; the long Fe-Fe

distance is 3.59 Å in the same plane, whilst the short Fe-Fe distance is 2.84 Å. Secondly, the surface cations are in five- or six-fold coordination, whereas the iron ions are in six-fold coordination in the bulk. Also the surface anions are in three- or four-coordination at the surface.

The $\{01\bar{1}2\}c$ surface is the least stable termination, with a surface energy of γ=2.75Jm^{-2}, compared to the other two terminations. It has a non-uniform low-density structure, as shown in **Figure 4.2**(**b**), with the surface iron ions in four- and five- fold coordination. As mentioned before, the oxidation state of iron is +3 in our simulations, but Henderson *et al*. (1998) and Wang and Rusted (2006) discussed the presence of ferrous ions on these surfaces. In our simulations we cannot deduce the presence of Fe^{2+} ions on the surface, but the coordination found would be compatible with their presence.

The other important termination of the $\{01\bar{1}2\}$ surface is the termination labelled as $\{01\bar{1}2\}b$ and reported in **Table 4.1**, which is the next most stable termination after $\{01\bar{1}2\}a$. **Figure 4.2**(**c**) shows that there are three iron surface ions which are three-coordinated and there are also three-coordinated oxygen ions in the uppermost layer. This surface only has half a layer of oxygen ions in the top layer, with a full layer of Fe ions underneath. A study by Henderson *et al*. (1998) used low energy election diffraction (LEED) under ultra-high vacuum (UHV) conditions to examine this surface; the results revealed an alternative (1x2) surface reconstruction, with a higher surface concentration of cation sites than the (1x1) surface. To conclude, the main difference between the three terminations of

the $\{01\bar{1}2\}$ surface, as displayed in the **Figure 4.2** (**a**), (**b**) and (**c**) is that the $\{01\bar{1}2\}a$ is a more ordered structure with all layers intact compared to $\{01\bar{1}2\}b$ and $\{01\bar{1}2\}c$ surfaces, which are out through the layers and are not planar which that affects the stability of the $\{01\bar{1}2\}b$ and $\{01\bar{1}2\}c$ terminations of this surface.

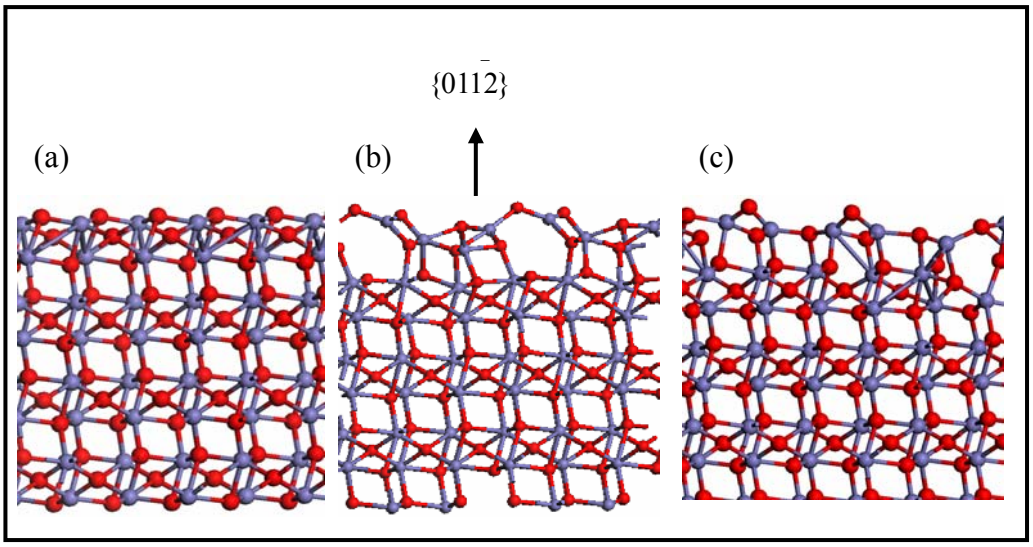

Figure 4.2: Geometry-optimised dehydrated hematite $\{01\bar{1}2\}$ surface. (a) the most stable termination $\{01\bar{1}2\}$a plane, (b) least stable termination $\{01\bar{1}2\}$c and (c) the second most stable termination $\{01\bar{1}2\}$b . Key: (Iron = blue and Oxygen = red).

In addition to the $\{0001\}$ and $\{01\bar{1}2\}$ surfaces, the $\{10\bar{1}1\}$ surface is another important surface, and de Leeuw and Cooper (2007) have described one termination of the $\{10\bar{1}1\}$ surface with a surface energy of 2.34 Jm^{-2}. Here we considered all possible terminations of the $\{10\bar{1}1\}$ surface, labelled as $\{10\bar{1}1\}a$, $\{10\bar{1}1\}b$ and $\{10\bar{1}1\}c$. In this work the $\{10\bar{1}1\}a$ surface is the most stable termination, with a surface energy of 2.34 Jm^{-2} which was the surface presented by de Leeuw

and Cooper (2007). In this surface there are six oxygen ions on the surface , three of which are positioned slightly upwards and the Fe-O bond length decreases from 1.939Å to a variation btween 1.83-1.80 Å after relaxation , as displayed in **Figure 4.3** (**a**) and (**b**). After optimisation of the structure the Fe-O bond length in the second layer increased to bond lengths between 1.90-2.05 Å due to the inter-layer distances in the surface. While the cations on this surface show four-coordination, the anions are in two- to four-fold coordination.

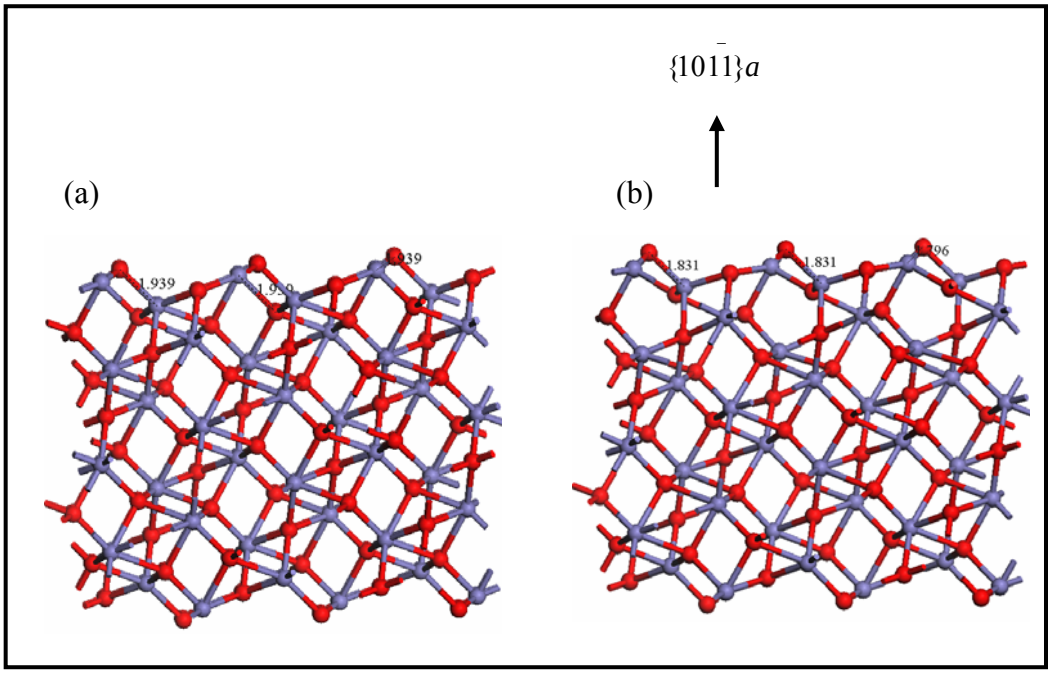

Figure 4.3: Geometry-optimised structure of the most stable termination {10$\bar{1}$1}a of dehydrated hematite {10$\bar{1}$1} surface. (a) before relaxation and (b) after relaxation. Key: (Iron = blue and Oxygen = red).

Our simulation showed there are two other possible terminations ,where the {10$\bar{1}$1}*b* surface has one Fe atom on the surface per simulation cell, while the {10$\bar{1}$1}*c* plane consists of two Fe atoms on the surface. The surface structures of both {10$\bar{1}$1}*b* and {10$\bar{1}$1}*c* planes are irregular, as shown in **Figure 4.4 and 4.5**. In the termination , which is more stable than the {10$\bar{1}$1}*c* termination by 0.11 Jm^{-2}, the iron atom on the surface is in four-fold coordination, compared to Fe atoms in the bulk which are three- to six-coordinated, while the anions are two-, three- and four-coordinated. When the surface structure of {10$\bar{1}$1}*b* is optimised, rearrangement occurs of the positions of the oxygen atoms on the surface which

before relaxation are three-coordinated. After relaxation they become two-coordinated and stand-out from the surface compared to other surface atoms (see **Figure 4.4** (**a**) and (**b**)). Because of the rearrangement of the oxygen position on the surface the Fe-O bond lengths decrease from 2.11 Å to 1.81 Å and 1.82 Å.

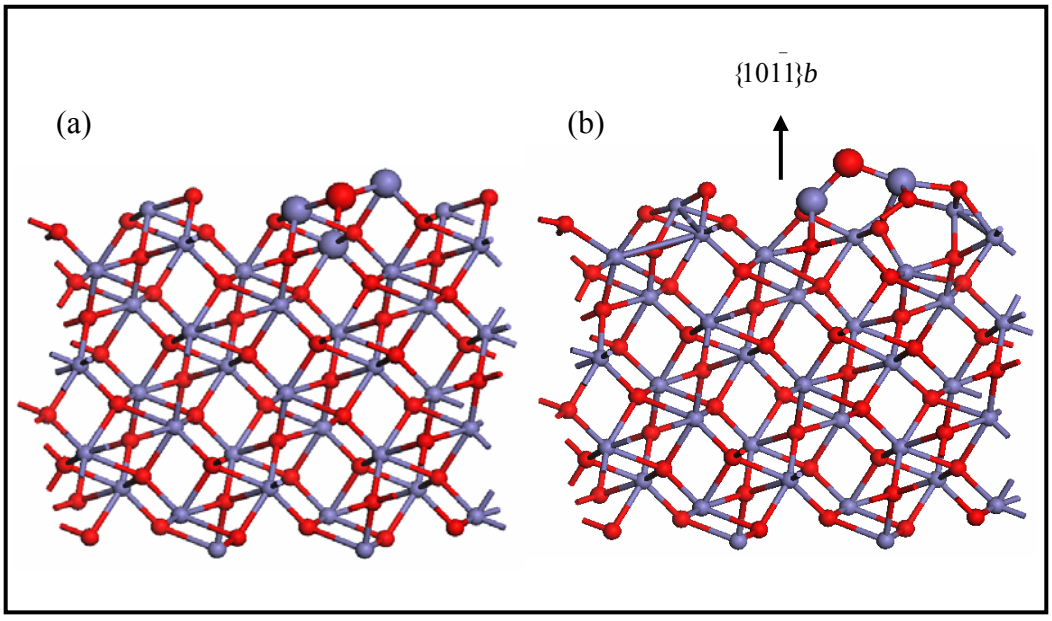

Figure 4.4: Geometry-optimised structure of the most stable termination {10$\bar{1}$1}b of dehydrated hematite {10$\bar{1}$1} surface. (a) before relaxation and (b) after relaxation. Key: (Iron = blue and Oxygen = red). The big red ball is the three-coordinated oxygen bonded to three big blue iron ions and after relaxation it becomes two-coordinated. Key: (Iron = blue and Oxygen = red).

Rearrangement also occurs in the {10$\bar{1}$1}*c* termination. Before relaxation the Fe are three-coordinated, but after relaxation they are four-coordinated when the oxygen atom on the surface moves to bridge between the two iron atoms (**Figure 4.5**) which pushes the iron slightly downwards in relation to other surface atoms. The

rearrangement of the iron and oxygen positions on the surface result in the Fe-O bond lengths decreasing from 1.94 Å and 2.11 Å to 1.89 Å and 1.88 Å, respectively, and the other Fe-O increase from 1.94 Å to 2.09 Å with a new Fe-O bond length of 1.76 Å.

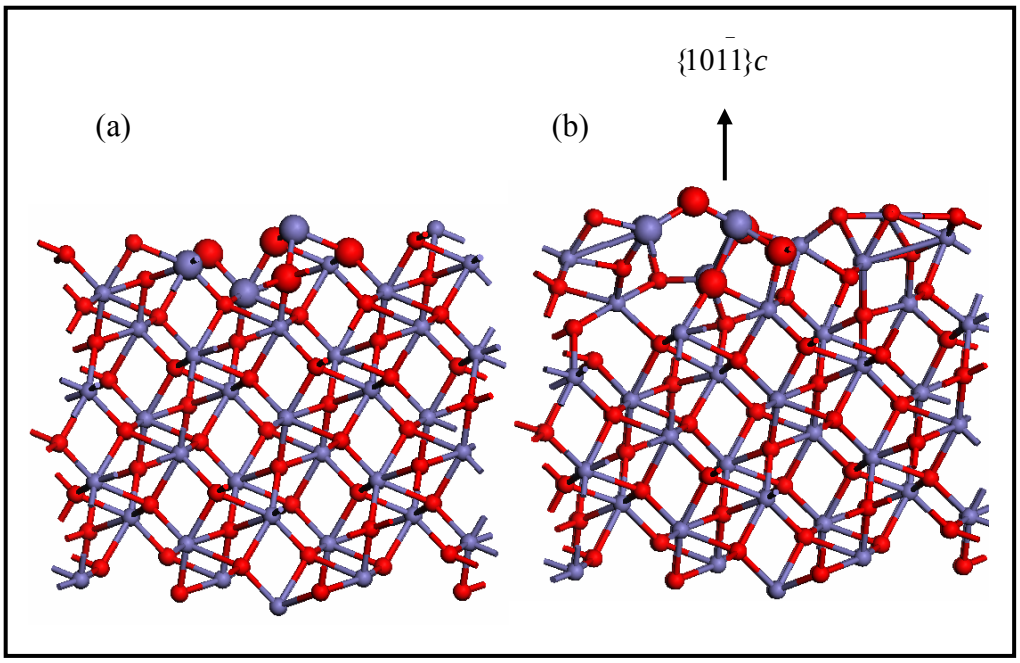

Figure 4.5: Geometry-optimised structure of the less stable termination {10$\bar{1}$1}c of dehydrated hematite {10$\bar{1}$1} surface. (a) before relaxation and (b) after relaxation. The big blue ball is the three –coordinated oxygen bonded to three big red ball oxygen ions and after relaxation it becomes four-coordinated. Key: (Iron = blue and Oxygen = red).

4.3.2 Hydroxylated Surfaces

We next investigated the effect of adsorption of dissociated water molecules on the stability of the hematite surfaces through evaluation of the surface energies and the relaxed hydroxylated surface structures. In this thesis, our surfaces were fully hydroxylated, which we could expect to occur in the natural environment. All the surface Fe ions are bonded to hydroxy groups and all the surface oxygen ions are protonated by the hydrogen ions from the dissociated water molecules.

The calculated surface energies, listed in **Table 4.1** show that all the hematite surfaces have become more stable after hydroxylation, whereas the {0001}Ox surface is now more stable than the {0001}Fe surface and indeed all other surfaces, in agreement with other classical calculations (de Leeuw and Cooper, 2007).

Upon hydroxylation, both iron- and oxygen- terminations of the {0001} surface are stabilised, with surface energies of 1.21 Jm^{-2} and 0.51 Jm^{-2} respectively, indicating that the oxygen-terminated plane would be expected to occur under aqueous conditions. If the surface is dehydrated, then the Fe-termination should occur, in agreement with Chambers and Yi (1999) who used molecular beam epitaxy and found only the Fe-termination. Eggleston *et al*. (2003) studied the structure of the hematite {0001} surface in aqueous media, using scanning tunnelling microscopy and resonant tunnelling calculations to show that under aqueous condition the O-termination can be present (Eggleston *et al*., 2003). The

hydroxylated {0001} Fe and {0001}Ox surfaces . After geometry optimisation are shown in **Figures 4.6** (**a**) and (**b**) respectively.

Upon hydroxylation of the Fe-termination, the surface cations are in four-fold coordination, compared to six-fold coordination in the bulk, and the surface anions are in four-coordination as in the bulk, which makes the surface more stable than the dehydrated surface. In contrast, in the oxygen-terminated surface the sub-surface iron atoms are now in six-fold coordination, as in the bulk, and the oxygen vacancies in the dry reconstructed dipolar plane are filled by the OH groups, leading to a smooth proton-terminated plane (**Figure 4.6**(**b**)). After hydroxylation, the Fe-O bond length increases from 1.80 Å to 2.03 Å, resulting in the conversion of three-coordinated oxygen and iron surface positions to four-coordination, although the Fe-O bond on the surface is still shorter than the Fe-O bond length in the bulk, whereas the Fe-O bond length to the hydroxy group is 1.70 Å.

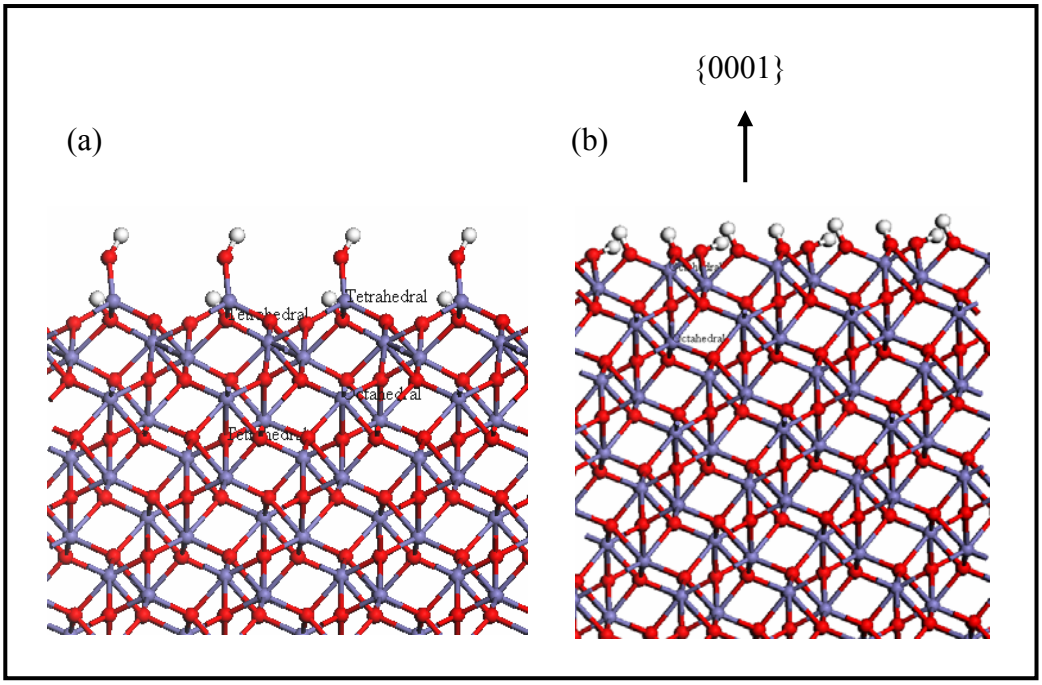

Figure 4.6: Geometry-optimised structures of hydroxylated hematite {0001} surface. (a) the partially hydroxylated iron-terminated surface and (b) the fully-hydroxylated oxygen-terminated surface. Key: (Iron = blue, Oxygen = red and Hydrogen=white).

4.3.3 Hydration Energies

The energies for the dissociative adsorption of water on each hematite surface have been calculated via the Born-Haber cycles, discussed in section 4.2.2 of this chapter, and the values have been listed in **Table 4.1**, which shows that all are exothermic reactions. The tendency to adsorb water could be attributed to the under-coordinated sites on each surface and the regular hydrogen-bonded structures of the water layers.

4.3.4 Morphologies

The external shape of the crystal is called the habit or morphology of the crystal(Schwertmann & Cornell, 2003) and the observed morphology of a crystal is usually called the growth morphology or equilibrium morphology. In fact, the equilibrium morphology depends on a number of factors. (i) The arrangement of ions in the crystal that determine the symmetry of the unit cell. (ii) pH and (iii) supersaturation and (iiii) ionic strength. The GDIS 0.90 program is used to generate the equilibrium morphologies of the crystals in this work.

There are a number of methods used for morphology predictions .One method is based on attachment energies (E_{att}) which are defined as the energies released per mole when a new layer is deposited on a crystal face and they represent the strength of binding of a complete layer of crystal to the surface; thus a surface with a small absolute attachment energy presents a very stable surface structure(Hartman & Chan, 1993). The attachment energy is inversely proportional to its morphological importance, thus a low attachment energy of a surface suggests it will be dominant in the morphology.

In this work, the relative growth rates of the possible faces of each crystal structure and the resulting equilibrium morphology have been determined using the surface energy and the lattice vector of the unit cell, according to Wulff's theorem (1901) and Gibbs (1928), where Gibbs suggested that the equilibrium

morphology of the crystal under thermodynamic control should possess minimal total surface energy for a given volume

$$\int \gamma \, dA = \min \qquad \textbf{(4.7)}$$

where γ is the surface energy and *A* is the surface area. Therefore, the shape of the crystal, according to the Wulff theorem is determined by γi/*hi*= constant, where γ_i is the surface free energy of a crystal face i and h_i is the distance from the centre to the face i. Thus, when a surface has a high surface energy, h_i will be large and it may therefore not be expressed in the morphology, because only surfaces with low surface energy, and small h_i are expected to occur in the calculated equilibrium morphology. Surfaces with high surface energies have a large growth rate and may "grow out of the morphology".

The calculated morphologies based on the dehydrated and hydroxylated surfaces of hematite are shown in **Figure 4.8** (**b**) and (**c**). The equilibrium morphology of the dehydrated hematite crystal shows the dominance of the $\{0001\}$, and the $\{01\bar{1}2\}$ surfaces because these two planes have the lowest surface energies as reported in **Table 4.1**. **Figure 4.8**(**b**) shows a number of additional stable surfaces, e.g. the $\{11\bar{2}1\}$. Although elongated the calculated hydroxylated morphology agrees very well with the experimental morphology, expressing $\{0001\}$, $\{10\bar{1}1\}$ and $\{11\bar{2}0\}$ faces although the $\{0001\}$ face is not as stable as in the experimental morphology show here. However, experimental morphologies can be due to other kinetic factors, as well as the thermodynamics considered here.

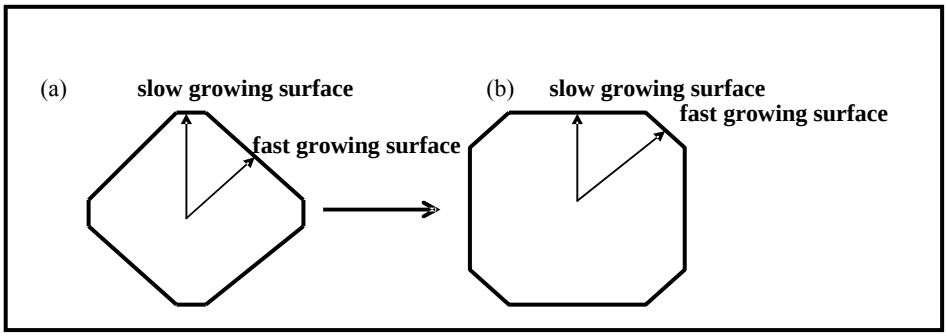

Figure 4.7: Schematic representation of the equilibrium morphology resulting structure from faces with different surface energies where (a) the initially large, fast growing surface in (b) has become small compared to the slow growing surface.

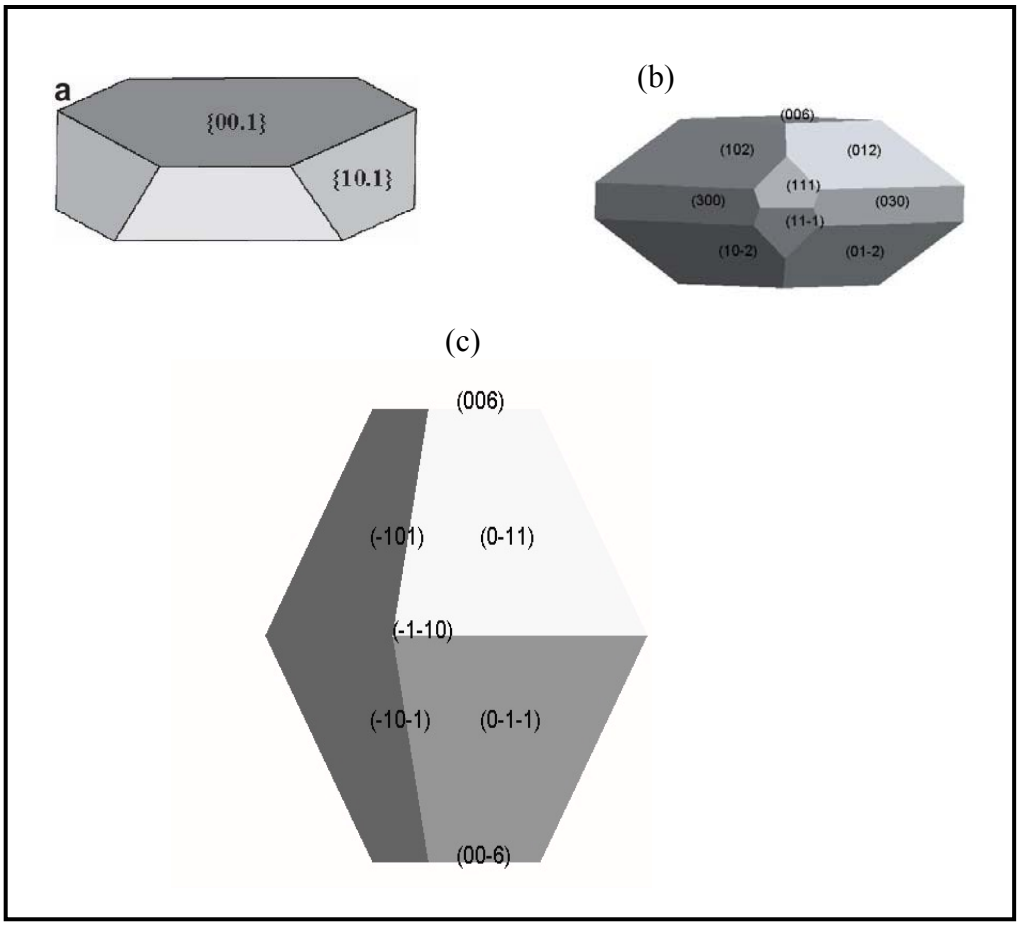

Figure 4.8: Experimental (a), calculated dehydrated (b) and hydroxylated(c) equilibrium morphologies of hematite.

4.4 Maghemite (γ-Fe_2O_3)

We next investigated the structures and energies of the dehydrated and hydroxylated maghemite surfaces where we have created a number of surfaces with low Miller indices: {001}, {010} ≡ {100}, {110}, {103} ≡ {013} and {113}. The {103} and {113} surfaces of the triple unit cell used in our simulations (**Chapter 3**) would be the {101} and {111} surfaces of a single cell. For each surface there are two or more terminations possible, which all contain both iron and oxygen atoms in the surface.

4.4.1 Dehydrated Surfaces

Table 4.3: Calculated surface energies (Jm^{-2}) and hydration energies ($kJmol^{-1}$) of dehydrated and hydroxylated maghemite surfaces.

Surface	Termination	γ_{pure}	$\gamma_{dissociative}$	$E_{dissociative}$
{001}a	Fe/Ox	1.36	1.07	-20.4
{001}b	Fe/Ox	1.42	0.83	-41.5
{001}c	Fe/Ox	1.62	0.57	-88.7
{001}d	Fe/Ox	1.79	1.30	-28.4
{010}a	Fe/Ox	1.32	0.94	-26.9
{010}b	Fe/Ox	1.44	1.29	-10.0
{110}a	Fe/Ox	1.71	1.02	-49.3
{110}b	Fe/Ox	1.83	1.14	-51.3
{113}a	Fe/Ox	1.75	1.54	-10.5
{113}b	Fe/Ox	2.00	1.59	-23.3
{103}a	Fe/Ox	1.75	1.09	-30.9
{103}b	Fe/Ox	1.76	1.11	-21.0
{103}c	Fe/Ox	1.83	1.27	-29.9
{103}d	Fe/Ox	1.85	1.30	-20.5
{103}e	Fe/Ox	1.86	1.33	-47.9
{103}f	Fe/Ox	1.88	1.43	-34.5
{103}g	Fe/Ox	1.98	1.50	-43.6

We have concentrated our discussion on two of the most significant surfaces of the maghemite mineral, namely the {010} and {001} surfaces, which are the top most stable surfaces (**Table 4.3**). The calculated surface energies, listed in **Table 4.3**, indicate that the {010}a surface is energetically more stable than all other dehydrated maghemite surfaces. Cutting in the {010} direction offers two possible terminations, labelled as {010}a and {010}b as reported in **Table 4.3**. Both terminations have similar surface energies, and are therefore almost equally likely to occur. The {010}a surface with surface energy of 1.32 Jm^{-2} is displayed in **Figure 4.9**(**b**). Before relaxation, the {010}a surface has three Fe ions in the topmost layer in two-fold coordination, whereas the oxygen ions are in three- and four-coordination. Upon optimisation of the surface, rearrangement occurs of the undercoordinated Fe ions, which after relaxation are accommodated in four-fold coordination further into the surface, whereas after relaxation all oxygen ions are now three-coordinated. The high coordination of the surface ions probably contributes to the stability of the surface. In the second layer, the Fe-O bond length increases to vary from 1.94 Å to 1.98 Å resulting in a less dense surface region.

The only difference between the two terminations of the {010} surface, which increases the surface energy of the {010}b plane to 1.44 Jm^{-2} (**Table 4.3**) is the coordinated of one Fe ion on the surface which after relaxation is in three-fold coordination instead of four-fold coordination, whereas the surface oxygen ions are in two- and three-fold coordination compared with three-coordination as has been found in the {010}a plane. Also the Fe-O bond length in the second layer increases for the four-coordinated Fe, from 1.90 Å to 1.95 Å (**see Figure 4.11**(**b**)).

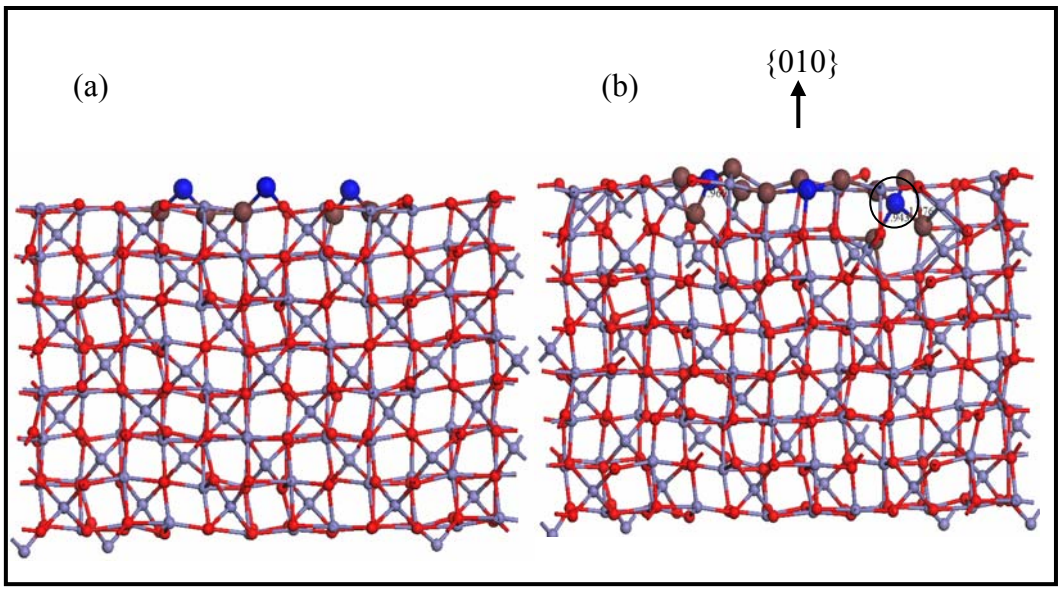

Figure 4.9: Geometry-optimised structure of the most stable termination {010}a of the dehydrated maghemite {010} surface. (a) before relaxation and (b) after relaxation. Key: (Iron =blue and Oxygen = red).The bright blue balls are the two-coordinated Fe ions, bonded to two brown oxygen ions, which after relaxation become four-coordinated.

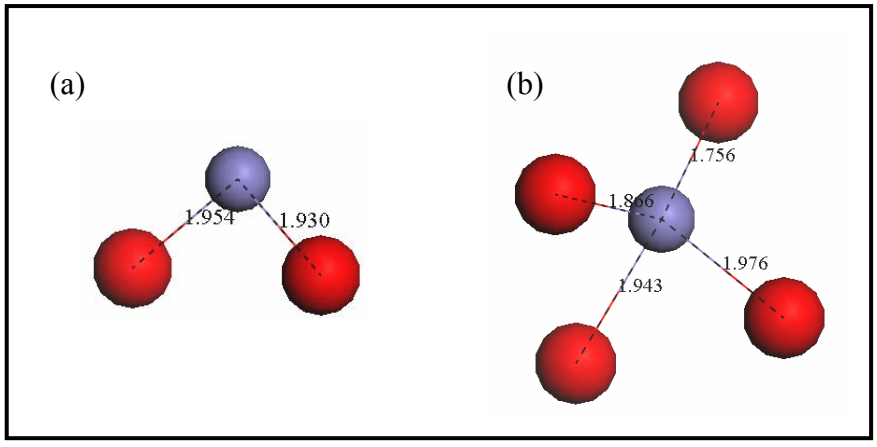

Figure 4.10: The different Fe-O bonds distances (Å) observed in the {010}a surface (a) before relaxation and (b) after relaxation.

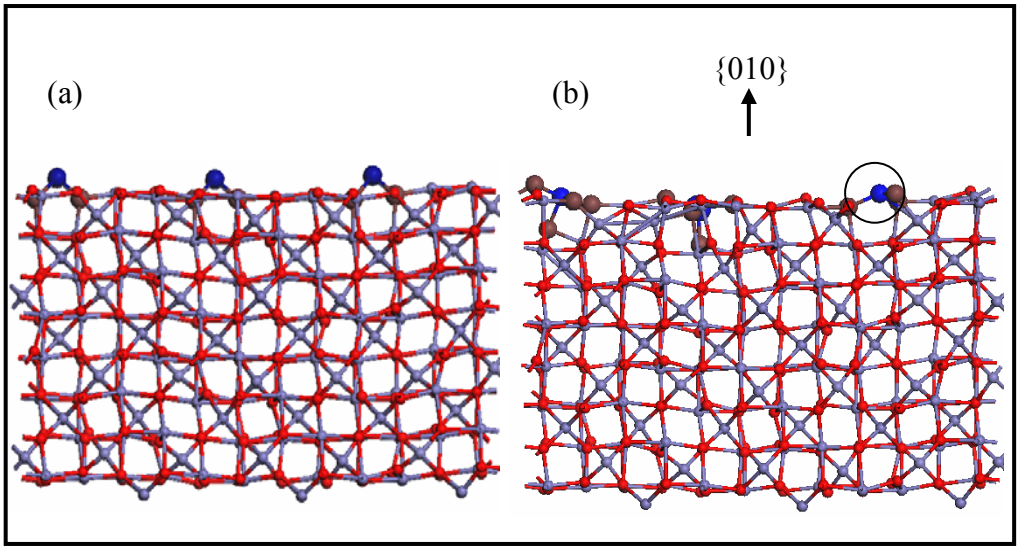

Figure 4.11: Geometry-optimised structure of the less stable {010}b termination of the dehydrated maghemite {010} surface. (a) before relaxation and (b) after relaxation, Fe(circled) becomes three-coordinated. Key: (Iron =blue and Oxygen = red).

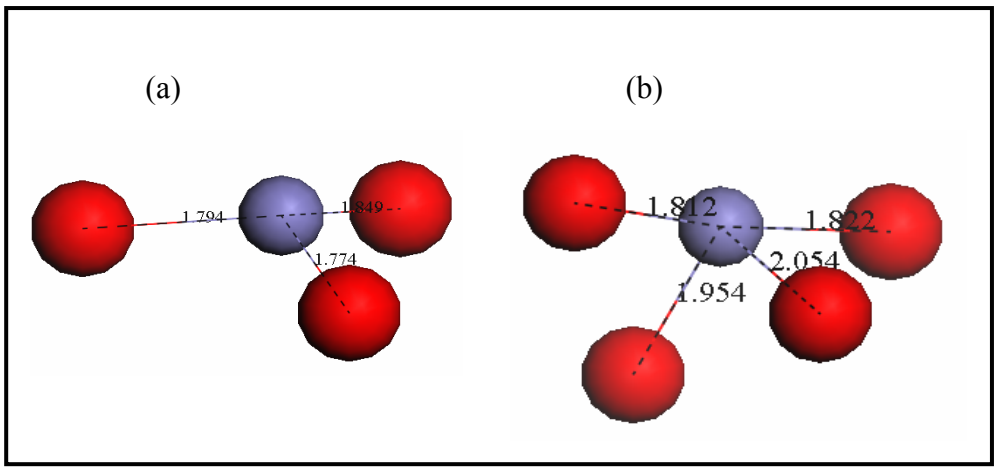

Figure 4.12: The different Fe-O bond distances (Å) observed in the {010}b surface. (a) three-coordinated Fe and b) four-coordinated Fe.

The other important dehydrated maghemite surface is the {001} surface, which has four possible terminations, labelled {001}a,{001}b,{001}c and {001}d as listed in **Table 4.3**. The calculated surface energies (**Table 4.3**) show that the {001}a is the next most stable surface with surface energy of 1.36 Jm^{-2} after the {010}a surface.

The {001}a surface is non-polar, with a well ordered structure, and is more stable than the other three terminations. Before optimisation the surface is flat with four- and five-fold coordinated cations, whereas the surface anions are in three-fold coordination. After optimisation, an oxygen atom has moved out of the surface, and the surface anions are in two- and three-fold coordination, while the Fe in the layer below are in five- and six-fold coordination. The relaxation of the oxygen ion out of the surface causes the Fe-O bond distance to increase from 2.08 Å to 3.23 Å hence breaking the bond. This low coordinated oxygen ion on the surface could be reactive towards impurities, such as water, pollutants or catalytic reactants.

The {001}b surface is the second-most stable termination of the{001}surface. The surface structure is irregular, where the cations on the surface before optimisation are in two- or five-fold coordination, whereas in the layer below, the Fe atoms are in four-, five and six-fold coordination. The surface anions are two-, three- and four-coordinated. Upon relaxation, the bond between the oxygen atom on the surface and the iron atom in the next layer is broken and it now forms a bridge to the iron atom on the top of the surface, which also bonds to another oxygen below the surface as can seen in **Figure 4.13(d)**. The Fe-O bond distance

between the oxygen on the surface and the iron in the layer below increases from 2.08 Å to 3.43 Å, resulting in the conversion of a six-coordinated iron atom to five-coordination. The iron atom in the surface is in four-fold coordination compared to two-coordination before relaxation. The overall result of this rearrangement moves the oxygen slightly upwards and at the same time the iron atom moves slightly downwards.

The other terminations of the {001} surface are the {001}c, where there is one oxygen atom on the surface, and the {001}d which consists of two oxygen atoms on the surface. The surface structures of both {001}c and {001}d surfaces are irregular as shown in **Figures 4.14**(**b**) and (**d**) respectively. After relaxation of the {001}c surface, rearrangement occurs of the positions of oxygen and iron atoms on the surface, which decreases the Fe-O bond distances to 1.90 Å and 1.91 Å.

On the {001}d plane there are two singly-coordinated oxygen atoms on the top of the surface ,whereas the other eight oxygen ions are in three- or four-fold coordination. These oxygen atoms with dangling bonds move down to form extra Fe-O bonds, varying in length from 1.98 Å to 2.47 Å. After relaxation, all oxygen ions on the surface are in three- and four-fold coordination.

To conclude, the simulations of the different terminations of the {001} surface have identified that the {001}a is the most stable plane, due to the combination of relative high coordination numbers of the surface species and a regular surface structure.

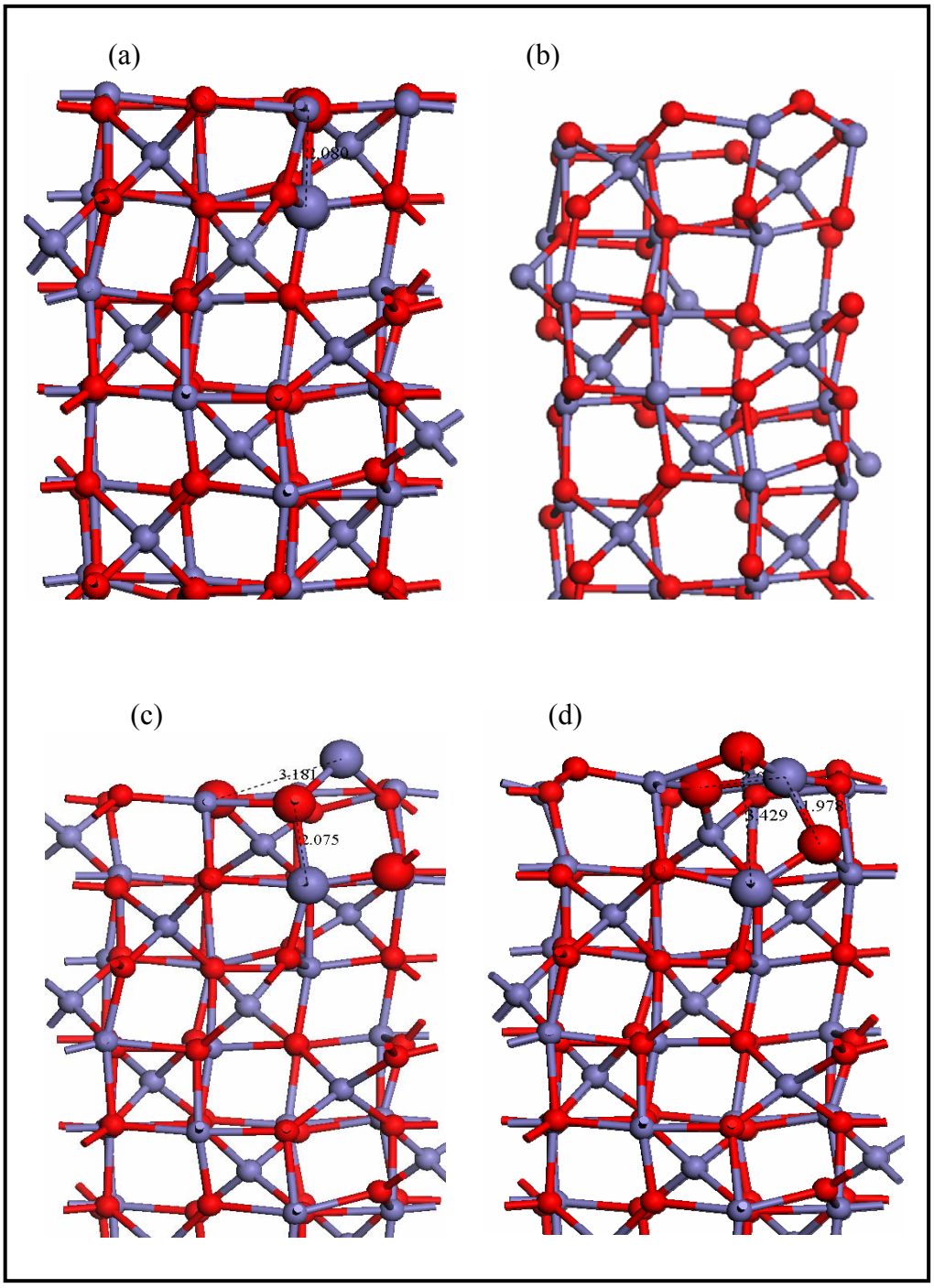

Figure 4.13: surface structures of the dehydrated maghemite {001} surface. (a) and (b) before and after relaxation of the {001}a surface, (c) and (d) before and after relaxation of the {001}b surface, shown distances in (Å). Key: (Iron =blue and Oxygen = red).

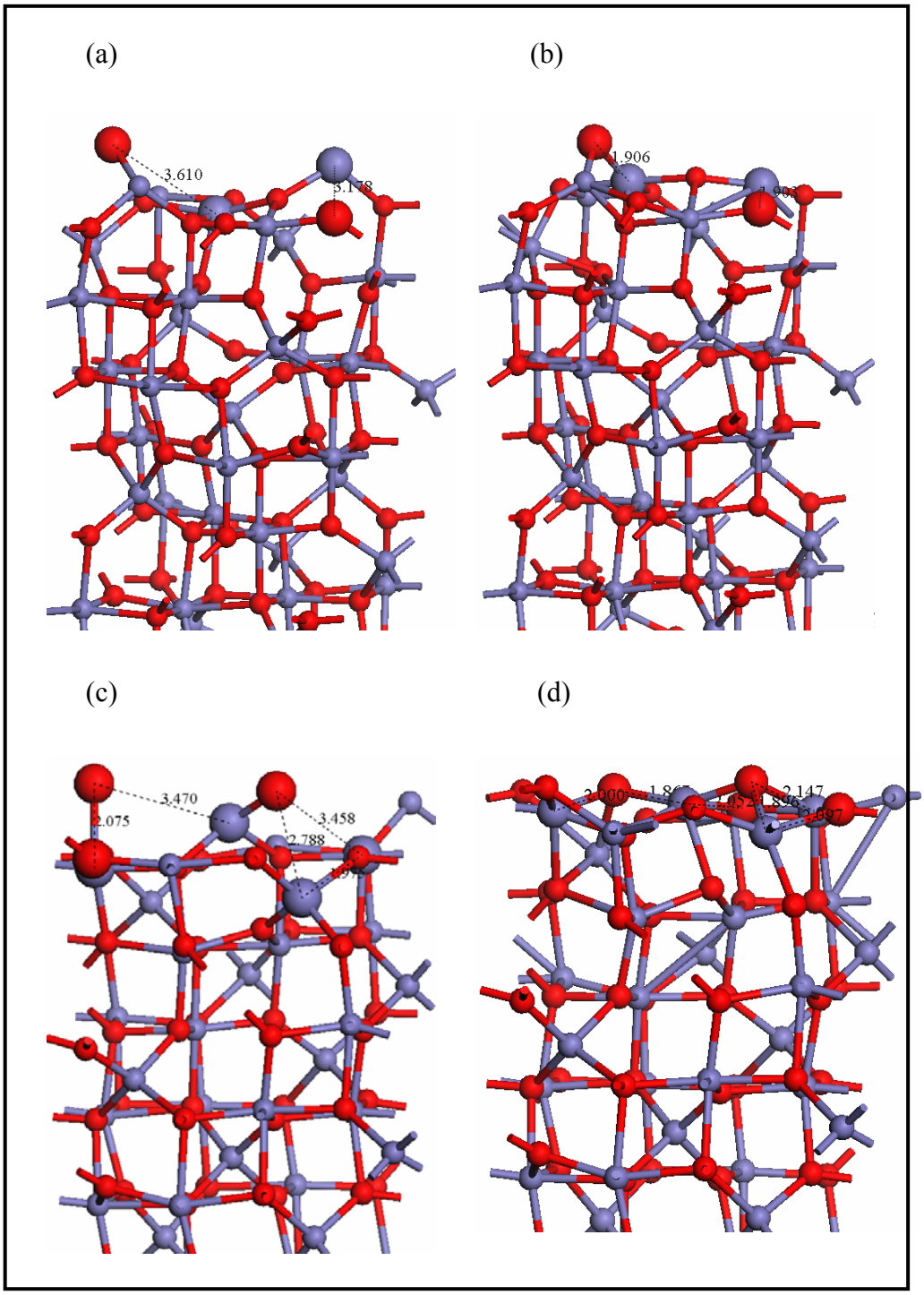

Figure 4.14: surface structures of the dehydrated maghemite {001} surface. (a) and (b) before and after relaxation of the {001}c surface, (c) and (d) before and after relaxation of the {001}d surface, shown distances in (Å). Key: (Iron =blue and Oxygen = red).

4.4.2 Hydroxylated Surfaces

As we mentioned before, the effect of hydroxylation of the surfaces has been investigated for both hematite (α-Fe_2O_3) and maghemite (γ-Fe_2O_3) iron oxides. Again, we have hydrated all the pure surfaces of maghemite considered here.

Upon hydroxylation of all the cations and anions of the surfaces, the surface energies were recalculated as listed in **Table 4.3**. It is evident that all the surfaces became more stable with various alterations in the order of stabilities of the different terminations of the same surface. For example, the {001}b and {001}c terminations have become the most stable surfaces with surface energies of 0.83 Jm^{-2} and 0.57 Jm^{-2} , respectively. The hydroxylated {001}c surface is clearly more stable than the other {001}surfaces indicating that this {001}c plane would be expected to occur under aqueous condition.

The surface cations on the hydroxylated {001}c surface are in five- and six-fold coordination compared to three-, four- and five- coordination before hydroxylation, while the surface anions are two-, three- or four- coordinated, compared to two- or three-fold coordination, before hydroxylation. After relaxation, (**Figure 4.15**(**a**)), the Fe-O bond length is closer to the bulk values, while the Fe-OH bond lengths vary between 1.76 Å - 2.24 Å and the hydrogen-bonding interaction distances range from 1.87 Å to 2.18 Å.

The {001}b surface also favours hydroxylation ,with reduction of the surface energy from 1.42 Jm^{-2} to 0.83 Jm^{-2} because the Fe initially in four- and five-fold

coordination now are in five- and six-fold coordination after hydroxylation. This surface has also been stabilised by hydrogen-bonding interactions between the hydrogen and oxygen of hydroxy groups on the surface, where the Fe-OH bonds are shorter than the Fe-OH on the {001}c plane, ranging from 1.86 Å to 2.36 Å. In comparison, the {001}a plane favours hydroxylation to a lower extent, lowering its surface energy only to 1.07 Jm^{-2}, perhaps because this surface was already stable as a dehydrated surface, making it less reactive than other terminations toward adsorbing impurities such as water. Hydrogen-bonding interactions distances range from 1.94 Å to 2.13 Å.

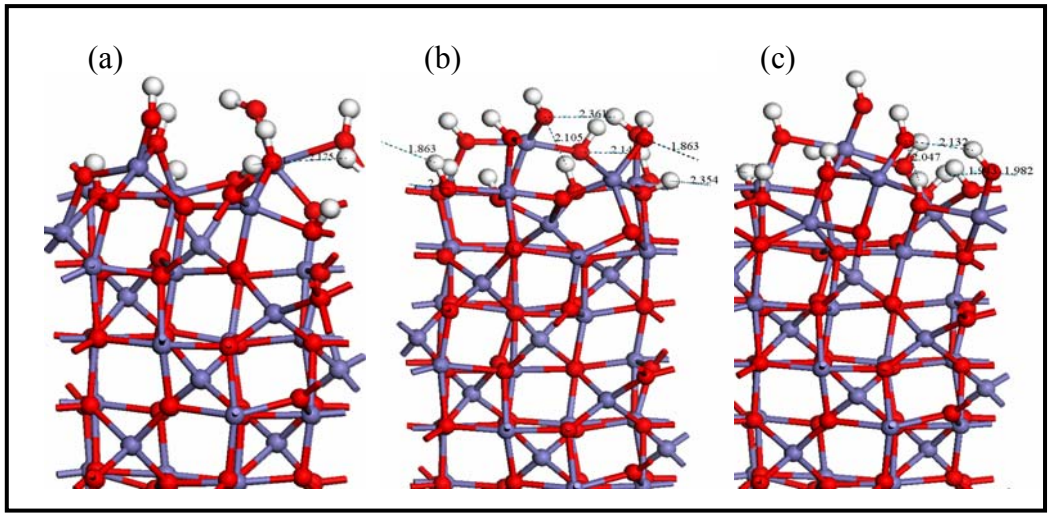

Figure 4.15: Geometry-optimised structures of the three most stable terminations of the hydroxylated maghemite {001} surface. (a){001}c,(b) {001}b and (c) {001}a surfaces, shown distances in (Å). Key: (Iron =blue and Oxygen = red and Hydrogen = white).

Of the {010} terminations, the {010}a surface is still the most stable, now with a surface energy of 0.94Jm^{-2} as compared to the {010}b termination where γ=1.29 Jm^{-2}. On optimisation of the {010}a plane, the surface cations are four-,

five- and six- coordinated. The hydroxy groups do not absorb in a regular pattern resulting in a irregular surface structure. Some of the adsorbed hydroxy groups are close to each other leading to a range of hydrogen-bonded interactions at 1.74 Å to 2.44 Å. The Fe-OH bond lengths vary from 1.73 Å to 2.22 Å, while the bond distance between Fe and oxygen in the layer below have become closer to the bond distances between Fe-O in the bulk, ranging from 1.81 Å to 2.18 Å as displayed in **Figure 4.16**.

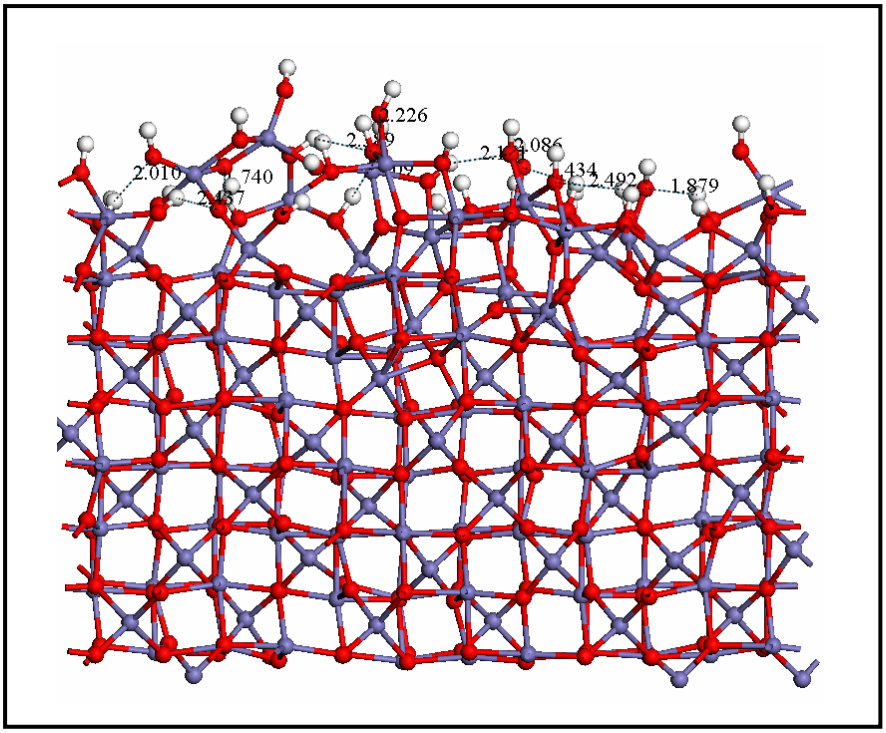

Figure 4.16: Geometry-optimised structure of the more stable {010}a termination of the hydroxylated maghemite {010} surface, shown distances in (Å). Key: (Iron =blue and Oxygen = red and Hydrogen = white).

4.4.3 Hydration Energies

The calculated hydration energies of all the hydroxylated surfaces of maghemite (γ-Fe_2O_3) are listed in **Table 4.3**. Where we see that the hydration energies range from -10.5 $kJmol^{-1}$ on the {113}a surface to -88.7 $kJmol^{-1}$ on the {001}c surface. Hydroxylation of the surfaces is clearly energetically favourable and the stabilities of the surfaces have increased, as indicated by the surface energies of the hydroxylated surfaces which are always less than the surface energies of the unhydrated surfaces.

4.4.4 Morphologies

Maghemite (γ-Fe_2O_3) is usually obtained from another iron oxide material and the habit of the morphology of maghemite may therefore depend on the morphology of the parent material. For example, the dehydration of goethite to hematite, reduction of hematite to magnetite and finally oxidation to maghemite (Berkowitz *et al*., 1985) will give maghemite with the {101} as the long axis. Maghemite can also be obtained from the dehydroxylation of lepidocrocite. Single crystals of maghemite, as used for the magnetic recording, have been obtained from spindle-shaped hematite. (Maeda, 1978; Ozaki & Matijevic, 1985).

The calculated maghemite morphologies based on unhydrated and hydroxylated surfaces are shown in (**Figure 4.17** (**a**) and (**b**)). The equilibrium morphology of the unhydrated crystal shows the dominance of the {001} and {010} surfaces, which are the most stable surfaces of the unhydrated maghemite surfaces with the

lowest surface energies. However, the morphology also expresses the {110},{103} and {113} faces.

The calculated morphology based on the hydroxylated surfaces of maghemite is displayed in **Figure 4.17** (**b**) and is very similar to the morphology based on the unhydrated surfaces, with the dominance of the {001} and {010} surfaces, but now more of the {110} and {103} planes are expressed and the {113} planes have disappeared.

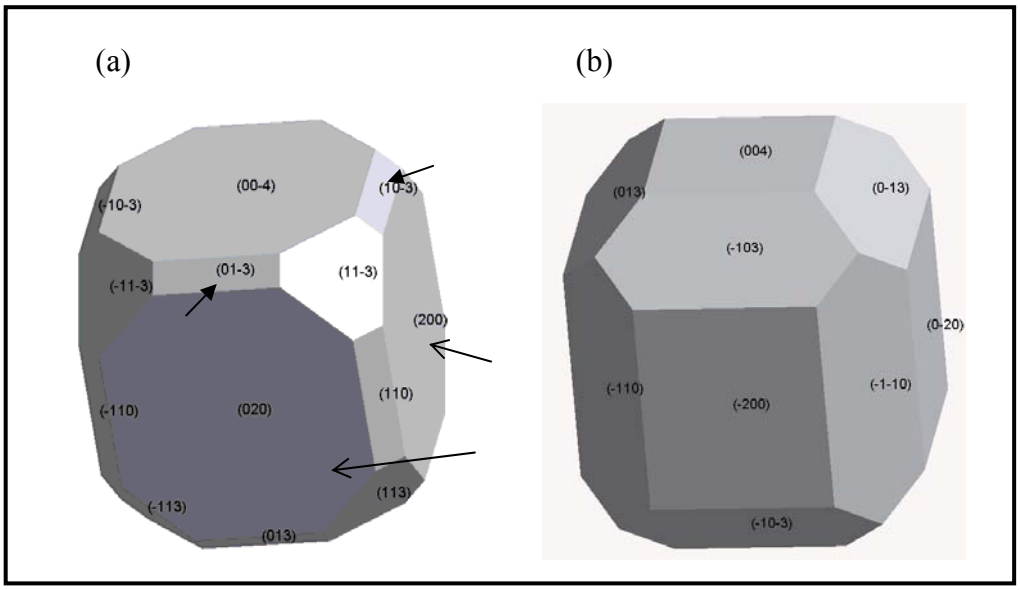

Figure 4.17: Calculated equilibrium morphologies of maghemite. (a) unhydrated and (b) hydroxylated.

4.5 Discussion and Conclusions

In this chapter, the characteristics of a range of low Miller index surfaces of hematite (α-Fe_2O_3) and maghemite (γ-Fe_2O_3) have been investigated, including hydration, adsorption of dissociative water molecules to the surfaces to full monolayer coverage. The equilibrium morphologies of the minerals based on both unhydrated and hydroxylated surface energies have also been calculated. As a result we can make the following observations.

- All surfaces of both hematite and maghemite can be terminated in two or more possible ways, by iron planes, oxygen plans or a mixture.
- When dehydrated, the Fe-terminated {0001} surface of hematite is the most stable plane, whereas the oxygen-terminated {0001} surface is the least stable face of all unhydrated surfaces of hematite. However, after adsorption of dissociative water molecules to the surface the oxygen-terminated {0001} became the most stable face in agreement with previous studies (de Leeuw & Cooper, 2007).
- Upon hydration by dissociative water molecules to the surface all surface energies decreased, and hydroxylation stabilises all surfaces by increasing the surface iron- and oxygen-coordination on the surface to more bulk-like coordination environments.
- The major interaction between the adsorbing water molecules and the surface was through interaction of their oxygen ions with surface iron ions, followed by hydrogen-bonding to surface oxygen ions. Hydrogen-bonded

networks between the hydroxy groups stabilise the hydrated structures further.

- The calculated hydration energies ($E_{dissociative}$) are negative indicating that the hydration process is thermodynamically favourable.
- Finally, the calculated morphologies of both hematite and maghemite, calculated using GDIS version 0.90, shows that the calculated hematite morphology is in reasonable agreement with one experimental morphology and expresses the main surfaces as seen experimentally. No experimental morphology for maghemite is available for comparison.
- However, the structure and the hydration of hematite α-Fe_2O_3 surfaces has been investigated, before by a number of researchers, for example, Becker *et al*. (1996) have studied the electronic structure of the hematite surface using ab-initio methods to interpret experimentally collected STM data, but also to gain insight into atomic level changes in electronic structure that are associated with heterogeneous surface reactions. Their calculations show that the local electronic structure of surfaces can be very different from bulk electronic properties and that conclusion drawn from cluster calculations representing the bulk can be misleading. In addition, this theoretical approach helps to explain the increased reactivity at specific sites on hematite, such as steps and kinks, in terms of the electronic surface structure of this mineral. Bergermayer and Schweiger (2004) have used Density Functional Theory with the generalized gradient approximation to study the oxygen coverage, structure and thermodynamic stability of the {0001} surface of hematite as a function of temperature and oxygen pressure, while the stabilities, structures, electronic, and magnetic

properties of the {0001} surfaces of hematite and iso-structural chromia or eskolaite (Cr_2O_3) have been investigated using ab initio methods by Rohrbach *et al*. (2004). Alvarez- Ramírez *et al*. (2004) have used four different DFT approximation levels, namely, the non-selfconsistent Harris functional, the local spin-density approximation, LSDA, the PW91 or BP meta GGA functional and the hybrid B3LYP method, to study the geometric structure of the {0001} hematite surface and they found that the Harris functional can be used to explore the adequacy of a given model but not to provide an accurate enough structure of the relaxed hematite {0001} surface. Lo *et al*. (2007) have studied the structures of the clean and hydrated hematite α-Fe_2O_3 $\{11\bar{0}2\}$ surface using DFT. They have calculated free energies of the surfaces in chemical equilibrium with water as a function of temperature and oxygen partial pressure, using *ab initio* thermodynamics and they found that the hydroxyl groups lead to large differences in energetic stability and layer relaxations of the oxide substrate. As well as, the effect of the hydroxylation on surface stability for both hematite and maghemite have been studied experimentally by Watanabe and Seto (1988), whereas Eggleston *et al*. (2003) have studied the structure of hematite {0001} surface in aqueous media using scanning tunnelling microscopy and resonant tunnelling calculations to show that under some conditions the Oxygen-termination can be present whereas the other studies find no evidence for an Oxygen-termination. Also the structure and reactivity of the hydrated hematite {0001} surface were investigated via combined theoretical and experimental techniques using DFT and crystal truncation rod diffraction by Trainor *et al*. (2004) and

their results show that the surface is dominated by two hydroxyl moieties: hydroxyls that are singly coordinated and doubly coordinated to Fe.

- In the next chapters we will present our calculations of the adsorption of organic molecules and arsenate at the dehydrated and hydroxylated surfaces, discussed in this chapter.

Chapter 5

Adsorption of Surfactants to Hematite (α-Fe_2O_3) and Maghemite (γ-Fe_2O_3) Surfaces

5.1 Introduction

One of the most interesting applications of iron oxide minerals is their use as adsorbents of organic substances and they, for example, can be employed as sensors owing to their adsorption capacity (Schwertmann and Cornell, 2003). This affinity towards adsorption of organics is the focus of this chapter where we have studied the iron oxides' interaction with model organic pollutants, which are found in the soil and groundwater.

In **Chapter 4** we have shown that our simulation techniques can model the interaction of dissociative water molecules with surfaces of both hematite (α-Fe_2O_3) and maghemite (γ-Fe_2O_3) iron oxides. Here we extend this work to study the strength of interaction of a selection of model organic molecules with the major surfaces of both hematite (α-Fe_2O_3) and maghemite (γ-Fe_2O_3).

5.2 Surfactants Molecules

We have investigated the adsorption of two organic molecules, namely methanoic acid and hydroxyethanal, where hydroxyethanal provides us with information about the effect of a larger more flexible molecule by increasing the chain length which also affects the functional group. Hydroxyethanal contains two kinds of functional group, an aldehyde and a hydroxyl group where the =O and –OH of the carboxylic acid group are in methanoic acid effect separated by an extra carbon atom, adding flexibility to the molecule. We will consider two initial configurations of hydroxyethanal, a staggered and eclipsed conformer, although the molecules are free to rotate during the simulations.

5.2.1 Methanoic acid

Methanoic acid is a simple planar molecule; (**Figure 5.1**) the smallest carboxylic acid, also called formic acid and hydrogen carboxylic acid. In the interatomic potential model both oxygen atoms of methanoic acid are assigned the same partial charge of -0.380 eV, but during the adsorption processes we have found that the carbonyl oxygen atom is the more accessible to coordinate to the surface and in most cases, methanoic acid coordinates to the surface through this atom, although sometimes methanoic acid coordinates to the surface through both oxygen atoms, depending on the nature of the surface ,i.e. geometry and type of surface ions.

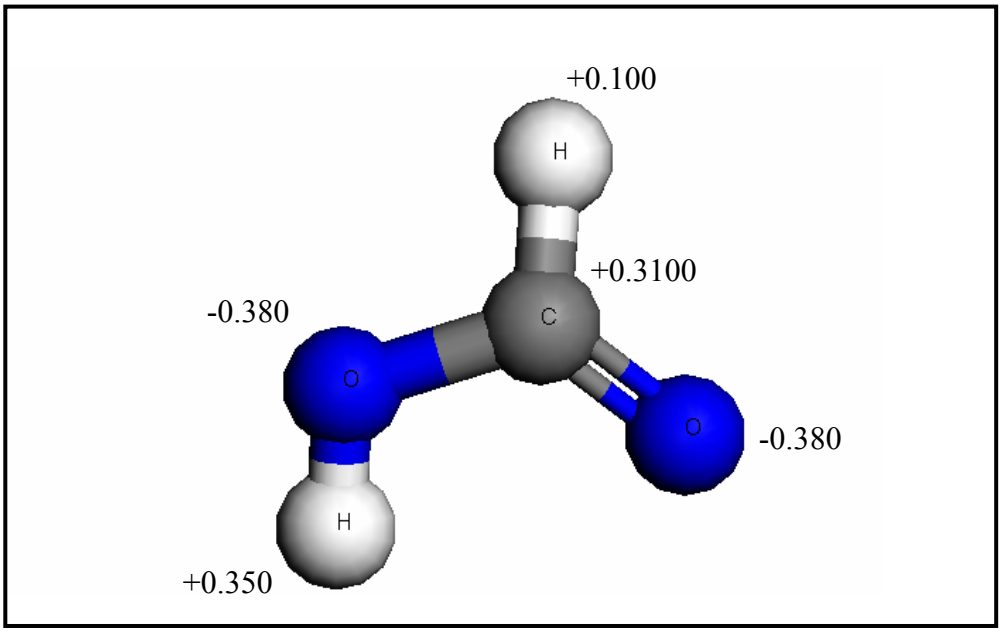

Figure 5.1: The methanoic acid molecule, showing the partial charges on the atoms. Key :(Carbon=Grey, Oxygen= dark blue and Hydrogen =White).

Throughout this chapter we shall refer to the atoms of methanoic acid molecule as follows: the oxygen atom which is part of the hydroxyl group will be referred to as hydroxyl oxygen atom; then there is the carbonyl oxygen atom, or doubly bonded oxygen atom; the hydroxyl hydrogen atom, which forms part of the hydroxyl group, and the carbonyl hydrogen atom, which is attached to the carbon atom of the carbonyl group.

5.2.2 Hydroxyethanal

We have used hydroxyethanal to investigate the effect of increasing the carbon chain length and position of the oxygen ions on the strength of the interaction with the mineral surfaces, where we expect that the strength of the interaction will

depend on the overall structure of the molecule as well as the nature of the surface (Schwarzenbach *et al*., 2003).

Hydroxyethanal has a hydroxyl group and a separate aldehyde group, as shown in **Figure 5.2**, in contrast with methanoic acid, where the =O and -OH are both on the same carbon. In this study we have considered two configurations of hydroxyethanal that have been labelled as the eclipsed and staggered conformers according to the position of the two oxygen atoms on the hydroxyethanal molecule (**Figure 5.2**). The staggered configuration of the free hydroxyethanal molecule is the lowest energy conformer, although during the simulation the staggered conformer would sometimes rotate itself to form the eclipsed configuration at the surface. Therefore, considering both conformers in our study allows us to be confident that we did not overlook an energetically more stable mode of adsorption for these molecules.

Hydroxyethanal can coordinate to the surface by either or both of its oxygen atoms, but in most cases hydroxyethanal coordinates to the surface through the carbonyl oxygen atom, which is the more accessible of the two oxygen atoms. As in methanoic acid we will refer to the oxygen atoms of the hydroxyethanal molecule as follows: the oxygen atom which is part of the hydroxyl group will be referred to as hydroxyl oxygen atom; and then there is the carbonyl oxygen atom, which is part of the carbonyl (aldehyde) group; hydroxyethanal has three types of hydrogen atoms and throughout this chapter they will be referred to as the hydroxyl hydrogen atom, which is part of the hydroxyl group; the carbonyl

hydrogen; and finally the two hydrogen atoms that are attached to the hydroxyl carbon atom will be labelled as carbon hydrogen atoms.

In our investigation we have calculated a large number of initial starting positions and orientations for both methanoic acid and hydroxyethanal to the different surface sites to identify the energetically most favorable location, rather than a local minimum.

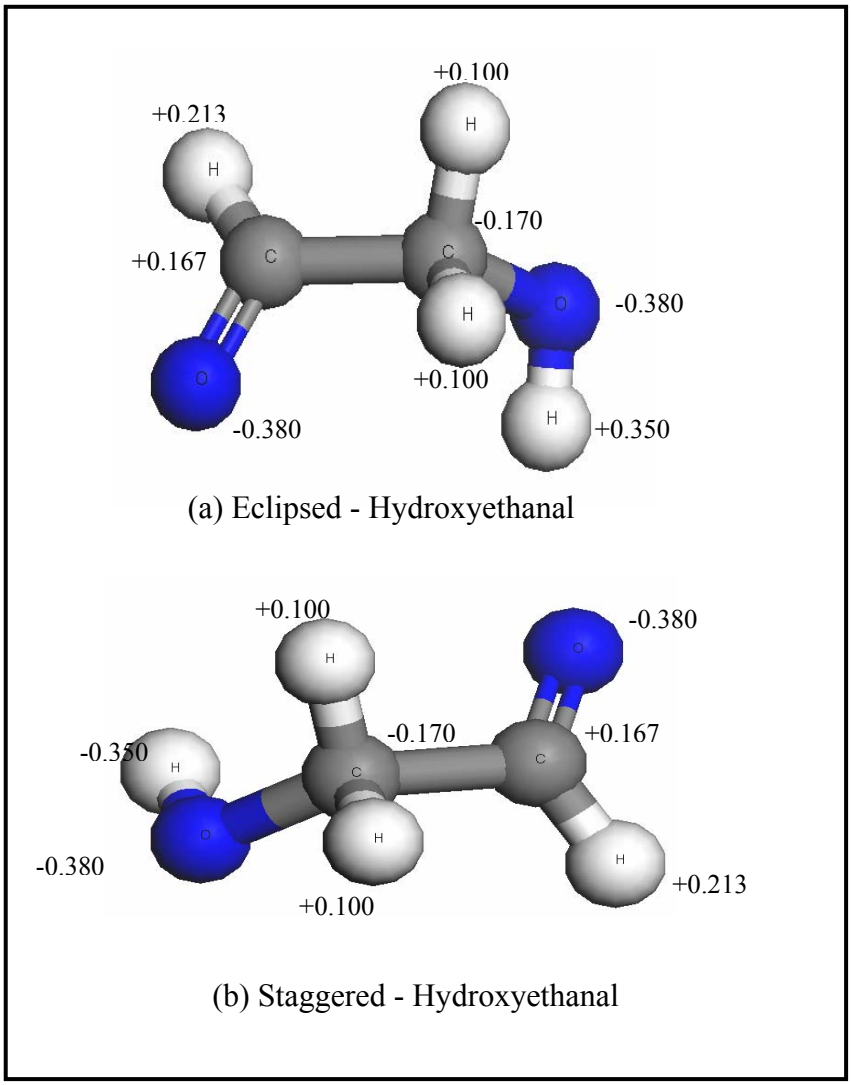

Figure 5.2: a) Eclipsed-hydroxyethanal with two oxygen atoms on the same side of the molecule and b) Staggered-hydroxyethanal with two oxygen atoms on opposite sides of the molecule. Key: (Carbon=Grey, Oxygen=dark blue and Hydrogen =White).

5.3 Mineral Surfaces

In this study we have considered the adsorption of methanoic acid and two conformers of hydroxyethanal to both hematite (α-Fe_2O_3) and maghemite (γ-Fe_2O_3) surfaces. Initially, we have studied the interaction of methanoic acid with the most stable termination of each dehydrated surface of the two minerals, as described in **Chapter 4**, where we have focused on the dominant surfaces of the two iron oxide minerals, which are important in the morphology. To investigate the adsorption of the methanoic acid and hydroxyethanal with the hydroxylated surfaces, we have again considered the most stable termination for each surface, which could be different from the dehydrated terminations as some terminations that were less stable became more stable after hydroxylation. The seven surfaces of hematite have been studied including the {0001} and $\{11\bar{2}0\}a$ planes, which are the most common cleavage planes and expressed in the dry morphology. We will describe in detail the iron termination of the {0001} surface, as it is the dominant termination under dry conditions, and the oxygen termination of the {0001}, as it is the dominant termination when hydroxylated. The $\{10\bar{1}1\}a$ and $\{11\bar{2}0\}a$ surfaces are considered because these are both morphologically important surfaces and we have also investigated the $\{10\bar{1}0\}a$ and $\{11\bar{2}1\}b$ surfaces.

In maghemite the main {010} iron and {001}oxygen surfaces will be studied, as well as other surfaces shown to be stable either as dehydrated surfaces or after hydroxylation: {110}, {103} and {113}.

5.4 Adsorption to Hematite

The most exothermic adsorption energies are listed for each surfactant to each hematite surface in **Table 5.1**.

Table 5.1: Calculated adsorption energies ($kJmol^{-1}$) for methanoic acid and two conformers of hydroxyethanal at relaxed dehydrated and hydroxylated hematite surfaces.

Surface	Adsorption energy($kJmol^{-1}$)					
	Methanoic acid		Hydroxyethanal		Hydroxyethanal	
			Staggered	Eclipsed	Staggered	Eclipsed
	dry	hydroxylated	dry		hydroxylated	
{0001}Fe	-119.3	-74.0	-139.4	-139.1	-94.5	-127.6
{0001}Ox	-107.0	-45.4	-126.6	-151.1	-51.0	-81.1
$\{10\bar{1}0\}$a	-117.8	-42.31	-134.1	-140.0	-57.8	-89.4
$\{10\bar{1}1\}$a	-122.5	-30.4	-153.8	-160.0	-41.1	-71.2
$\{11\bar{2}0\}$a	-120.7	-37.0	-170.3	-170.3	-48.3	-75.8
$\{01\bar{1}2\}$a	-118.8	-117.8	-149.8	-155.5	-109.3	-148.3
$\{11\bar{2}1\}$b	-137.4	-51.6	-175.1	-195.9	-55.7	-83.5

5.4.1 Adsorption of Methanoic acid at the Dehydrated Surfaces

Firstly, we investigated the interaction of methanoic acid with the dehydrated hematite surfaces. Our simulations show that the most favourable mode of adsorption for methanoic acid is by coordinating to one surface iron atom through the carbonyl oxygen atom, and this type of configuration is seen on all dehydrated hematite surfaces. In addition, hydrogen bonding between most of the available hydrogen atoms and surface oxygen atoms also plays an important role. However, we shall describe in detail the interaction between methanoic acid and the most important surfaces.

In the lowest-energy configuration, the methanoic acid molecule adsorbed at the oxygen-terminated {0001} surface releases an adsorption energy of 107.0 $kJmol^{-1}$. Here the carbonyl oxygen atom is adsorbed at a distance of 1.89 Å on top of the surface to an iron atom which is under-coordinated and hence reactive. In addition, the hydroxyl hydrogen atom interacts with the surface through weak hydrogen-bonding to two surface oxygen atoms at distances of 2.00 Å and 2.30 Å. The surface/adsorbate system is shown in **Figure 5.3**.

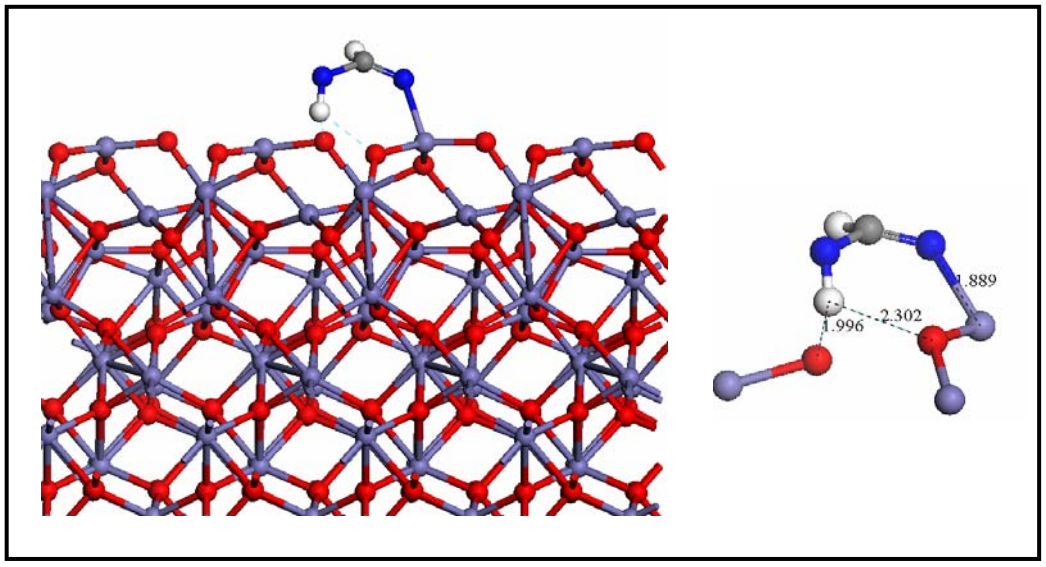

Figure 5.3: Lowest-energy optimised structure of methanoic acid adsorbed at the dehydrated hematite oxygen-terminated {0001} surface, showing interatomic distances (Å) between the adsorbate and surface species. Key: (Iron = blue, Oxygen (surface) = red, Oxygen (methanoic acid) = dark blue, Carbon=Grey and Hydrogen = White).

However, the calculated adsorption energies listed in **Table 5.1** show that the adsorption of methanoic acid onto Fe-terminated {0001} surface is energetically more favourable (-119.3 $kJmol^{-1}$) than onto the oxygen-terminated {0001} surface. The Fe-terminated surface is a comparatively flat surface, as described in **Chapter 4**. Upon relaxation, the methanoic acid molecule has adsorbed to the surface via electrostatic interaction between the carbonyl oxygen atom of the molecule and one surface iron atom at a bond distance of 1.92 Å. On this surface the hydroxyl hydrogen atom is located almost equidistant from three surface oxygen atoms, forming a tetrahedral structure with H…O distances ranging from 2.05 Å - 2.07 Å. The least energetically favorable mode for the adsorption of methanoic acid onto the Fe-terminated {0001} surface, releasing an adsorption energy of 29.1 $kJmol^{-1}$,

was found when the methanoic acid adsorbed to the surface as a flat molecule at a longer distance as displayed in **Figure 5.4**(**b**).

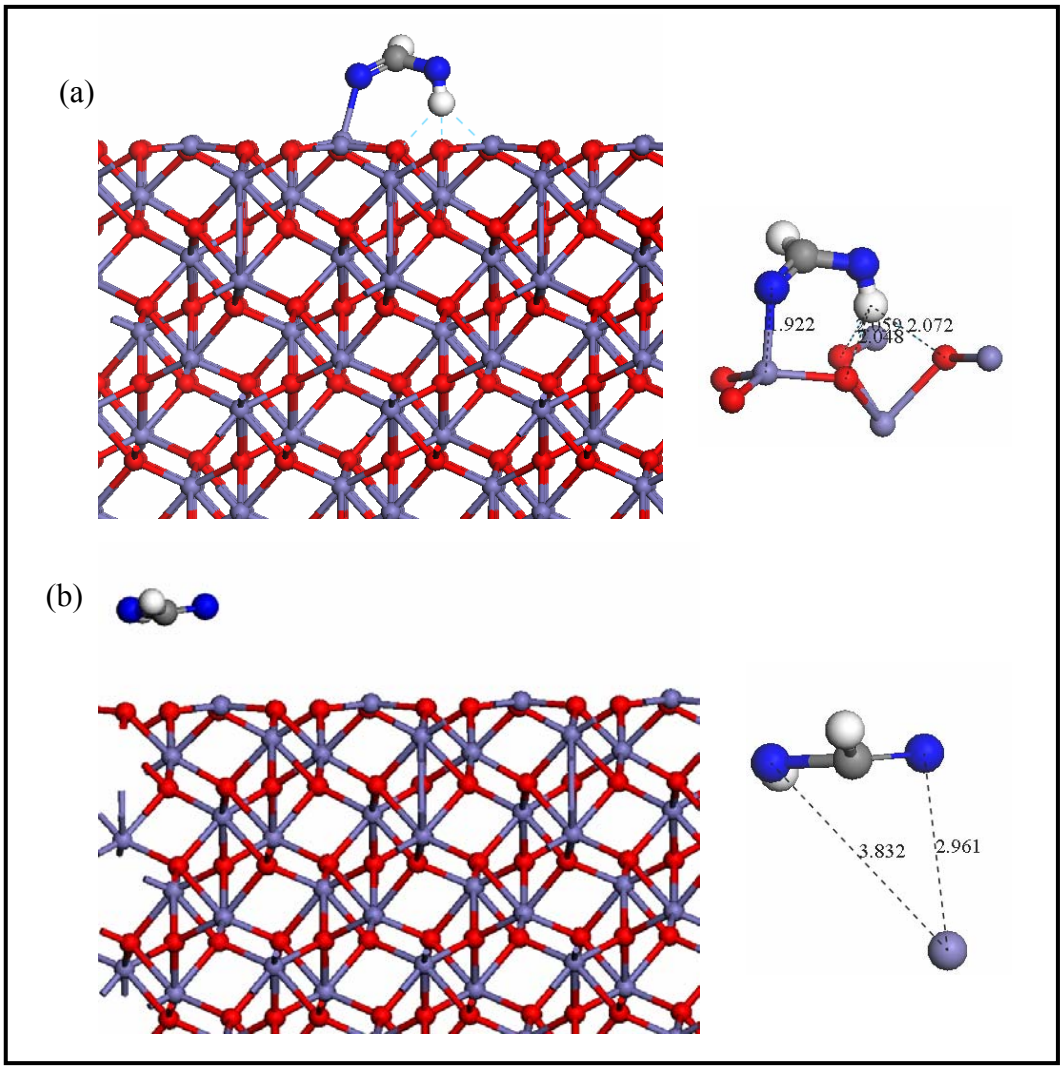

Figure 5.4: Geometry optimised structures of two different configurations of methanoic acid adsorbed at the dehydrated hematite iron-terminated {0001} surface. (a) lowest-energy optimised structure and (b) highest-energy optimised structure, showing interatomic distances (Å) between the adsorbate and surface species. Key: (Iron = blue, Oxygen (surface) = red, Oxygen (methanoic acid) = dark blue, Carbon=Grey and Hydrogen = White).

In addition to the {0001} surface, the methanoic acid is also adsorbed on the $\{10\bar{1}1\}a$ surface. As discussed before in **Chapter 4**, the $\{10\bar{1}1\}a$ is by far the least stable surface compared with the other dehydrated hematite surfaces, which therefore may be expected to be reactive towards adsorption of the methanoic acid molecule, which is adsorbed with an adsorption energy of 122.5 $kJmol^{-1}$. The methanoic acid molecule is almost perpendicular to the surface as displayed in **Figure 5.5**. Here the carbonyl oxygen atom is adsorbed on top of the surface to the under-coordinated and hence reactive iron atom at a distance of 1.93 Å. The hydroxyl hydrogen atom of the methanoic acid molecule interacts with two surface oxygen atoms through hydrogen-bonding interactions at distances of between 2.09 Å and 2.23 Å, although the carbonyl hydrogen atom cannot interact with the surface as it is pointed away from the surface. The electrostatic interaction between the carbonyl oxygen atom and the iron surface ion and the hydrogen-bonds between the hydroxyl hydrogen atom and the oxygen surface ions give rise to strong binding of the methanoic acid to the $\{10\bar{1}1\}a$ surface of hematite.

There are other configurations of the adsorbate molecule which lead to strong interactions between the surface and the molecule, for example, when the methanoic acid molecule adsorbs almost flat onto the surface, where a number of close interactions are formed between the molecule's carbonyl oxygen atom O=C or hydroxyl oxygen atom –OH and two surface iron atom ($Fe_{surface}$ …$O{=}C_{methanoic\ acid}$=2.29 Å and $Fe_{surface}$…$OH_{methanoic\ acid}$ =2.22 Å), as well as hydrogen-bonding interactions between the hydroxyl hydrogen atom and a surface oxygen atom at a distance of 1.79 Å (E_{ads} = -118.4 $kJmol^{-1}$).

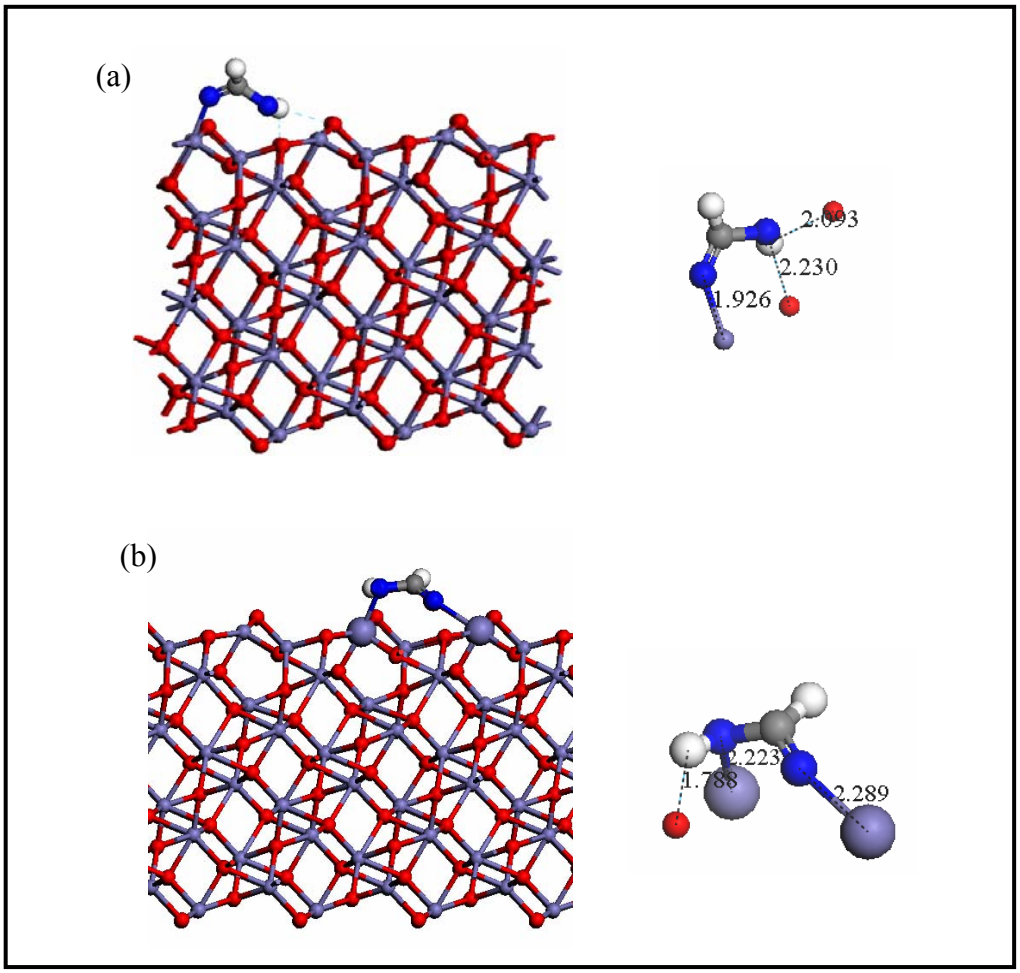

Figure 5.5: Geometry-optimised structures of two different configurations of methanoic acid adsorbed at the dehydrated hematite $\{10\bar{1}1\}a$ surface. (a) lowest- energy optimised structure and (b) highest- energy optimised structure, showing interatomic distances (Å) between the adsorbate and surface species. Key :(Iron = blue, Oxygen (surface) = red, Oxygen (methanoic acid) = dark blue, Carbon=Grey and Hydrogen = White).

Similarly to the iron-terminated $\{0001\}$ and $\{10\bar{1}0\}a$ surfaces the methanoic acid molecule adsorbs onto the $\{01\bar{1}2\}a$ surface with an adsorption energy -118.8 kJmol^{-1}. These three different surfaces are close in surface energies (±0.12 Jm^{-2}) and relatively stable (**Table 4.1**, **Chapter 4**), due to their

well-ordered surface structures. As a result adsorption of the methanoic acid molecule releases less energy in comparison with the other dehydrated hematite surfaces, because the stability of the surfaces makes them less reactive towards adsorption of mechanic acid or other impurities.

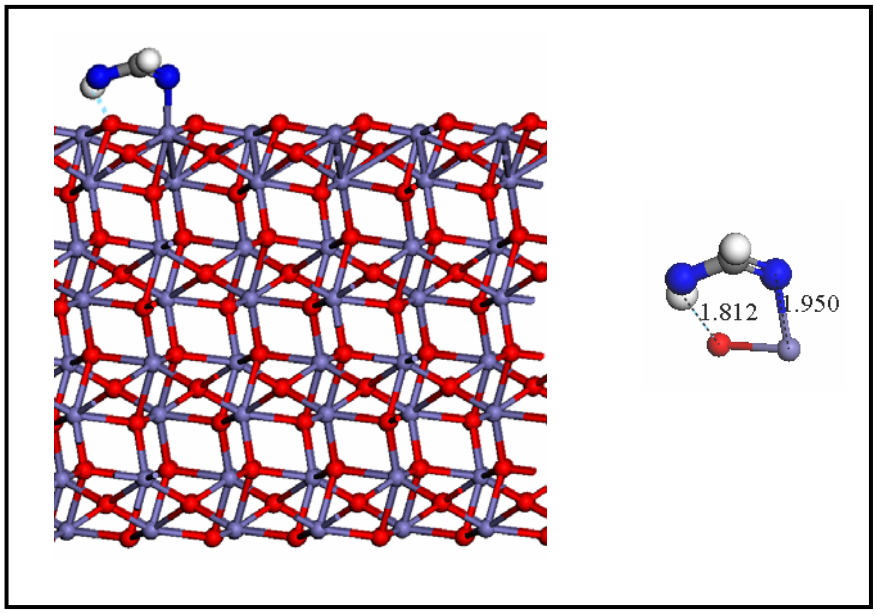

Figure 5.6: Lowest-energy optimised structure of methanoic acid adsorbed at the dehydrated hematite oxygen-terminated $\{01\bar{1}2\}a$ surface, showing interatomic distances (Å) between the adsorbate and surface species. Key: (Iron = blue, Oxygen (surface) = red, Oxygen (methanoic acid) = dark blue, Carbon=Grey and Hydrogen = White).

Adsorption of methanoic acid onto the $\{11\bar{2}1\}b$ surface is more energetically favourable (-137.4 $kJmol^{-1}$) in comparison with all other dehydrated hematite surfaces because it is one of the least stable surfaces. Again the initial positions and configurations of the adsorbate molecule have a significant effect on the final surface/adsorbate system and thus the strength of adsorption of molecule onto the surface. In the lowest-energy configuration (E_{ads} = -137.4 $kJmol^{-1}$) the carbonyl

oxygen atom of methanoic acid molecule is adsorbed to the under-coordinated iron atom just below the oxygen on top of the surface at a bond distance of 2.01 Å which is shorter than the distance between the iron and oxygen on the surface ($Fe_{surface}$ …$Ox_{surface}$ = 2.03 Å). The Fe on the surface now is five coordinated (**Figure 5.7**(**a**)). In addition, a hydrogen-bond has formed between the hydroxyl hydrogen atom and a surface oxygen atom at a distance of 1.82 Å. Other low-energy configurations are also shown in **Figure 5.7**(**b**) and (**c**).

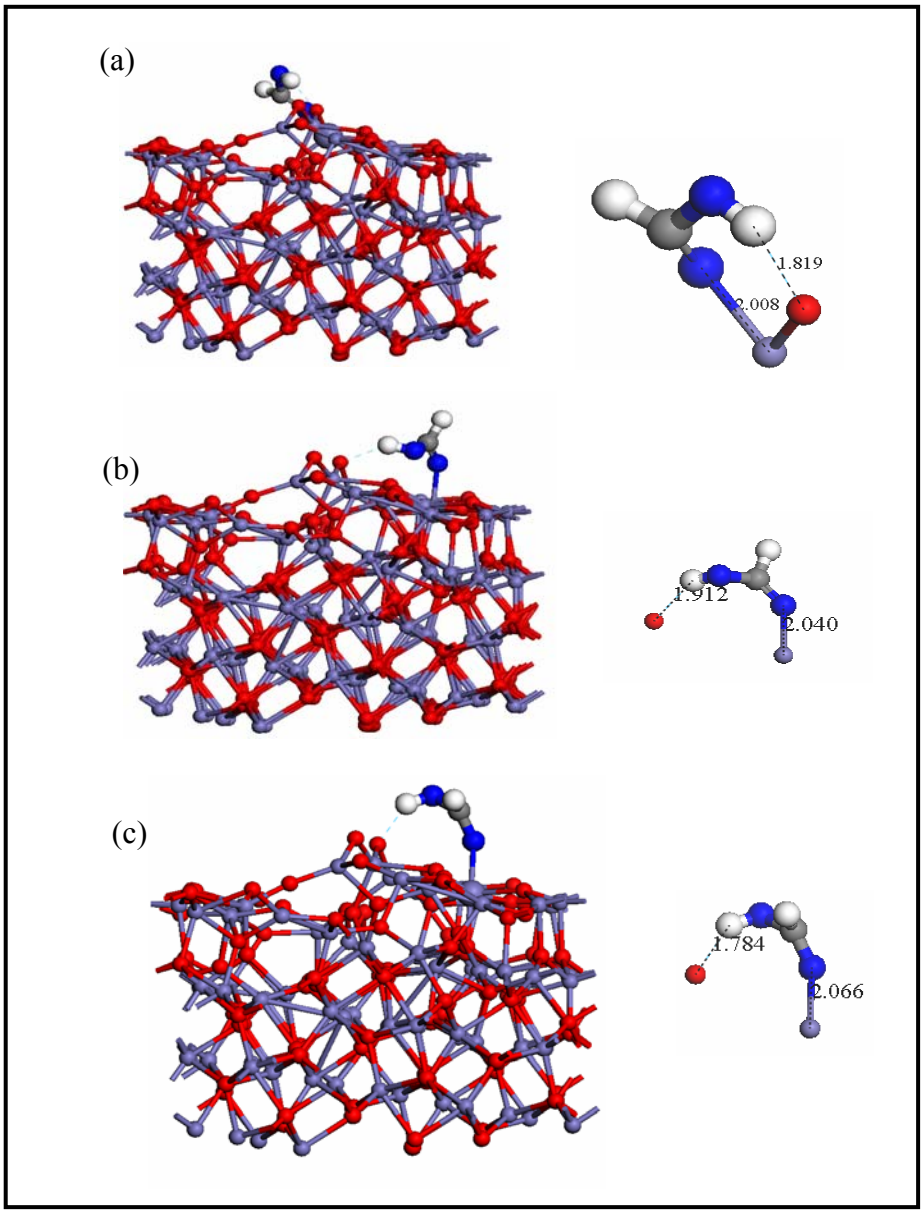

Figure 5.7: Geometry-optimised structures of three different configurations of methanoic acid adsorbed at the dehydrated hematite $\{11\bar{2}1\}$b surface in the lowest energy positions, showing interatomic distances (Å) between the adsorbate and surface species. Key: (Iron = blue, Oxygen (surface) = red, Oxygen (methanoic acid) = dark blue, Carbon=Grey and Hydrogen = White).

In summary, the adsorption energies of methanoic acid molecule at the surfaces of hematite (α-Fe_2O_3) listed in **Table 5.1**, show that the methanoic acid molecule interacts strongly with all dehydrated hematite surfaces. However, the adsorbate binds more strongly to the $\{11\bar{2}1\}b$ surface than, for example, to the {0001} iron and oxygen terminated surfaces. The Fe-terminated {0001} surface is a stable surface before adsorption, and as a result the methanoic acid molecule has little effect on the surface structure. The $\{11\bar{2}1\}b$ surface is less stable than the {0001}Fe surface, which is due to a large number of under-coordinated surface species, making the $\{11\bar{2}1\}b$ surface more reactive than the {0001}Fe surface. In general, the less stable surface is more reactive towards adsorption of impurities.

When we compare the adsorption energies for the methanoic acid at the three different surfaces {0001}Fe, $\{01\bar{1}2\}a$ and $\{10\bar{1}0\}a$ (**Table 5.1**), we see that the energies released upon adsorption do not vary much, possibly due to any of the following reasons:(i)These different surfaces have very similar stabilities exemplified by their similar surface energies (±0.12 Jm^{-2}); (ii) They are all well-ordered ; (iii) The distance between the surface iron and carbonyl oxygen atom as result of the interaction between the surface and molecule is very similar, as is the hydrogen-bonding distance as a result of the interaction between the hydroxyl hydrogen atom of methanoic acid molecule to a surface oxygen atom on each surface.

5.4.2 Adsorption of Hydroxyethanal at the Dehydrated Surfaces

Hydroxyethanal adsorbs in a different way to methanoic acid, which is not surprising because the structures of the two carboxylic acid molecules are different due to the presence of the extra carbon atom between the two oxygen groups compared to the methanoic acid, which adds flexibility to the molecule, allowing more easily interaction of both oxygen atoms with the surface. In general, both staggered and eclipsed conformers of hydroxyethanal interact with the surface by bridging via its two oxygen atoms between two surface iron atoms. This type of interaction is seen on both iron- and oxygen-terminated {0001} surface, and also on the $\{11\bar{2}0\}a$ and $\{01\bar{1}2\}a$ surfaces. Also, we find that sometimes adsorption of hydroxyethanal in an eclipsed conformation is energetically preferred over a staggered conformation, even though the free molecule is more stable in the staggered conformation than as an eclipsed conformer. In all cases, the hydrogen-bonded interactions between the adsorbates' hydrogen atoms and surface oxygen atoms play an important role in further stabilising the adsorption of the hydroxyethanal molecules, on the surfaces.

On the oxygen-terminated {0001} surface both conformers of hydroxyethanal adsorb to the surface by bridging between two surface iron atoms releasing adsorption energies of 126.6 $kJmol^{-1}$ and 151.1 $kJmol^{-1}$ for the initially staggered and eclipsed-hydroxyethanal, respectively. However, the adsorbates are all free to

rotate and rearrange during optimisation and here the hydroxyethanal adsorbs in an eclipsed fashion.

In one low energy configuration from the initially eclipsed hydroxyethanal on the {0001}Ox surface, the molecule coordinates to two different surface iron atoms, through the carbonyl oxygen atom at distance of $Fe_{surface}$…O=C = 1.99 Å, and through the hydroxyl oxygen atom to the second iron surface atom at a distance of $Fe_{surface}$…OH =2.20Å, shown in **Figure 5.8**(**a**). Similarly, the adsorption mode of the lowest-energy configuration starting from the staggered hydroxyethanal, leaves the molecule adsorbed onto the surface by bridging two surface irons atoms through the carbonyl oxygen atom at a distance $Fe_{surface}$…O=C = 1.94 Å and through the hydroxyl oxygen atom with another surface iron atom at a distance of $Fe_{surface}$…OH =2.21 Å. In **Figure 5.8** we have shown the two lowest-energy structures of hydroxyethanal adsorbed at the {0001}Ox surfaces of dehydrated hematite .

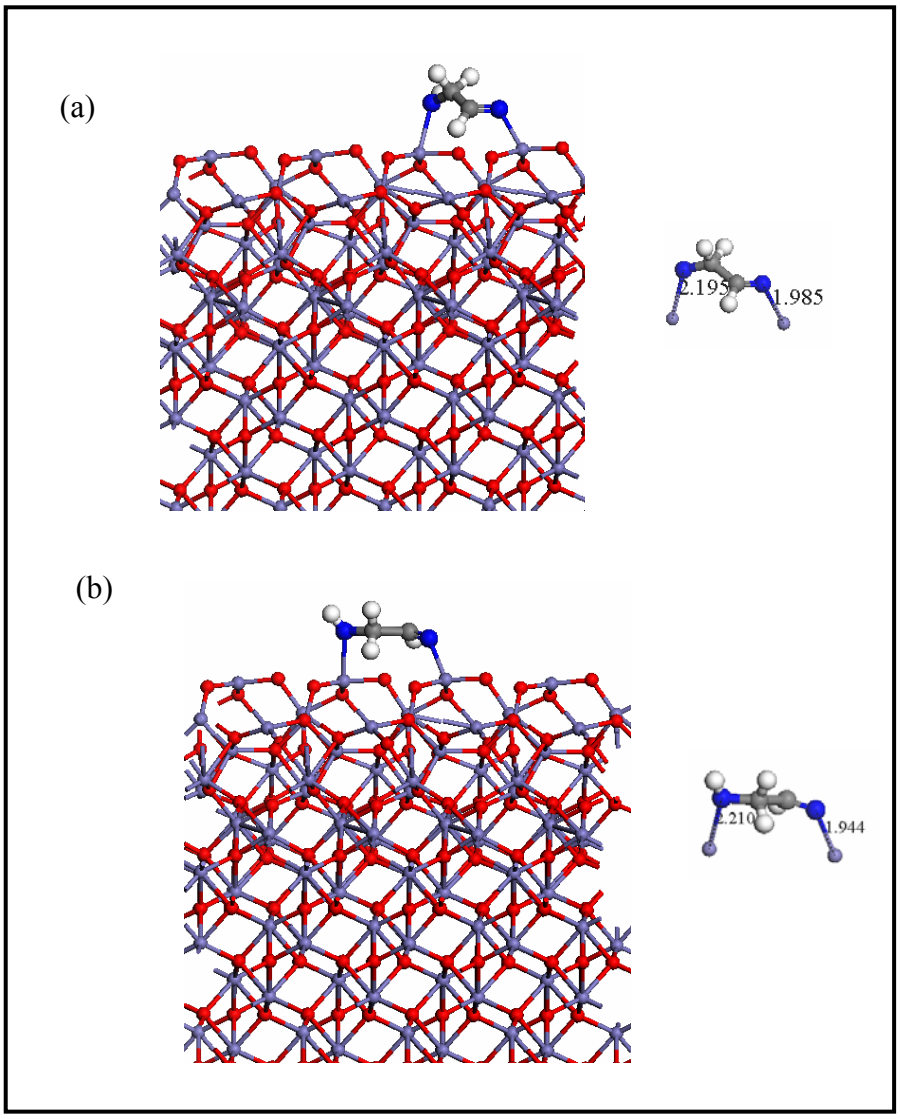

Figure 5.8: Geometry-optimised structures of two low-energy surface/adsorbate structures of hydroxyethanal adsorbed at the dehydrated hematite {0001}Ox surface, showing interatomic distances (Å) between the adsorbate and surface species. Key: (Iron = blue, Oxygen (surface) = red, Oxygen (hydroxyethanal) = dark blue, Carbon=Grey and Hydrogen = White).

The adsorption of hydroxyethanal to the iron-terminated {0001} surface is energetically significantly less favorable than onto the oxygen-terminated surface releasing adsorption energies of -139.4 $kJmol^{-1}$ and -139.1 $kJmol^{-1}$ for the initially staggered and eclipsed hydroxyethanal respectively. Both bridge two surface iron atoms and similarly to the oxygen-terminated surface, the two forms of the hydroxyethanal molecule are unable to form hydrogen-bonds with the molecule when adsorbed onto the surface, as shown in **Figure 5.9**(**a**) and (**b**) for the initially eclipsed and staggered hydroxyethanal respectively.

Sometimes, the molecule adsorbs to the surface through its carbonyl oxygen only, which lowers the adsorption energy. In the extreme case, the molecule does not form any close interactions and because only weakly physiosorbed to the surface. **Figure 5.9** shows some of the main structures identified in our simulation.

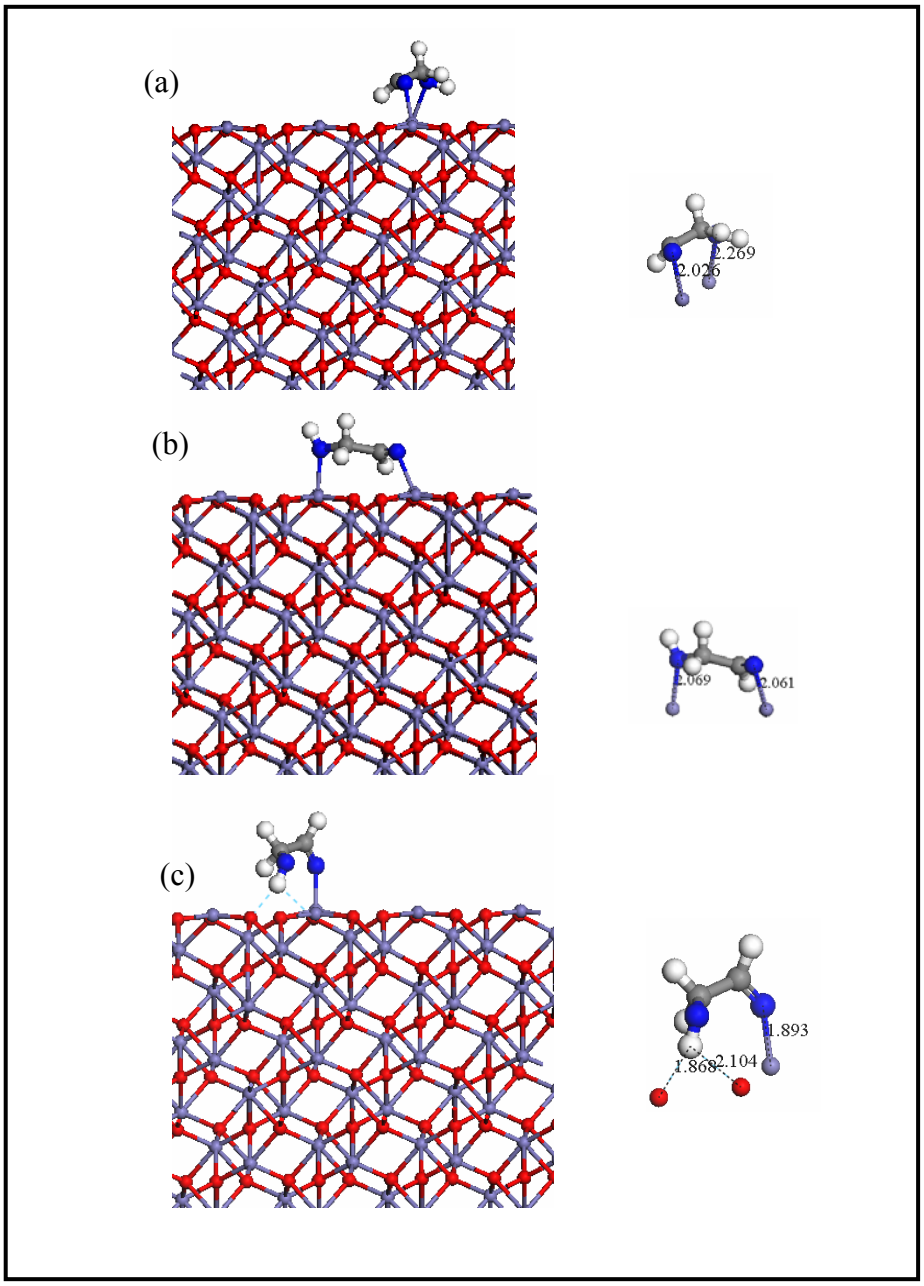

Figure 5.9: Geometry-optimised structures of three low-energy surface/adsorbate structures of hydroxyethanal adsorbed at the dehydrated hematite {0001}Fe surface, showing interatomic distances (Å) between the adsorbate and surface species. Key: (Iron = blue, Oxygen (surface) = red, Oxygen (hydroxyethanal) = dark blue, Carbon=Grey and Hydrogen = White).

Although the adsorption of hydroxyethanal on the $\{01\bar{1}2\}a$ and $\{10\bar{1}1\}a$ surfaces is preferred in an eclipsed fashion, the adsorption modes of the eclipsed hydroxyethanal at these two dehydrated hematite surfaces is different. The lowest energy configuration from the eclipsed hydroxyethanal adsorbed at the $\{01\bar{1}2\}a$ surface is similar as seen before at both iron- and oxygen-terminated $\{0001\}$ surfaces. However, on the $\{10\bar{1}1\}a$ surface, the eclipsed hydroxyethanal adsorbs onto the surface by coordinating by its carbonyl oxygen to one surface iron atom at a distance of 1.88 Å, and in addition, forming a hydrogen-bond between one surface oxygen atom and the hydroxyl hydrogen of hydroxyethanal at a distance of 1.84 Å. **Figure 5.10** shows the lowest-energy optimised structures for adsorption of hydroxyethanal at the $\{01\bar{1}2\}a$ and $\{10\bar{1}1\}a$ surfaces.

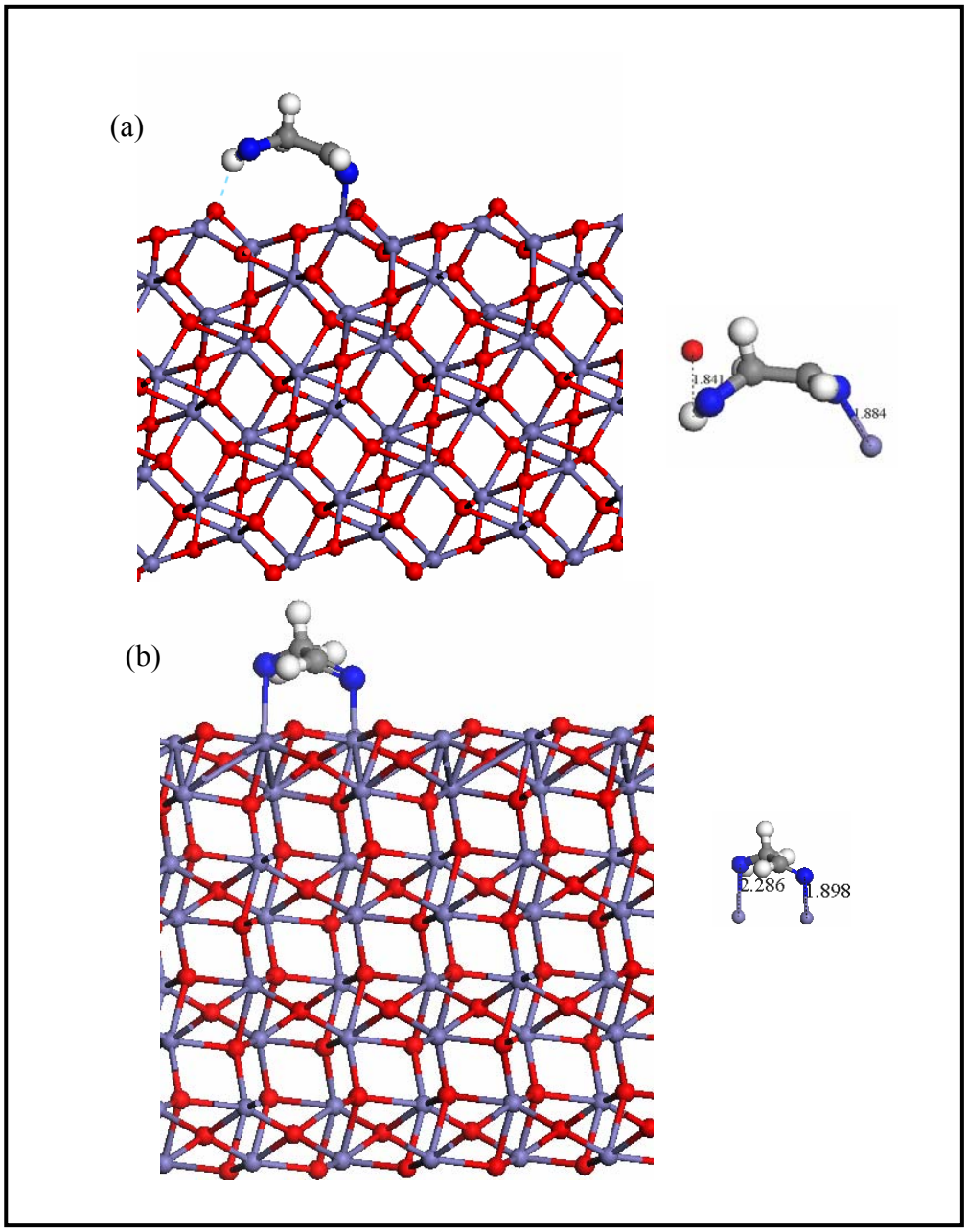

Figure 5.10: Geometry-optimised structures of two low-energy surface/adsorbate structures of hydroxyethanal adsorbed at the dehydrated hematite. (a) $\{10\bar{1}1\}$a and (b) $\{01\bar{1}2\}$a surfaces, showing interatomic distances (Å) between the adsorbate and surface species. Key: (Iron = blue, Oxygen (surface) = red, Oxygen (hydroxyethanal) = dark blue, Carbon=Grey and Hydrogen = White).

However, sometimes the spacing between the surface iron atoms is not large, which will not allow the oxygen atoms of the adsorbate molecule to bridge between two surface iron atoms. For example, both conformers of hydroxyethanal adsorb to the $\{10\bar{1}0\}a$ in the same mode by coordinating through their carbonyl oxygen atom to only one surface iron atom. The hydroxyethanal molecules still adsorb releasing relatively large energies,-134.1 $kJmol^{-1}$ to -140.0 $kJmol^{-1}$ for the lowest energy structures of the initially staggered and eclipsed hydroxyethanal respectively. Again, the hydroxyethanal prefers to adsorb onto the $\{10\bar{1}0\}a$ surface in an eclipsed fashion. **Figure 5.11** shows the three lowest energy structures identified in our simulations.

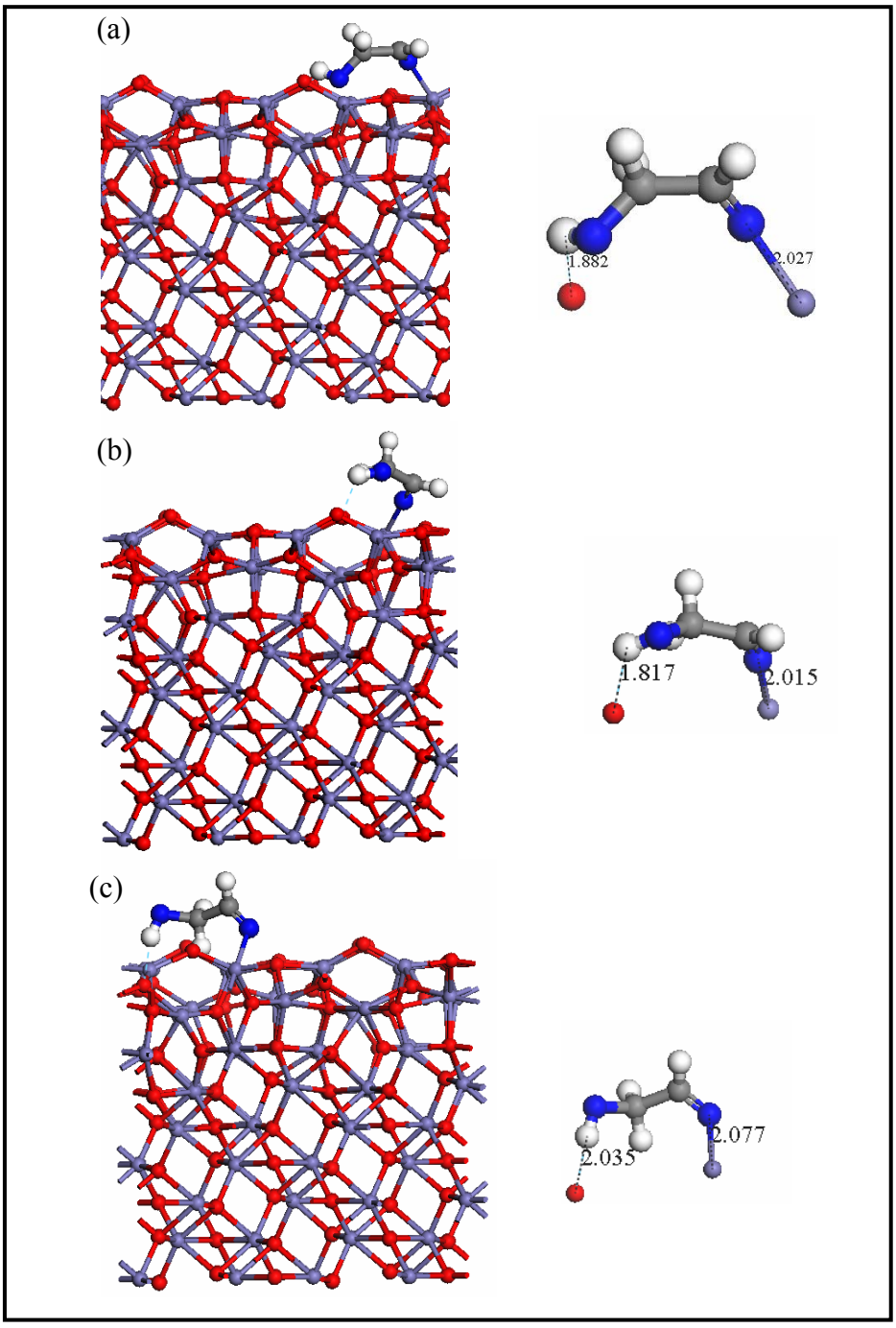

Figure 5.11: Geometry-optimised structures of three low-energy surface/adsorbate structures of hydroxyethanal adsorbed at the dehydrated hematite $\{10\bar{1}0\}$a surface, showing interatomic distances (Å) between the adsorbate and surface species. Key: (Iron = blue, Oxygen (surface) = red, Oxygen (hydroxyethanal) = dark blue, Carbon=Grey and Hydrogen = White).

Our simulations show that the hydroxyethanal binds strongly to the $\{11\bar{2}1\}b$ surface, releasing relatively large energies (-175.1 $kJmol^{-1}$ to -195.9 $kJmol^{-1}$), which that may due to the unstable nature of the surface.

In the lowest-energy optimised structure (**Figure 5.12**(**a**)) the molecule coordinates to only one iron surface atom via its hydroxyl oxygen atom at a bond distance of ($Fe_{surface}$ …OH =2.31 Å). The hydroxyethanal molecule is able to span 3.33 Å wide but on this surface the carbonyl group is not able to interact with another surface iron atom. However, adsorption is stabilised further by hydrogen-bonding via the hydroxyl hydrogen atom, which is in close enough proximity to one surface oxygen atom at a distance of ($O_{surface}$ …HO =2.01 Å).

In a different configuration (**Figure 5.12**(**b**)) the molecule does bridge two surface iron atoms, interaction strongly via its carbonyl oxygen atom at a distance of ($Fe_{surface}$ …O=C = 2.09 Å), and more weakly via the hydroxyl oxygen atom at a distance of ($Fe_{surface}$ …OH=2.17 Å). **Figure 5.12** shows the two lowest-energy structures for the adsorption of hydroxyethanal at the $\{11\bar{2}1\}b$ surface.

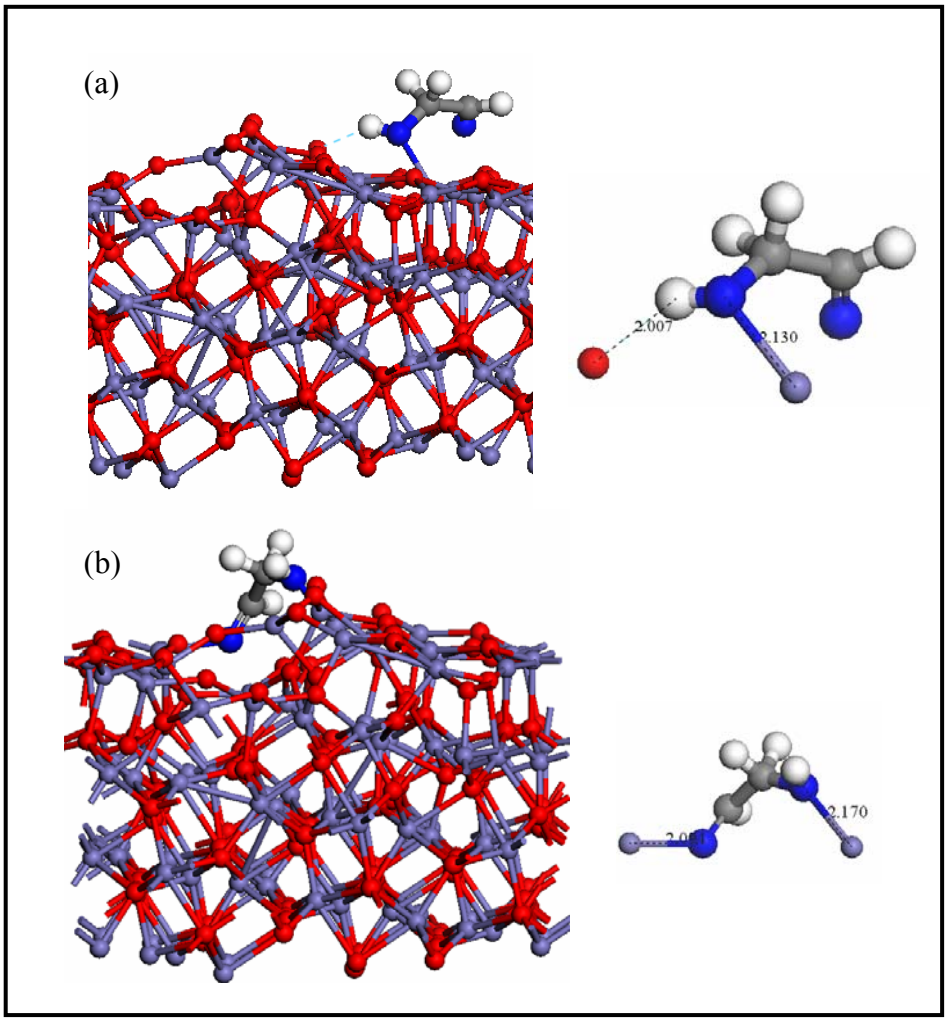

Figure 5.12: Geometry optimised structures of two low-energy surface/adsorbate structures of hydroxyethanal adsorbed at the dehydrated hematite $\{11\bar{2}1\}$b surface.(a) hydroxyethanal coordinating to one surface iron atom and (b) hydroxyethanal bridging between two surface iron atoms, showing interatomic distances (Å) between the adsorbate and surface species. Key: (Iron = blue, Oxygen (surface) = red, Oxygen (hydroxyethanal) = dark blue, Carbon=Grey and Hydrogen = White).

In summary, the largest adsorption energies of the initially staggered and eclipsed conformers of hydroxyethanal at the surfaces of hematite (α-Fe_2O_3) are listed in **Table 5.1**. Both interact strongly with all dehydrated hematite surfaces, via both oxygen atoms of carbonyl and hydroxyl groups, and on most surfaces the molecule adsorbs onto the surface by bridging between two surface iron atoms. In addition, adsorption is sometimes stabilised by hydrogen-bonding between surface oxygen atoms and the hydroxyl hydrogen atom, depending on the rotation and position of the molecule. Generally, the adsorption of hydroxyethanal is more favourable when the molecule is initially in the eclipsed conformer.

5.4.3 Adsorption of Methanoic acid at the Hydroxylated Surfaces

We have extended our work to investigate the effect of the same molecules at the hydroxylated hematite surfaces; which will be their usual state in the natural environment. The adsorption energies are now calculated with respect to the hydroxylated surface, and the results are listed in **Table 5.1**. We see that on most surfaces, the methanoic acid molecule does not adsorb strongly because, the addition of water through hydroxylation has significantly stabilised the surfaces.

When methanoic acid is adsorbed on the hydroxylated {0001}Fe surface, the carbonyl oxygen atom of the methanoic acid coordinates to the four-fold coordinated iron surface atom at a distance of 2.13Å, whilst the dissociatively adsorbed water molecules remain in a similar geometry upon adsorption of methanoic acid as is seen on the purely hydroxylated surface. The surface is

further stabilised by extra interactions, where some hydrogen-bonds form between the carbonyl oxygen atom of methanoic acid and hydroxyl hydrogen atom of the surface at a distance of 2.35 Å, and between the hydroxyl hydrogen atom of the adsorbate molecule and the closest oxygen atom of the hydroxylated surface at a distance of 1.88 Å.

From our results in **Table 5.1**, we can see that the adsorption of methanoic acid onto the hydroxylated oxygen-terminated surface in the lowest energy position releases an adsorption energy of -45.4 $kJmol^{-1}$. Upon relaxation, the hydroxyl hydrogen atom of methanoic acid molecule interacts with two surface oxygen atoms to form a weak hydrogen-bonding interaction at distances of 2.04 Å and 2.12 Å. However, the adsorption of methanoic acid onto the surface has little effect on the regular pattern of adsorption of dissociative water molecules as seen on the hydroxylated surface on its own. There are few hydrogen bonds between the dissociatively adsorbed water molecules, and surface oxygen atoms, and there is also little interaction between the adsorbed methanoic acid molecule and surrounding dissociatively water molecules on the hydroxylated surface, as shown in **Figure 5.13**(**b**).

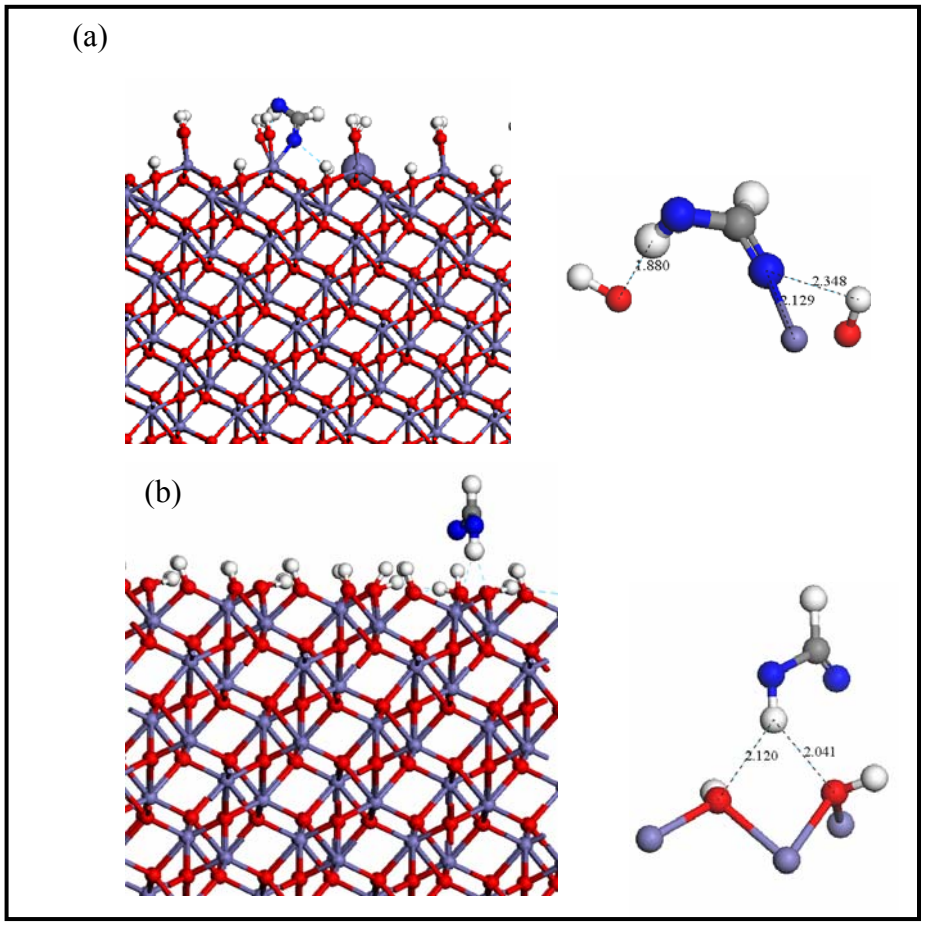

Figure 5.13: Geometry-optimised structures of two low-energy surface/adsorbate structures of methanoic acid adsorbed at the hydroxylated hematite {0001} surfaces.(a) Iron-terminated and (b) Oxygen-terminated , showing interatomic distances (Å) between the adsorbate and surface species. Key: (Iron = blue, Oxygen (surface) = red, Oxygen (hydroxyethanal) = dark blue, Carbon=Grey and Hydrogen = White).

Also, we have found in very few cases, the methanoic acid is capable of competing with dissociative water molecules for surface adsorption sites, at least on the major $\{01\bar{1}2\}a$ surface. In the lowest-energy configuration, the surface with coadsorbed methanoic acid and dissociative water molecules release an adsorption energy of -117.8 $kJmol^{-1}$. Upon relaxation, the methanoic acid replaced two

dissociated water molecules, taking the actual position of one of them whereas the second forms a bridge with the neighbouring surface iron atom, as displayed in **Figure 5.14**, where the methanoic acid coordinates to one iron surface atom via the carbonyl oxygen atom at a distance of 2.24 Å, whereas its hydroxyl hydrogen atom interacts with two oxygen surface atoms to form weak hydrogen-bonding interactions at distances of 2.05 Å and 2.10 Å.

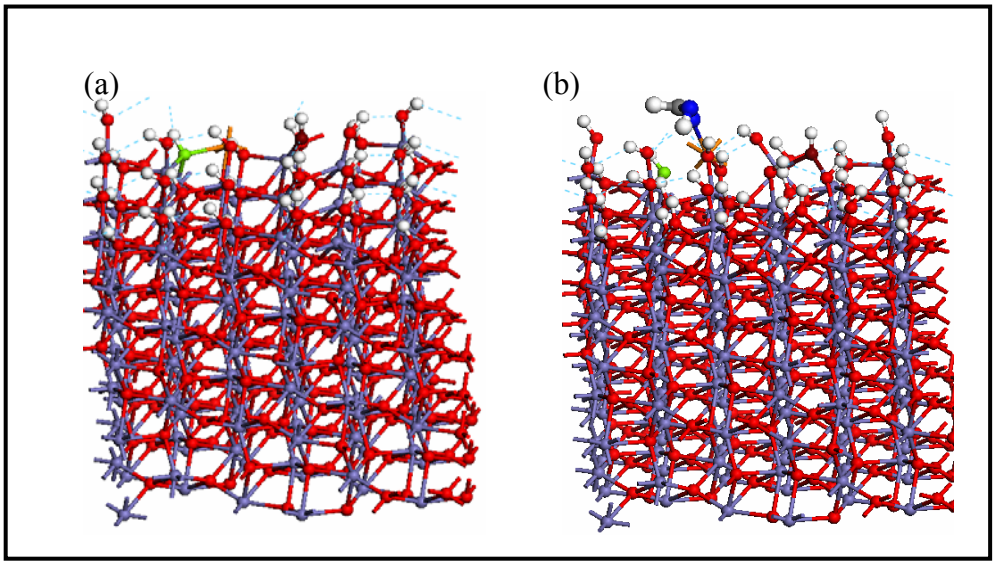

Figure 5.14: Geometry-optimised structure of the lowest-energy configuration of methanoic acid adsorbed at the hematite $\{01\bar{1}2\}_a$ surfaces showing the surface. (a) surface as purely hydroxylated and (b) surface after adsorption of methanoic acid molecule, showing interatomic distances. Key: (Fe = blue, Oxygen= red, Oxygen from organic = dark blue, Carbon=Grey and Hydrogen = White).The dark red is the hydroxyl group that forms a bond with the neighbouring iron atom on the surface. The orange is the iron atom when the carbonyl oxygen atom coordinates to the surface taking the place of the light green oxygen atom position.

5.4.4 Adsorption of Hydroxyethanal at the Hydroxylated Surfaces

On the {0001}Fe surface hydroxyethanal was able to form many favourable interactions with the surface. In particular the carbonyl oxygen atoms of the hydroxyethanal are adsorbed at the surface, where the iron atom is under-coordinated and that leads to increase the coordination of the Fe atom. Also, hydrogen-bonding interactions occur between the hydroxylated surface species and the oxygen atoms of one or both functional groups of hydroxyethanal.

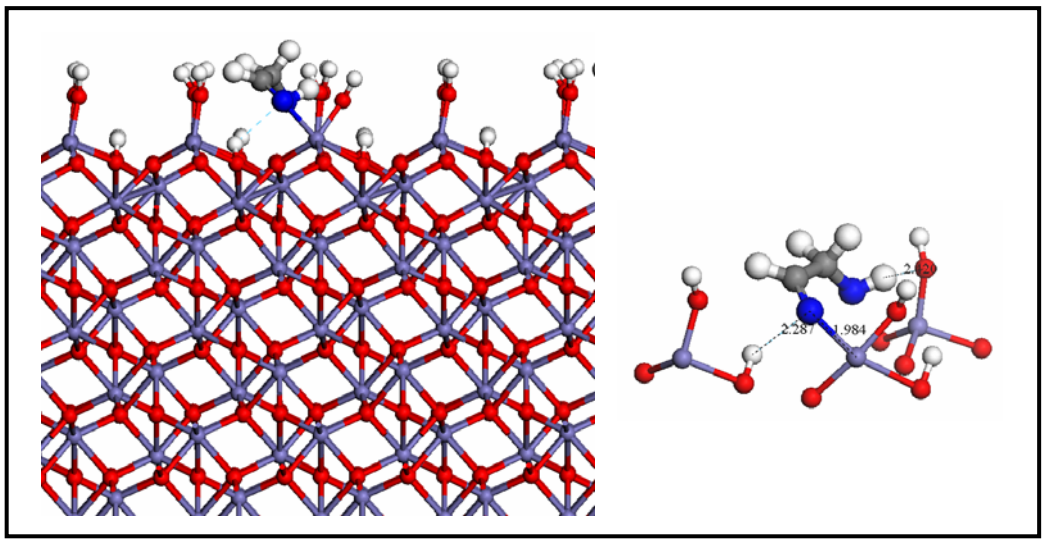

Figure 5.15: Geometry-optimised structures of the lowest-energy surface/adsorbate structures of hydroxyethanal adsorbed at the hydroxylated hematite {0001}Fe surface, showing interatomic distances (Å) between the adsorbate and surface species. Key: (Iron = blue, Oxygen (surface) = red, Oxygen (hydroxyethanal) = dark blue, Carbon=Grey and Hydrogen = White).

5.4.5 Adsorption Energies

When we compare the adsorption energies for methanoic acid with those for hydroxyethanal (**Table 5.1**), we see that in general, the energies released by adsorption of hydroxyethanal to all the dehydrated hematite (α-Fe_2O_3) surfaces are larger than for methanoic acid. The differences in binding strengths and modes of adsorption between the methanoic acid and hydroxyethanal is most likely due to the presence of the extra carbon and hydrogen atoms, which increase the interactions to the surface, whereas, the presence of =O and –OH groups in both methanoic acid and hydroxyethanal generally cause strong adsorption.

The energies listed in **Table 5.1** also show that the adsorption of hydroxyethanal is more favourable at the dehydrated $\{11\bar{2}1\}b$ surface than all other hematite surfaces, similar to the methanoic acid. The reason for that is due to the relatively unstable nature of this surface.

Our results also show that the adsorption by methanoic acid and hydroxyethanal at all hydroxylated surfaces, is less energetically favourable than onto the dehydrated surfaces, probably due to the shielding of the reactive surface ions by the hydroxy groups- Fe has a higher charge than H- and the more stable and hence less reactive nature of the hydroxylated surfaces, compared to the dehydrated surfaces.

5.5 Adsorption to Maghemite

We next investigate the adsorption of methanoic acid and hydroxyethanal with the most stable dehydrated and hydroxylated maghemite surfaces and the most exothermic adsorption energies are listed for each surfactant to each maghemite surface in **Table 5.2**.

Table 5.2: Calculated adsorption energies ($kJmol^{-1}$) for methanoic acid and two conformers of hydroxyethanal at relaxed dehydrated and hydroxylated maghemite surfaces.

Surface	**Adsorption energy($kJmol^{-1}$)**					
	Methanoic acid		**Hydroxyethanal**		**Hydroxyethanal**	
			Staggered	**Eclipsed**	**Staggered**	**Eclipsed**
	dry	**hydroxylated**	**dry**		**hydroxylated**	
{001}c	-191.7	-42.6	-218.5	-254.1	-89.1	-89.3
{010}a	-137.9	-45.8	-170.6	-195.2	-58.6	-89.0
{110}a	-150.1	-50.3	-186.9	-218.2	-59.2	-79.2
{113}a	-191.2	-83.2	-185.1	-258.3	-80.9	-92.8
{103}a	-198.3	-54.7	-256.9	-292.0	-74.9	-89.4

5.5.1 Adsorption of Methanoic acid at the Dehydrated Surfaces

As with hematite, our simulations show that, on most dehydrated maghemite surfaces, the methanoic acid prefers to adsorb onto the surface by coordinating

one surface iron atom at a bond distance ranging from 1.86 to 2.20 Å. This kind of interaction is seen on the following surfaces: {001}c,{010}a, {110}a, and {113}a.

In the lowest-energy configuration, methanoic acid molecule adsorbs at the {001}c surface with a relatively large adsorption energy of -191.7 $kJmol^{-1}$, due to the instability of this surface. The molecule coordinates to only one surface iron atom, via its carbonyl oxygen atom at a bond distance of 1.88 Å. In addition, the surface has been stabilised by hydrogen-bonding interactions between the hydroxyl hydrogen atom, which is located almost equidistant to two surface oxygen atoms at distances of between 1.75 Å and 2.49 Å.

In a different configuration (**Figure 5.16**(**b**)), again the molecule adsorbs to the surface in the same way, but in this configuration, the hydroxyl hydrogen atom of methanoic acid can interact only with one surface oxygen atom at a distance of ($O_{surface}$ …$HO_{methanoic}$ = 1.74 Å). **Figure 5.16** shows the two lowest-energy structures for the adsorption of methanoic acid at the {001}c surface.

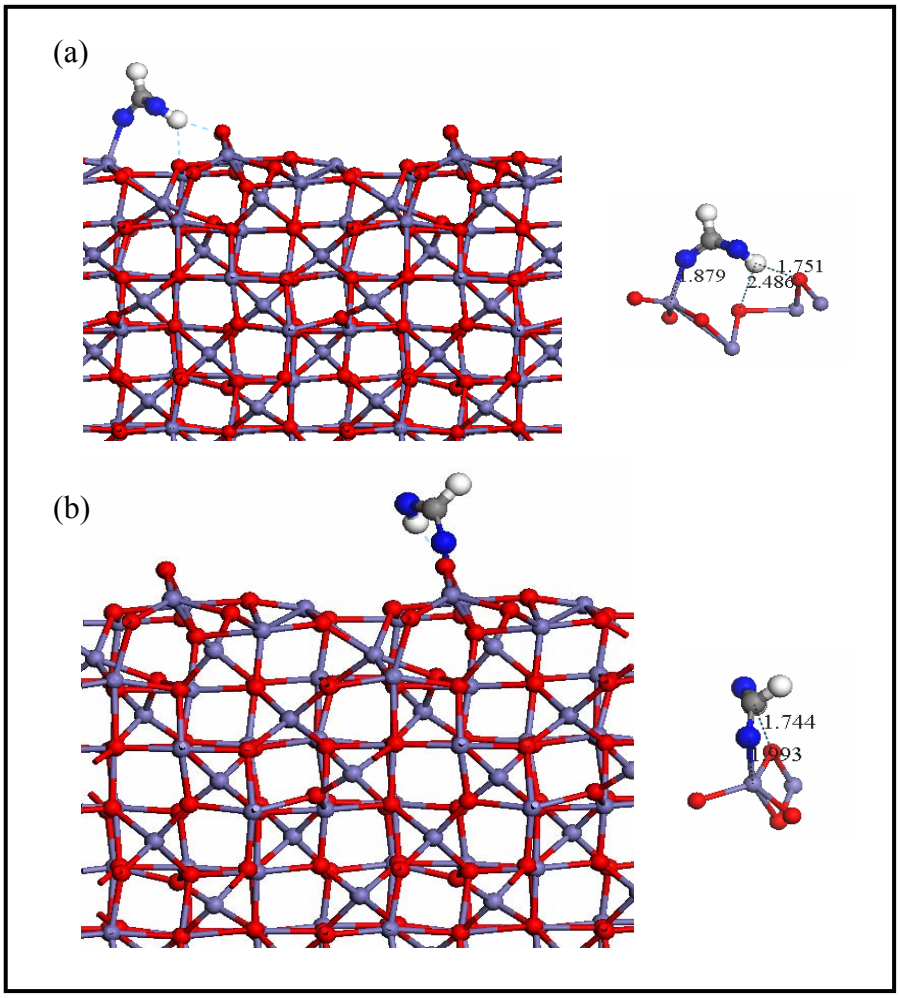

Figure 5.16: Geometry-optimised structures of the two lowest-energy surface/adsorbate structures of methanoic acid adsorbed at the dehydrated maghemite {001}c surface, showing interatomic distances (Å) between the adsorbate and surface species. Key: (Iron = blue, Oxygen (surface) = red, Oxygen (hydroxyethanal) = dark blue, Carbon=Grey and Hydrogen = White).

As we see from (**Figure 5.16**(**a**) **and** (**b**)), the carbonyl oxygen atom of methanoic acid coordinates to different iron surface atoms; in the lowest-energy configuration it binds to a three-coordinated Fe, whereas in the second configuration, the Fe is in four-coordination.

According to the calculated adsorption energies listed in **Table 5.2** the adsorption of methanoic acid to the dominant {010}a surface is the least energetically favourable at -137.9 kJmol^{-1}, compared with all other dehydrated maghemite surfaces. In the lowest-energy configuration, the molecule is almost flat on the surface, where it coordinates to one surface iron atom at a distance of 1.93Å, which is close to the Fe-O distance in the bulk mineral. In addition, the hydroxyl oxygen atom of the molecule interacts with one surface oxygen atom at a distance of 1.81Å.

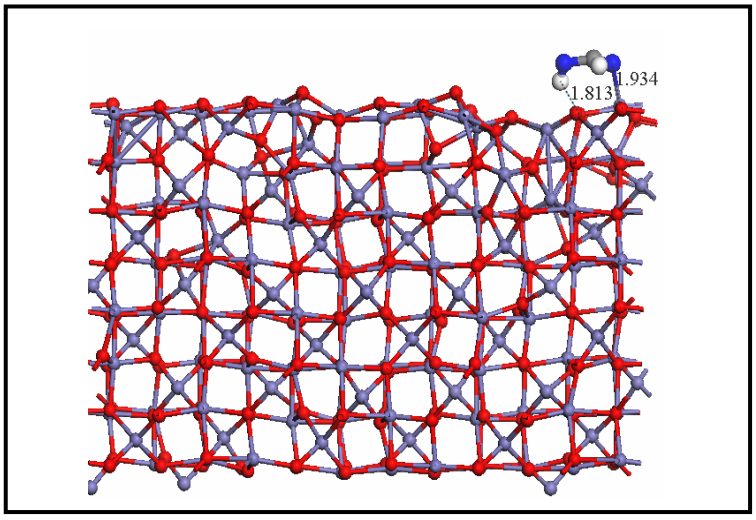

Figure 5.17: Geometry-optimised structure of the lowest-energy surface/adsorbate structure of methanoic acid adsorbed at the dehydrated maghemite {010}a surface, showing interatomic distances (Å) between the adsorbate and surface species. Key: (Iron = blue, Oxygen (surface) = red, Oxygen (hydroxyethanal) = dark blue, Carbon=Grey and Hydrogen = White).

The {103}a surface is the least stable surface compared with the other dehydrated maghemite surfaces , which therefore as expected is reactive towards adsorption of the methanoic acid molecule, releasing an adsorption energy of -198.3 kJmol^{-1}. In the lowest-energy optimised structure (**Figure 5.18**), the molecule adsorbs to

the surface by bridging between two surface iron atoms via its carbonyl oxygen and hydroxyl oxygen atoms at distances of 1.90 Å and 2.20 Å, respectively. In addition, the hydroxyl hydrogen of the methanoic acid molecule prefers to interact with two surface oxygen atoms through hydrogen-bonding interactions at distances of between 1.91 Å and 2.18 Å.

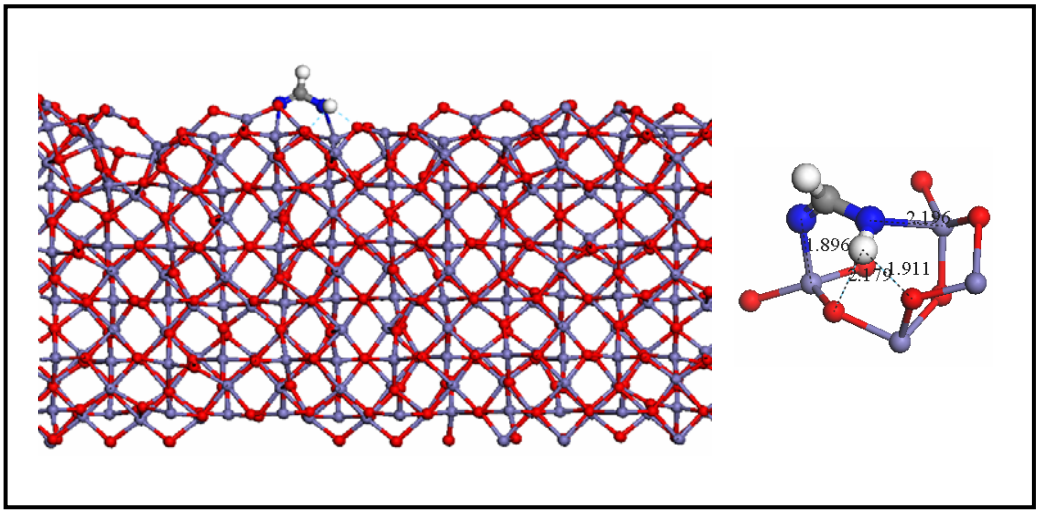

Figure 5.18: Geometry-optimised structure of the lowest-energy surface/adsorbate structure of methanoic acid adsorbed at the dehydrated maghemite {103}a surface, showing interatomic distances (Å) between the adsorbate and surface species. Key: (Iron = blue, Oxygen (surface) = red, Oxygen (hydroxyethanal) = dark blue, Carbon=Grey and Hydrogen = White).

In summary, our results show that the methanoic acid strongly binds to all dehydrated maghemite surfaces, releasing energies between approximately 137 and 198 $kJmol^{-1}$. The adsorbate binds more strongly to the {103}a surface than all other dehydrated maghemite surfaces, because this surface is the least stable surface before adsorption, and as a result is reactive towards adsorbates to increase the coordination of the surface species. As a result, of the many

interactions between methanoic acid and this surface, large energies are released upon adsorption.

As in the dehydrated hematite surfaces, the most favourable mode of the interaction between the maghemite surfaces and methanoic acid molecule occurred via its carbonyl oxygen atom, interacting with only one surface iron atom, whereas weaker interactions are found in the hydrogen-bonding interactions between the surface oxygen atoms and hydroxyl hydrogen atom of methanoic acid.

5.5.2 Adsorption of Hydroxyethanal at the Dehydrated Surfaces

In the investigation of the adsorption of hydroxyethanal to the maghemite surfaces, we have found that the most favourable mode of the interaction occurred where the molecule adsorbs to the surface by bridging between two surface iron atoms. This kind of the interaction is seen on the {001}c, {110}a, and {103}a surfaces. Also, our results (**Table 5.2**) show that on all dehydrated maghemite surfaces, adsorption of hydroxyethanal in an eclipsed conformation is energetically preferred over a staggered conformation.

On the{001}c surface, both conformers of hydroxyethanal adsorb to the surface in a similar way by bridging two surface iron atoms, releasing relatively large adsorption energies of -218.5 $kJmol^{-1}$ and 254.1 $kJmol^{-1}$ for the initially staggered and eclipsed hydroxyethanal, respectively. The main difference in the two

configurations is the distance between the surface species and coordinating site of the adsorbate molecule.

In one low energy configuration from the eclipsed hydroxyethanal, the molecule coordinates to the two different surface iron atoms via its carbonyl oxygen and hydroxyl oxygen atoms at distances of 2.03 Å and 2.02 Å. At the same time, the surface has stabilised through hydrogen-bonding interactions between the hydroxyl hydrogen atom of the hydroxyethanal molecule and two surface oxygen atoms at distances between 2.01 Å-2.41 Å. In **Figure 5.19** we have shown the two lowest-energy structures of hydroxyethanal adsorbed at the {001}c surface.

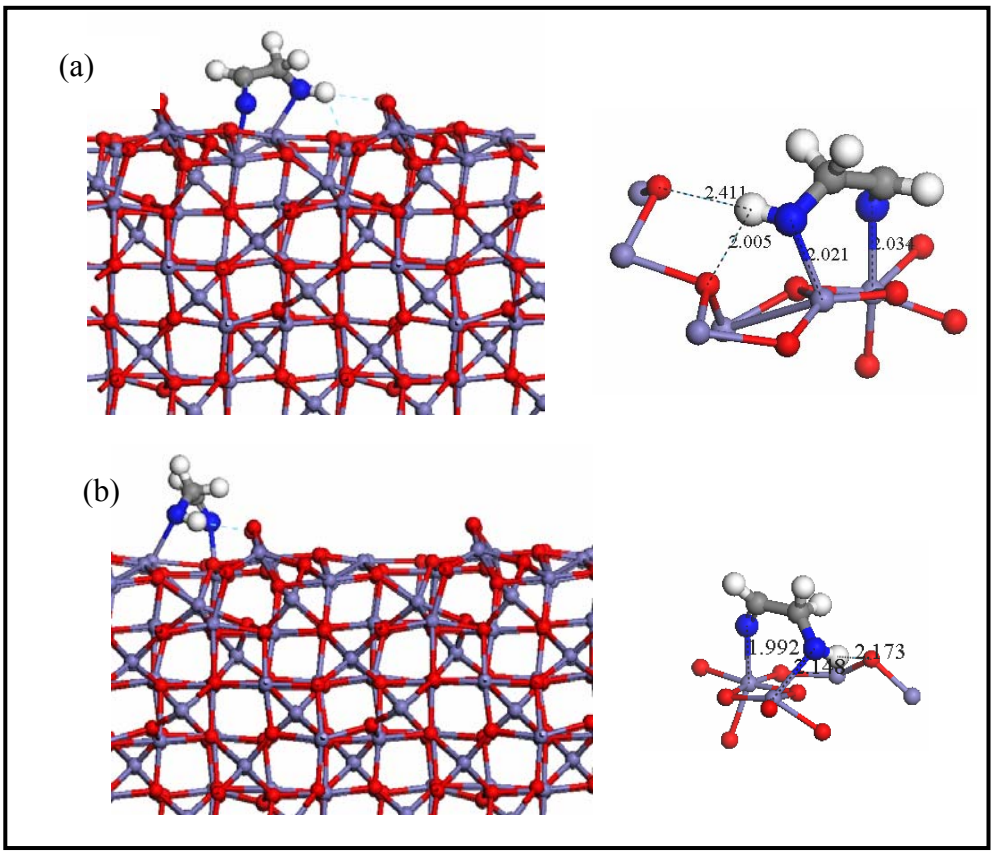

Figure 5.19: Geometry-optimised structures of the lowest-energy surface/adsorbate structures of hydroxyethanal adsorbed at the dehydrated maghemite {001}c surface, showing interatomic distances (Å) between the adsorbate and surface species. Key: (Iron = blue, Oxygen (surface) = red, Oxygen (hydroxyethanal) = dark blue, Carbon=Grey and Hydrogen = White).

Our results (**Table 5.2**) show that the adsorption of hydroxyethanal is more energetically more preferred onto the {103}a surface, releasing large adsorption energies of -256.9 $kJmol^{-1}$ to -292.0 $kJmol^{-1}$ for the initially staggered and eclipsed hydroxyethanal, respectively, similar to the adsorption of methanoic acid on the dehydrated maghemite surfaces. In the lowest optimised structure (**Figure 5.20**) from the eclipsed hydroxyethanal, the molecule bridges two surface iron

atoms, coordinating strongly via its carbonyl oxygen atom to an iron atom on top of the surface at a distance of 1.86 Å, whereas the hydroxyl oxygen atom coordinates to a second iron atom below the surface oxygen atoms at a distance of 2.02 Å. The adsorption is stabilised by further interactions where the hydroxyl hydrogen atom of the molecule is interacting with two surface oxygen atoms to form weak hydrogen-bonds at distances between 2.40 Å -2.48 Å.

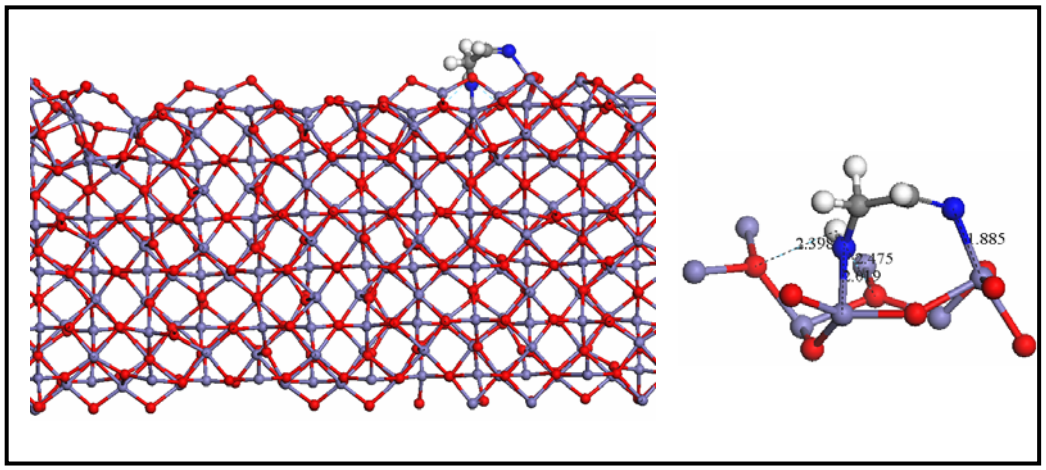

Figure 5.20: Geometry-optimised structure of the lowest-energy surface/adsorbate structure of hydroxyethanal adsorbed at the dehydrated maghemite {103}a surface, showing interatomic distances (Å) between the adsorbate and surface species. Key: (Iron = blue, Oxygen (surface) = red, Oxygen (hydroxyethanal) = dark blue, Carbon=Grey and Hydrogen = White).

The other favourable mode of the adsorption of hydroxyethanal with dehydrated maghemite surfaces is by coordinating to one surface iron atom which can be seen on both {010}a and {113}a surfaces.

Both conformers of hydroxyethanal adsorb to the {010}a surface in similar way by coordinating to only one surface iron atom through their carbonyl oxygen atoms. The hydroxyethanal molecules adsorb, releasing relatively large energies of 170.6 $kJmol^{-1}$ and 195.2 $kJmol^{-1}$ for the lowest energy structures of the initially staggered and eclipsed hydroxyethanal respectively.

In the lowest-energy optimised structure for both eclipsed and staggered hydroxyethanal, the carbonyl oxygen atom coordinating to a surface iron atom in four-fold coordination, at bond distances of 1.87 Å and 1.93 Å for the eclipsed and staggered hydroxyethanal, respectively. The main difference in the adsorption of the hydroxyethanal conformers is in the formation of hydrogen-bonding interactions with the surface, which depend on the position of the adsorbate molecule. For example, in the lowest configuration form the eclipsed hydroxyethanal, the molecule is almost perpendicular to the surface, enabling the hydroxyl hydrogen atom to interact with two surface oxygen atoms at distances between 1.86 Å - 2.82 Å, while in the lowest configuration from the staggered hydroxyethanal, the hydroxyl group points away from the surface, and the hydroxyl hydrogen atom can therefore interact with only one surface oxygen atom at a distance of 1.80 Å. **Figure 5.21** shows the two lowest energy structures as identified from our simulations.

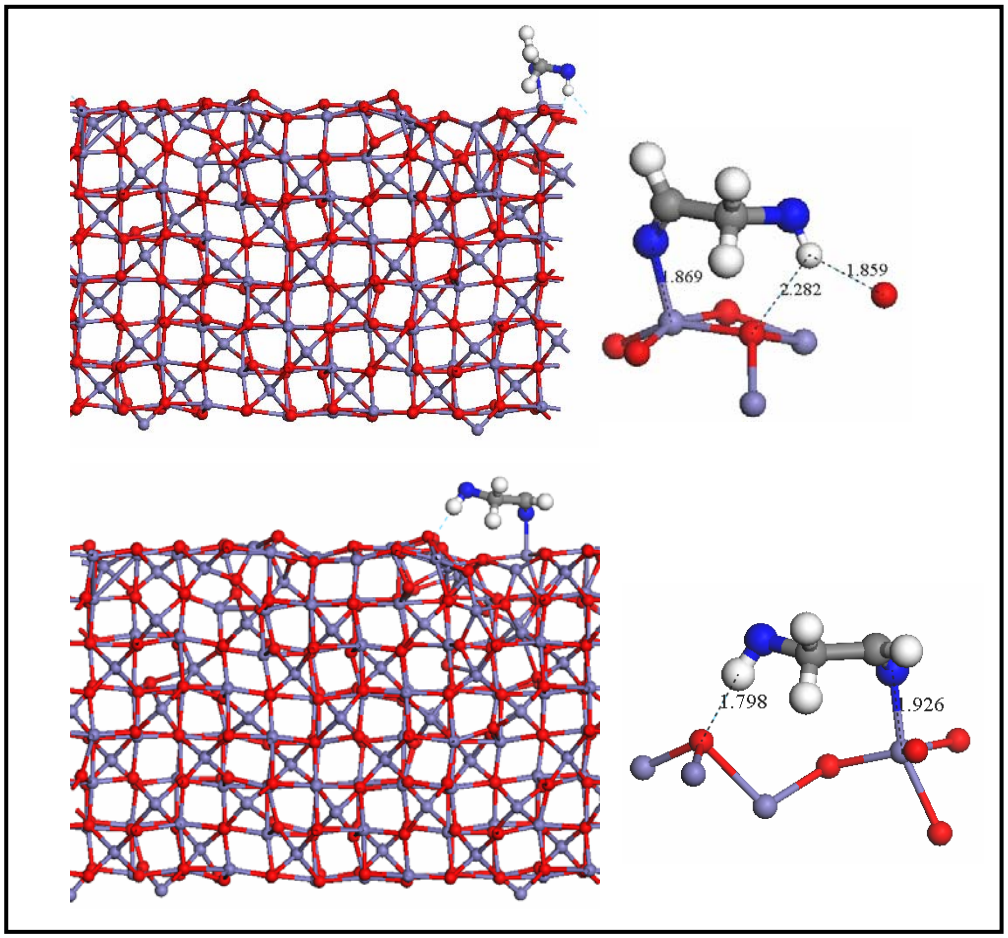

Figure 5.21: Geometry-optimised structures of the two lowest-energy surface/adsorbate structures of hydroxyethanal adsorbed at the dehydrated maghemite {010}a surface, showing interatomic distances (Å) between the adsorbate and surface species. Key: (Iron = blue, Oxygen (surface) = red, Oxygen (hydroxyethanal) = dark blue, Carbon=Grey and Hydrogen = White).

5.5.3 Adsorption of Methanoic acid at the Hydroxylated Surfaces

Finally, we have investigated the adsorption of both methanoic acid and hydroxyethanal onto the hydroxylated maghemite surfaces. On most hydroxylated surfaces the calculated adsorption energies (**Table 5.2**) are slightly more negative than the calculated hydration energies (**Table 4.3**, **Chapter 4**), including the {010}a, {110}a, {113}a, and {103}a surfaces.

The hydroxylated maghemite {113}a surface is the most reactive toward methanoic acid releasing an adsorption energy of 83.2 $kJmol^{-1}$, because the adsorbed methanoic acid molecule on the maghemite {113}a surface is in the best position to interact with the preadsorbed dissociative water molecules. Because the methanoic acid is a bigger molecule than water, it is able to interact with the rows of dissociated water molecules both to the left and to the right. The hydroxyl hydrogen atom of the methanoic acid molecule forms hydrogen bonds to two oxygen atoms of surrounding hydroxy groups at distances of 1.96 Å and 2.32 Å, whereas the carbonyl oxygen atom interacts with only one surface iron atom at a distance of 2.14 Å.

Conversely, introduction of methanoic acid onto the hydroxylated {001}c maghemite surface releases an adsorption energy of only 42.6 $kJmol^{-1}$, which is less negative than the calculated hydration energy -88.7 $kJmol^{-1}$ due to the stability of this surface. In the lowest-energy configuration, the methanoic acid molecule has few significant interactions with the surrounding hydroxy groups

where the carbonyl oxygen atom of the adsorbate molecule interacts with two surface hydrogen atoms at distances between 2.35 Å - 2.49 Å, and the hydroxyl hydrogen atom forms another hydrogen-bond with only one surface oxygen atom at a distance of 1.90 Å, while in this position the hydroxyl oxygen atom of methanoic acid points away from the surface.

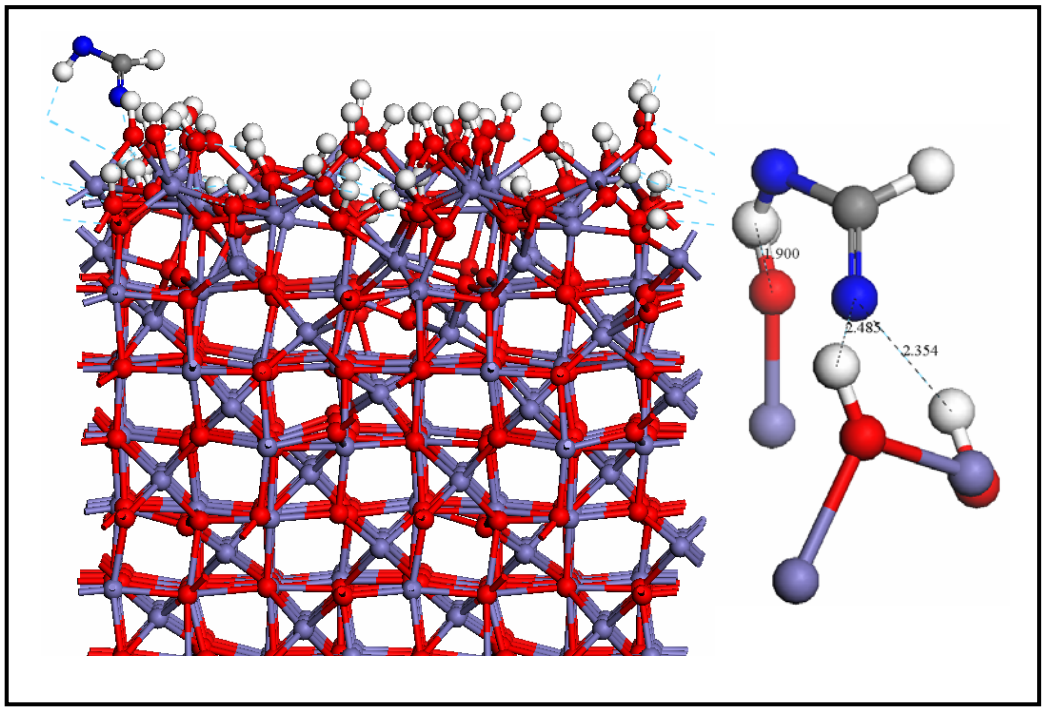

Figure 5.22: Geometry-optimised structure of the lowest-energy surface/adsorbate structure of methanoic acid adsorbed at the hydroxylated maghemite {001}c surface, showing interatomic distances (Å) between the adsorbate and surface species. Key: (Iron = blue, Oxygen (surface) = red, Oxygen (hydroxyethanal) = dark blue, Carbon=Grey and Hydrogen = White)**.**

5.5.4 Adsorption of Hydroxyethanal at the Hydroxylated Surfaces

In general, our results suggest that the adsorption of hydroxyethanal onto all hydroxylated maghemite surfaces is stronger. As on the dry surface, the adsorption of the hydroxyethanal on the surface would be preferred in an eclipsed fashion.

In the lowest energy positions from each eclipsed and staggered hydroxyethanal, both conformers adsorb to the {001}c surface in a similar mode, by coordinating to one surface iron atom via their carbonyl oxygen atoms. Upon relaxation, the molecule was almost perpendicular to the surface, coordinating to one surface iron atom via its carbonyl oxygen atom at a distance of 2.16 Å. In addition, the hydroxyl oxygen atom of the molecule interacts more weakly to one hydrogen atom of surrounding hydroxy groups at a distance of 2.46 Å.

Again, the adsorption of hydroxyethanal onto the hydroxylated {113}a surface is energetically more favourable than the other surfaces. In the lowest-energy configuration, the hydroxyl hydrogen atom of the hydroxyethanal molecule forms a hydrogen-bond to one oxygen atom of the surrounding hydroxy groups at a distance of 1.96 Å, while the carbonyl oxygen atom forms a weak hydrogen-bond with one hydrogen atom of the surrounding hydroxy groups at a distance of 2.50 Å.

5.5.5 Adsorption Energies

The calculated adsorption energies for the adsorption of both organic molecules on the different maghemite surfaces are all negative. As with hematite, we see that the adsorption of hydroxyethanal to all dehydrated and hydroxylated maghemite (γ-Fe_2O_3) surfaces is more favourable than methanoic acid.

5.6 Discussion and Conclusions

In this chapter, we have modelled the adsorption of both methanoic acid and hydroxyethanal at important dehydrated and hydroxylated surfaces of both hematite and maghemite. These adsorbate were chosen, because they provide the opportunity to investigate the effect of separation the =O and –OH groups of the carboxylic acid by an extra carbon into separate ethanol and aldehyde functional groups, on the strength of the surface/adsorbate interaction. From our results we can make the following observation:

- Generally, adsorption of hydroxyethanal is more favourable than methanoic acid for both hematite and maghemite, either dehydrated or hydroxylated surfaces, due to the larger and more flexible O-O distance in hydroxyethanal, which better suits the large interatomic Fe-Fe distances on the hematite and maghemite surfaces. Our simulations show that the adsorption of hydroxyethanal is more favourable in the eclipsed conformer.

- By comparing the adsorption energies of methanoic acid and both the eclipsed and staggered hydroxyethanal on the two iron polymorphs hematite (α-Fe_2O_3) and maghemite (γ-Fe_2O_3), we find that maghemite is more reactive toward the adsorption of methanoic acid molecule than hematite. This maybe explained by the surface energies, where most of the maghemite surfaces are less stable than the dry hematite surfaces, and therefore will be more reactive.
- The hydroxylation of the surfaces of both iron oxide minerals made the adsorption of the two organic molecules much less favourable than those at the dehydrated surfaces, caused by the stabilisation of the hydroxylated surfaces compared to the dehydrated surfaces and the shielding of the surface by the hydroxy groups and in particular the hydrogen atoms.
- The adsorption of methanoic acid also have investigated on other material, for example, Cooper and de Leeuw (2002) have studied the adsorption of methanoic acid on both calcite and aragonite surfaces, and have shown that the methanoic acid molecule coordinate bridging two surface calcium atoms, strongly via their carbonyl oxygen atoms and weakly via their hydroxyl oxygen atoms on the Calcite surfaces, also sometimes the methanoic acid adsorbed onto the surface through only the carbonyl oxygen atom, which coordinate to only one surface calcium atoms, and that what have found in our simulation results for using the same molecule.
- In the next chapter, we will present our calculations of the adsorption of arsenate at the same dehydrated and hydroxylated hematite and maghemite surfaces.

Chapter 6

Adsorption of Arsenate at Hematite (α-Fe_2O_3) and Maghemite (γ-Fe_2O_3) Surfaces

Abstract

In the previous chapter, we have employed atomistic simulations to determine the modes and strength of binding of methanoic acid and hydroxyethanal as model organic pollutants to the surfaces of hematite and maghemite. In this chapter, we present the interaction between the same surfaces considered in **Chapter 5** with the arsenate molecule (H_3AsO_4), where the adsorption is studied again at both dehydrated and hydroxylated surfaces.

6.1 Introduction

Arsenic has received a great deal of public attention because its high levels in some water supplies have led to major health problems as it causes certain kinds of cancers (Hopenhayn, 2006). The arsenic contamination in shallow tubewell waters in excess of the acceptable limit is affecting the health of the people in many countries for example, Bangladesh and West Bengal in India. In both these countries thousands of people have already shown the symptoms of arsenic

poisoning, but there are millions still at risk because of the widespread use of the drinking water direct from these tubewells. Therefore, it is clearly important to remove arsenic from groundwater for which a number of strategies have been proposed. The most commonly used methods are co-precipitation, oxidation, ion exchange, or adsorption on mineral surfaces. The concentration of arsenate in natural water is strongly influenced by adsorption on oxide surfaces (Fuller & Davis, 1989; Vitre *et al*., 1991; Azcue & Nriagu, 1993; Pichler & Veizer, 1999; Fukushi *et al*., 2003; Linge & Oldham, 2004), and one of the common methods which has been suggested for the removal of arsenic is the filtration method (Katsoyiannis & Zouboulis, 2002; Thirunavukkarasu *et al*., 2003; Garelick *et al*., 20005 Jessen *et al*., 2005), which depends on its adsorption onto iron oxides surfaces. Therefore, in this chapter we focus on the adsorption of arsenate on the hematite (α-Fe_2O_3) and maghemite (γ-Fe_2O_3) surfaces.

6.2 Adsorbate Molecule

The Arsenate molecule ($H_nAsO_4^{3-n}$) is used to study the adsorption of arsenic compounds on the hematite and maghemite surfaces, and the calculated adsorption energies will provide us information about the strength of interaction between the mineral surfaces and the adsorbate molecule.

Arsenate is a tetrahedral molecule with one As=O double bond (**Figure 6.1)**. All hydroxyl oxygen atoms of the arsenate are assigned the same partial charge of -1.4 eV, with a charge of -2.0 eV for the double-bonded oxygen. The double bonded oxygen atom is the more accessible to coordinate to the surface and in

most case arsenate coordinates to the surface through this atom, although this does not mean that the hydroxyl oxygen atoms cannot coordinate to the surface. Sometimes the arsenate molecule coordinates to the surface through both types of oxygen atoms depending on the nature of the surface.

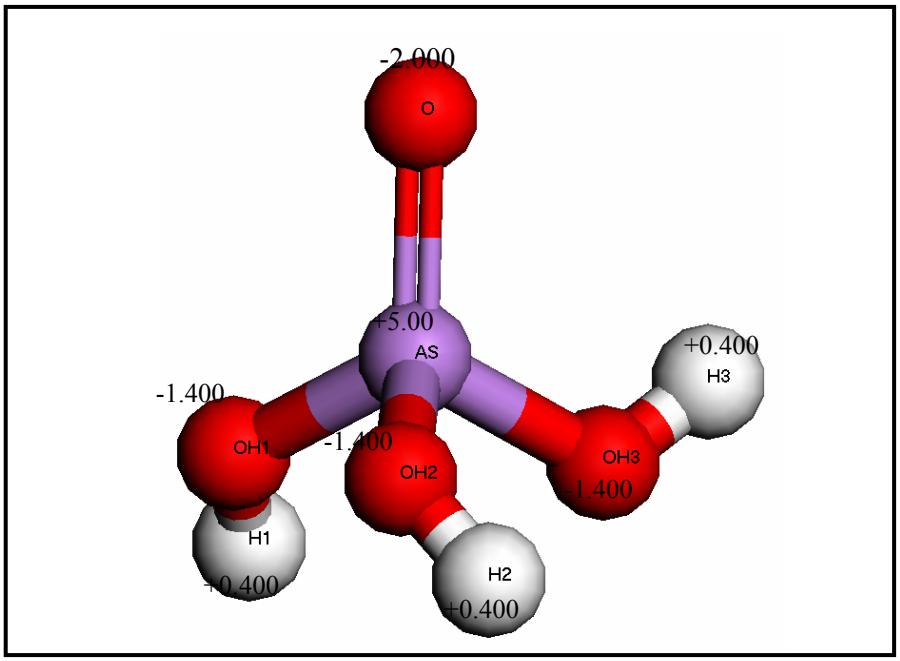

Figure 6.1: The arsenate molecule, showing the charges on the atoms. Key: (Arsenate =purple, Oxygen=red and the hydrogen =White).

6.3 Adsorption to Hematite

6.3.1 Dehydrated Surfaces

Table 6.1: Calculated adsorption energies ($kJmol^{-1}$) for the arsenate molecule at relaxed dehydrated and hydroxylated hematite surfaces.

Surfaces	Adsorption energy($kJmol^{-1}$)	
	Dehydrated	Hydroxylated
$\{0001\}$Fe	-313.2	-31.3
$\{0001\}$Ox	-482.1	-62.8
$\{10\bar{1}0\}$a	-323.6	-173.4
$\{10\bar{1}1\}$a	-673.7	-49.7
$\{11\bar{2}0\}$a	-364.3	-176.4
$\{01\bar{1}2\}$a	-314.5	-109.4
$\{11\bar{2}1\}$b	-328.0	-129.6

We first investigate the interaction of the arsenate with the dehydrated hematite and maghemite surfaces. In general, the most favourable mode of adsorption of the arsenate molecule on most dehydrated hematite (α-Fe_2O_3) surfaces is through bridging by the As between two surface oxygen atom, whereas the doubly-bonded oxygen and one of the hydroxyl oxygen atoms coordinate to one surface iron atom each. This kind of configuration is seen on both the iron- and oxygen-terminations of the {0001} plane. On the Fe-terminated {0001} surface, the As is coordinated to two surface oxygen atoms at distances of between 1.77 Å and 1.79 Å, with the doubly bonded oxygen atom coordinated to one surface iron atom at a distance of 1.94 Å, whereas two hydroxyl oxygen atoms are coordinated to two surface iron atoms at distances of between 2.13 Å and 2.10 Å. According to the calculated adsorption energies, listed in **Table 6.1**, the adsorption of the

arsenate to the Fe-terminated {0001} surface is strong but less energetically than to the Ox-terminated plane (-313.2 $kJmol^{-1}$), (-482.1 $kJmol^{-1}$), which is less stable and hence more reactive. However, this surface was less reactive towards other effects, so we expect that such as surface geometry also play a role. **Figure 6.2** shows the lowest energy positions for adsorption of the arsenate molecule on both Fe-termination and Ox-termination of the {0001} surface.

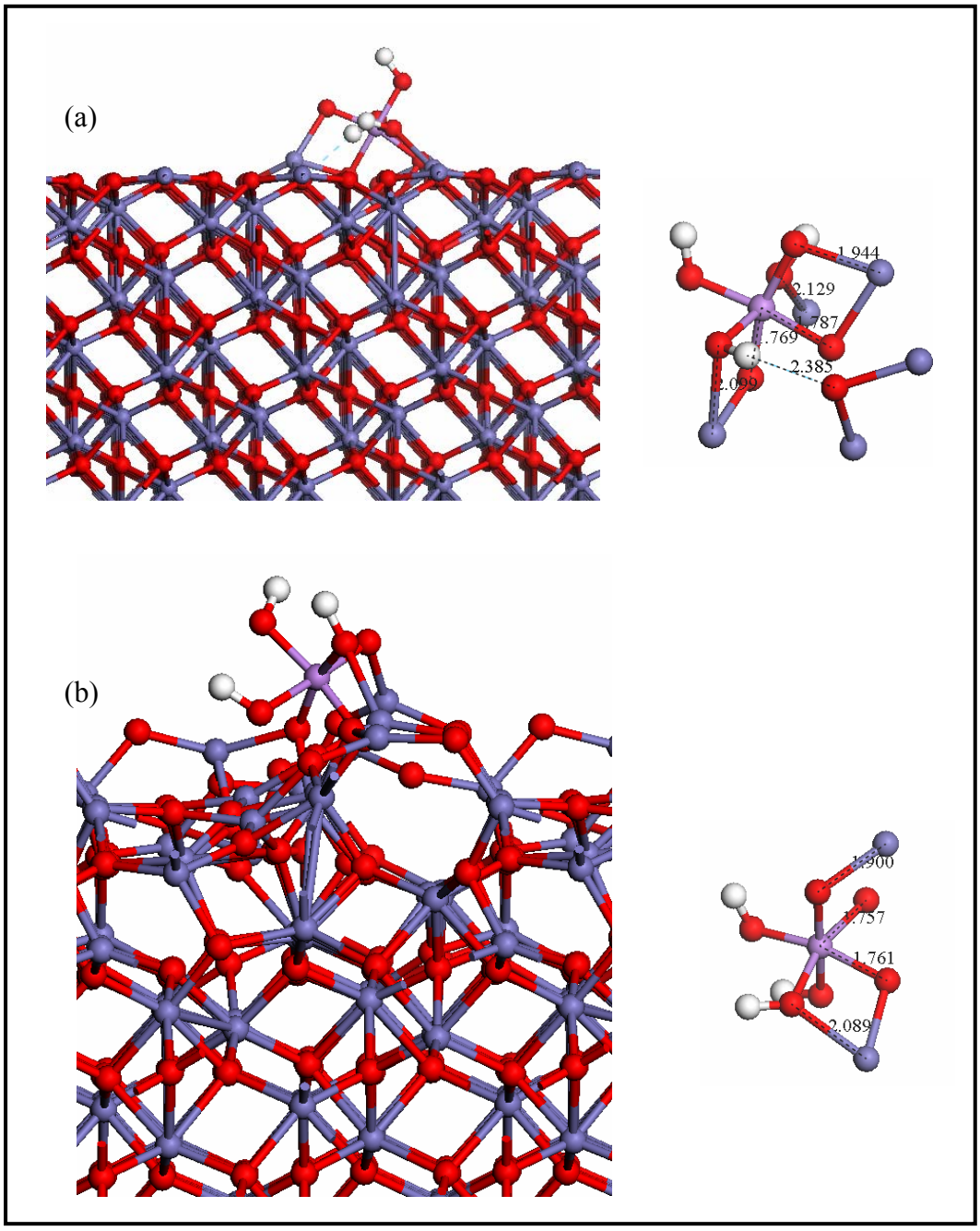

Figure 6.2: Lowest-energy optimised structures of arsenate adsorbed at the dehydrated hematite {0001} surface. (a) Fe-terminated and (b) oxygen-terminated, showing interatomic distances (Å) between the adsorbate and surface species. Key: (Iron = blue, Oxygen = red, Arsenate = purple, and the Hydrogen = White).

Sometimes the spacing between the surface iron atoms is not too large, which allows to the doubly-bonded oxygen atom of arsenate to bridge between two iron atoms. For example, on the $\{11\bar{2}0\}a$ surface, as shown in **Figure 6.3**, the doubly-bonded oxygen atom of the arsenate bridges between two surface iron atoms at distances of 1.98 Å and 2.14 Å, whereas the hydroxyl oxygen atom coordinates to another iron atom in the layer below at a distance of 2.22 Å, and As again bridges between two surface oxygen atoms at distances of 1.76 Å and 1.77 Å, releasing an adsorption energy of -364.3 $kJmol^{-1}$.

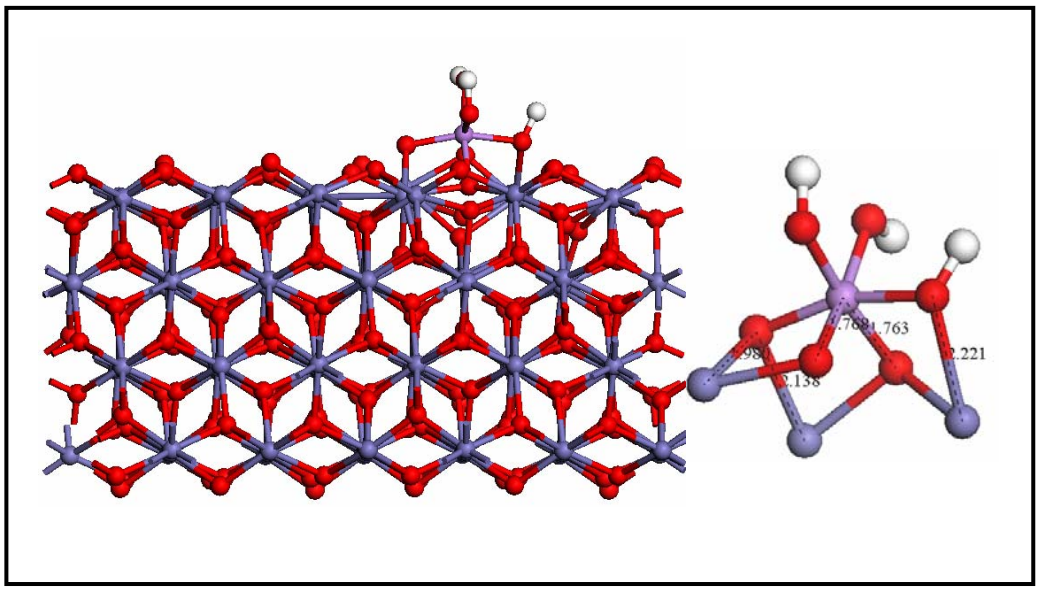

Figure 6.3: Lowest-energy optimised structure of arsenate adsorbed at the dehydrated hematite $\{11\bar{2}0\}a$ surface, with the double-bonded oxygen of arsenate bridging two surface iron atoms, showing interatomic distances (Å) between the adsorbate and surface species. Key: (Iron = blue, Oxygen = red, Arsenate = purple, and the Hydrogen = White).

On both $\{10\bar{1}0\}a$ and $\{01\bar{1}2\}a$ surfaces, the arsenate prefers to adsorb on the surface by coordinating through the As to only one surface oxygen atom, in addition to the interactions between the surface species and another oxygen or hydrogen atoms of the arsenate. In **Figure 6.4** we have shown the lowest -energy structures of arsenate adsorbed at the $\{10\bar{1}0\}a$ and $\{01\bar{1}2\}a$ surfaces respectively.

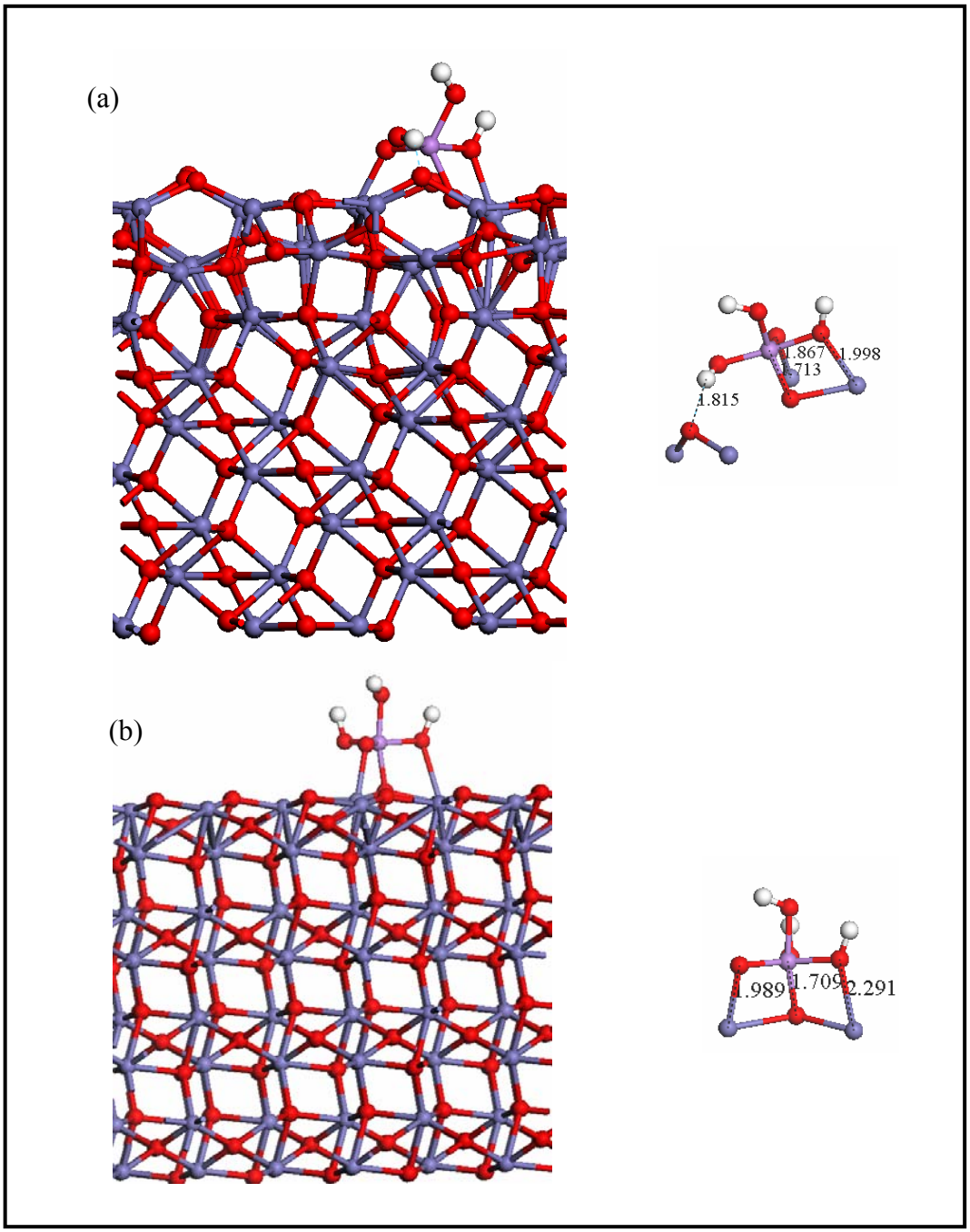

Figure 6.4: Lowest-energy optimised structures of arsenate adsorbed at the dehydrated hematite surfaces. (a) $\{10\bar{1}0\}$a surface and (b) $\{01\bar{1}2\}$a surface, showing interatomic distances (Å) between the adsorbate and surface species. Key: (Iron = blue, Oxygen = red, Arsenate = purple , and the Hydrogen = White).

The energy released upon adsorption of arsenate on the $\{10\bar{1}1\}a$ surface is very high in comparison with all other dehydrated hematite surfaces, which may due to its high surface energy ($2.34Jm^{-2}$) and therefore unstable nature, as discussed before in previous chapters.

On the $\{10\bar{1}1\}a$ surface, the most favourable mode of adsorption of arsenate is shown in **Figure 6.5**. Upon the adsorption, the molecule coordinates to the surface through the As which bridges three surface oxygen atoms at bond distances ranging from 1.74 Å - 1.78 Å, whereas the doubly bonded oxygen atom of the arsenate molecule is strongly coordinated to one surface iron atom at a distance of 1.88 Å and one of the hydroxyl oxygens coordinates to an other surface iron atom at a distance of 1.93 Å. An interesting feature is that one of the hydroxyl groups of the arsenate leaves the molecule to bind to a surface iron atom (1.88 Å), leaving the As in six-coordination. **Figure 6.5** shows the two lowest-energy structures of the arsenate adsorbed at the $\{10\bar{1}1\}a$ surface.

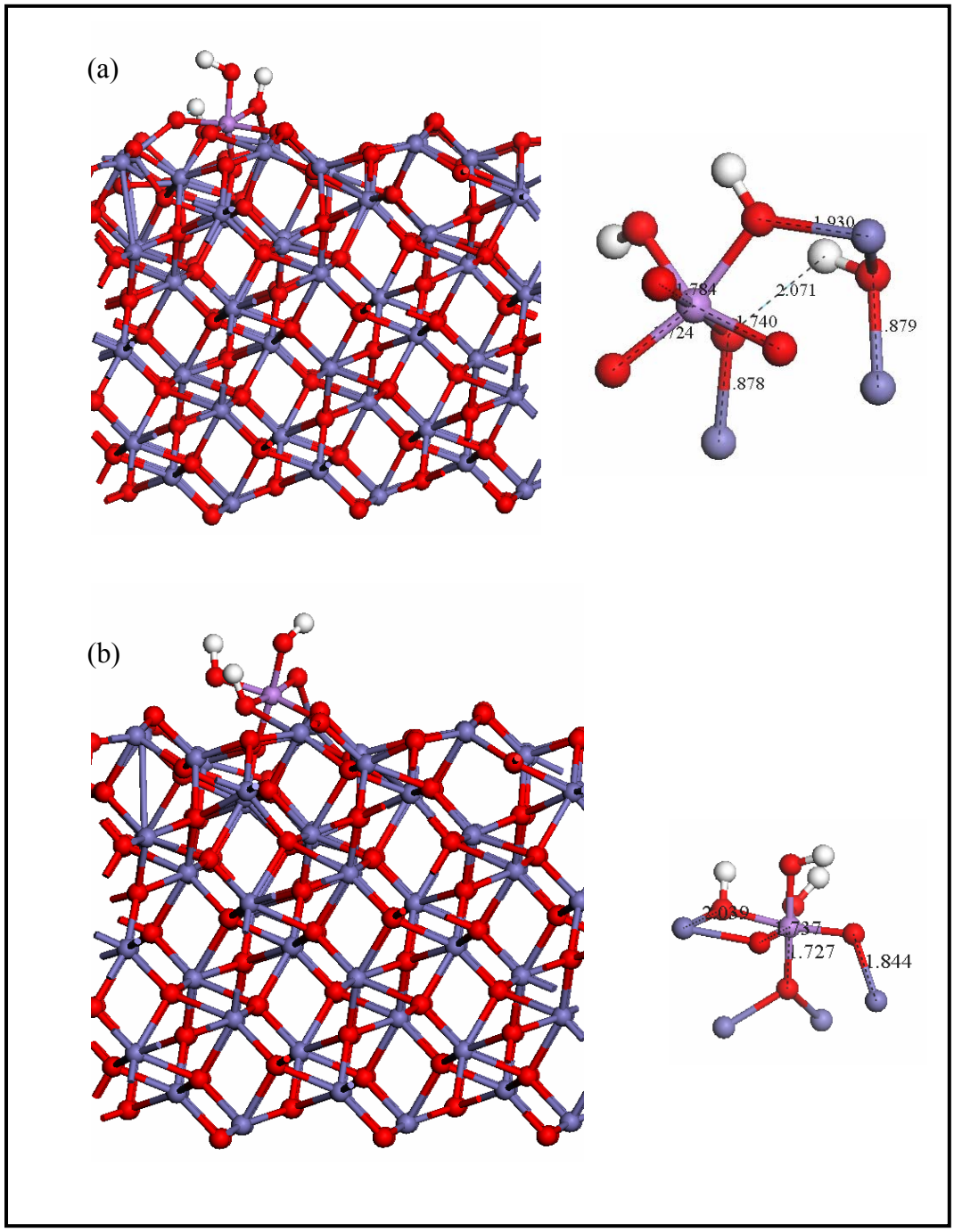

Figure 6.5: Geometry-optimised structures of the two lowest-energy configurations of arsenate adsorbed at the dehydrated hematite $\{10\bar{1}1\}$a surface, showing the interatomic distances (Å). Key :(Iron = blue, Oxygen = red, Arsenate = purple, and the Hydrogen = White).

6.3.2 Hydroxylated Surfaces

Again, we have considered the same hydroxylated hematite surfaces to investigate the influence of pre-adsorbed water on the interaction between the arsenate and the mineral.

Generally, our results suggest that addition of water through dissociative adsorption onto the surfaces significantly reduces the interaction between the surfaces and the second adsorbate molecule. In the most favourable adsorption mode, the arsenate molecule replaces one or two hydroxy groups of the dissociatively adsorbed water. The doubly-bonded oxygen of the arsenate molecule only coordinates to one surface iron atom and will replace the hydroxy group in that position. In most cases the surface is stabilised further by hydrogen-bonding interactions between the surface species and the multiple oxygen and hydrogen atoms of arsenate. For example, on the Fe-terminated {0001} surface The doubly-bonded oxygen coordinates to one surface iron atom at a distance of 1.88 Å, replacing one hydroxy group in that position. Two hydrogen atoms of other arsenate hydroxyl groups interact with the closest oxygen atom of the surrounding dissociated water molecules on the surface at distances of between 2.29 Å - 2.37 Å. At the same time the doubly-bonded oxygen forms another hydrogen bond with the hydrogen atom of a neighbouring surface hydroxy group at a distance of 1.95 Å, as shown in **Figure 6.6**.

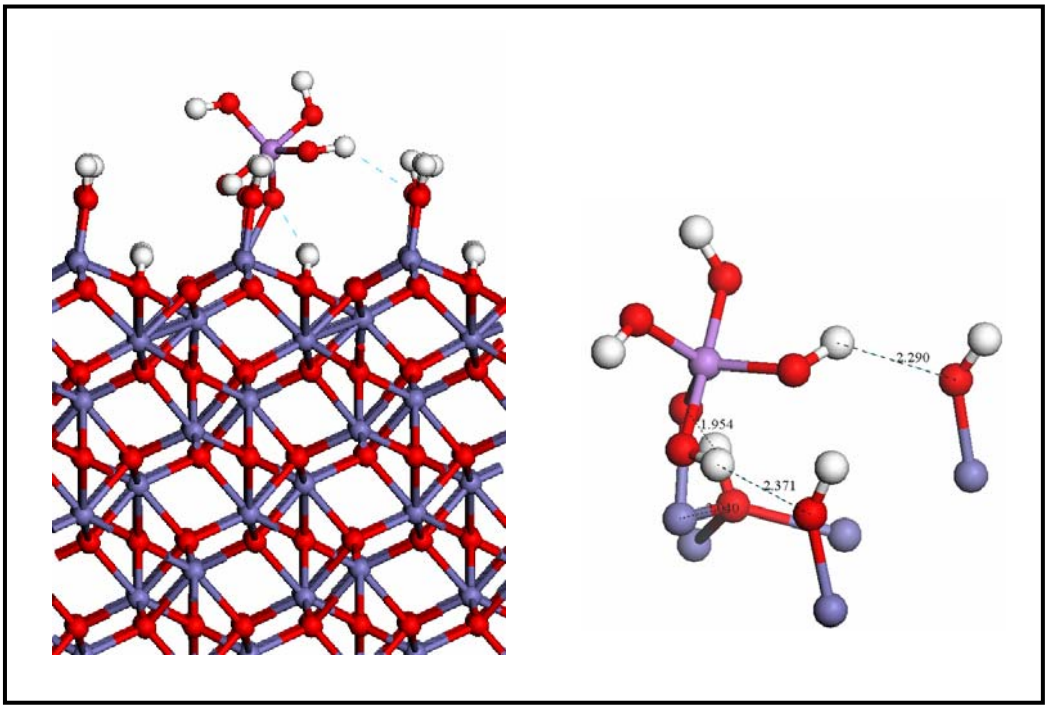

Figure 6.6: Lowest-energy optimised structures of arsenate adsorbed at the hydroxylated Fe-terminated {0001} surface, showing interatomic distances (Å) between the adsorbate and surface species. Key: (Fe = blue, Oxygen = red, Arsenate = purple, and the Hydrogen = White**).**

However, sometimes the As atom coordinates to one or two oxygen atoms of the surrounding hydroxy groups on the surface. **Figure 6.7** shows the $\{01\bar{1}2\}a$ surface, where the arsenate molecule adsorbs by replacing one hydroxy group where the doubly-bonded oxygen of arsenate binds to the surface iron atom in that position at a distance of 1.91 Å, while the As atom coordinates to one oxygen atom of a surface hydroxy group at a distance of 1.71 Å. The surface is stabilised further by hydrogen-bonding interactions between the hydroxylated surface species and the functional groups (oxygen atoms and hydrogen atoms) of the arsenate molecule.

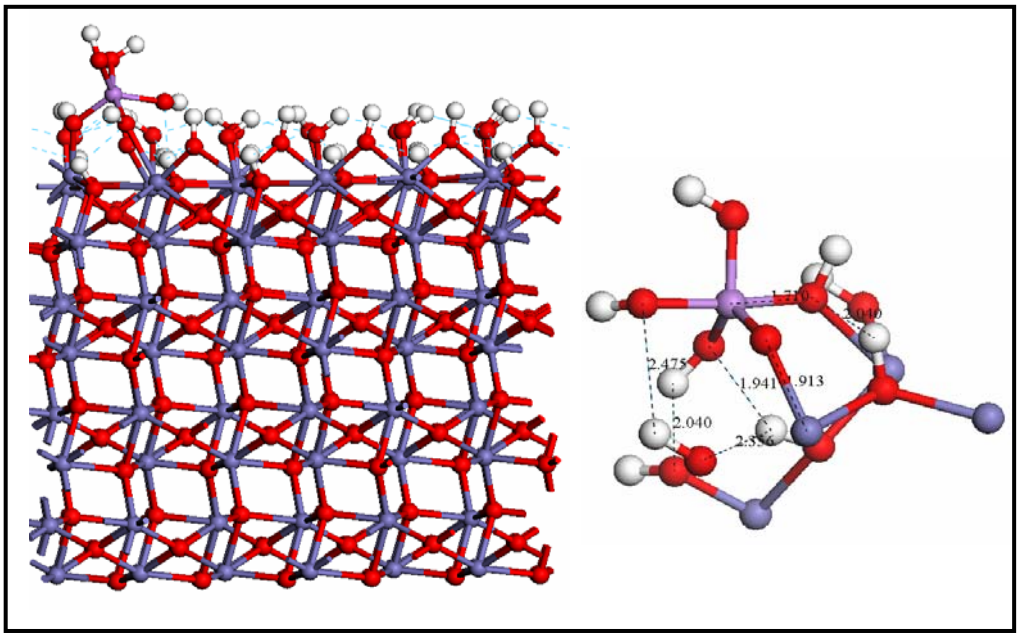

Figure 6.7: Lowest-energy optimised structures of arsenate adsorbed at the hydroxylated hematite $\{01\bar{1}2\}a$ surface, showing interatomic distances (Å) between the adsorbate and surface species. Key: (Fe = blue, Oxygen = red, Arsenate = purple, and the Hydrogen = White).

On the other hydroxylated hematite surfaces, ($\{0001\}$Ox, $\{10\bar{1}0\}a$, $\{10\bar{1}1\}a$, $\{11\bar{2}0\}a$, and $\{11\bar{2}1\}b$, the As of arsenate bridges two oxygen atoms of the surrounding hydroxy groups on the surface.

6.3.3 Adsorption Energies

The adsorption energies for the arsenate at all the dehydrated and hydroxylated hematite surfaces, listed in **Table 6.1**, have shown that the arsenate interacts strongly with the dehydrated hematite (α-Fe_2O_3) surfaces, in particular to the

$\{10\bar{1}1\}a$ surface and oxygen-terminated {0001} surface.

Both $\{10\bar{1}1\}a$ and oxygen-terminated {0001} surfaces are less stable compared to the other surfaces considered, which is due to a large number of under-coordinated surface species and the nature of the surface structures, described in **Chapter 4**, makes these two surfaces particularly reactive toward adsorption of arsenate or other impurities.

In contrast, adsorption of arsenate on the Fe-terminated {0001} surface is the least energetically favourable of all the surfaces considered. The Fe-terminated {0001} surface is a stable surface with flat surface structure before adsorption, and as a result the adsorbate has little effect on the surface structure. However, the many interactions between adsorbate and surface still leads to the large energy released upon adsorption.

In all cases, the favourable interactions between the surface and arsenate released large energies upon adsorption, and the process of adsorption includes chemical interaction, leading to strong ionic bonding between the surface species and arsenate, especially on the $\{10\bar{1}1\}a$ surface, where the adsorption leads to saturation of the dangling bonds of oxygen and iron ions.

However, adsorption of arsenate onto the hydroxylated surfaces releases much smaller adsorption energies, listed in **Table 6.1**, because the hydroxylated surfaces are much more stable than their dehydrated counterparts.

The adsorption energies released upon adsorption of arsenate to the series of hydroxylated hematite surfaces are largest on the ($\{10\bar{1}0\}a$, $\{11\bar{2}0\}a$, $\{01\bar{1}2\}a$ and $\{11\bar{2}1\}b$) surfaces. The reason for this preference is due to the relative instability of these surfaces, which have relatively high surface energies when either dehydrated or hydroxylated. This relative instability makes these surfaces more reactive than the other surfaces, which is exemplified by the larger energies released upon adsorption.

6.4 Adsorption to Maghemite

6.4.1 Dehydrated Surfaces

We next inspected the interaction of the arsenate with the dry maghemite surfaces, which were already considered in the study of the interaction with methanoic acid and hydroxyethanal. The adsorption energies of the lowest energy positions for all the surface-adsorbate systems are presented in **Table 6.2**.

Table 6.2: Calculated adsorption energies ($kJmol^{-1}$) for the arsenate molecule at dehydrated and hydroxylated maghemite surfaces.

Surface	**Adsorption energy($kJmol^{-1}$)**	
	Arsenate	
	Dehydrated	**Hydroxylated**
{001}c	-441.1	-43.3
{010}a	-223.3	-46.0
{110}a	-461.7	-49.7
{113}a	-547.3	-94.5
{103}a	-529.0	-93.8

The adsorption of arsenate onto the dominatnt {010}a surface remains the least energetically favourable with an adsorption energy of -223.3 $kJmol^{-1}$, similar to what was seen for the adsorption of the two organic molecules on this surface (**Chapter 5)** .

The arsenate coordinates via it's As to one surface oxygen atom at a distance of ($O_{surface}$…$As_{arsenate}$= 1.72 Å). In addition, the doubly-bonded oxygen atom and one

of the oxygen atoms of the three hydroxyl groups of arsenate are coordinated to two surface iron atoms at distances of 1.94 Å and 2.14 Å respectively, whereas an H atom of arsenate is coordinated to one surface oxygen atom to form a hydrogen-bond of 1.84 Å. The third hydroxyl group of arsenate points away from the surface. **Figure 6.8** shows the relaxed {010}a surface with the adsorbed arsenate molecule .

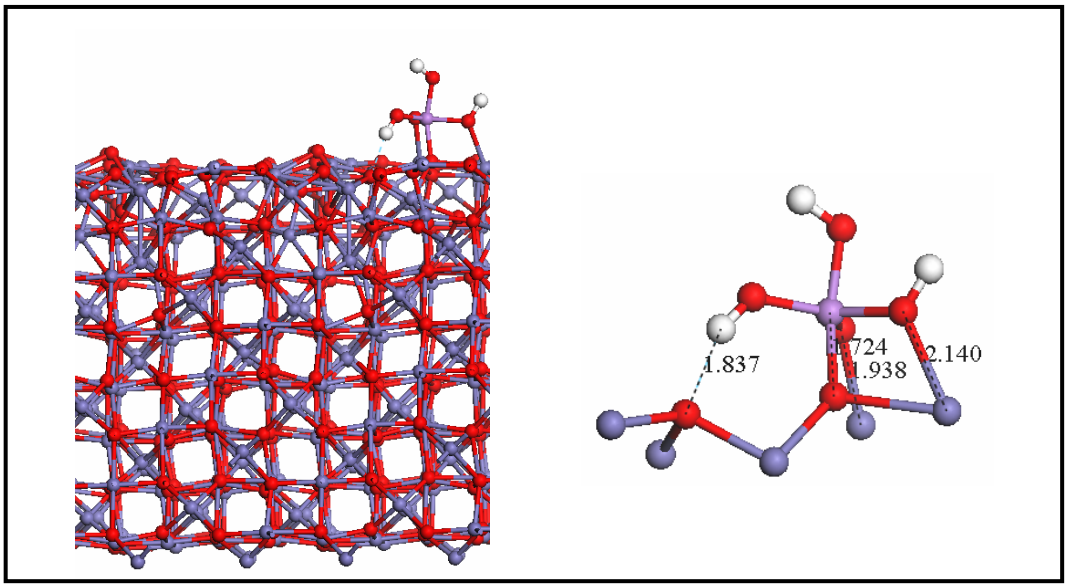

Figure 6.8: Lowest-energy optimised structure of arsenate adsorbed at the dehydrated maghemite {010}a surface, showing interatomic distances (Å) between the adsorbate and surface species. Key: (Iron = blue, Oxygen = red, Arsenate = purple, and the Hydrogen = White).

Similar interactions are seen on the {001}c surface, shown in **Figure 6.9**.

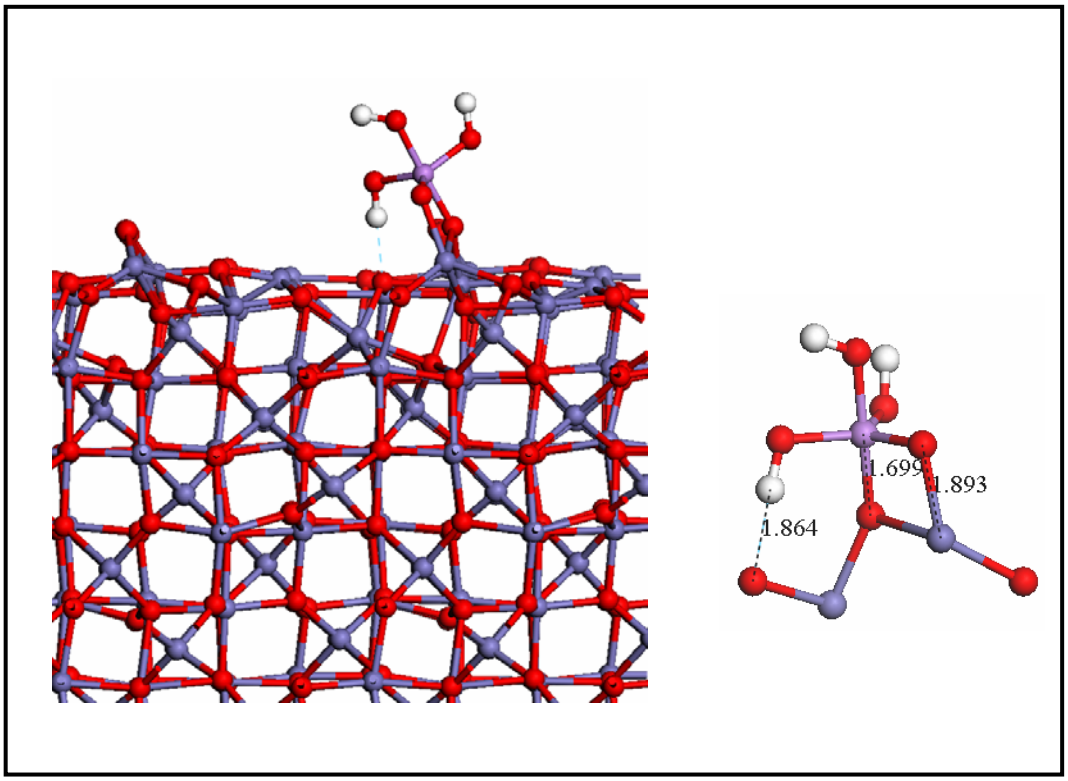

Figure 6.9: Lowest-energy optimised structures of arsenate adsorbed at the dehydrated maghemite {001}c surface, showing interatomic distances (Å) between the adsorbate and surface species. Key: (Iron = blue, Oxygen = red, Arsenate = purple, and the Hydrogen = White).

Similar to the most favourable modes of interaction between the arsenate and the dehydrated hematite surfaces, arsenate prefers to adsorb onto the dehydrated maghemite surfaces through the As which bridges between two surface oxygen atoms, in addition to other interactions between surface species and either the hydroxyl groups or the double-bonded oxygen of arsenate molecule. These kinds of interactions are seen on the most reactive dehydrated maghemite surfaces, the {110}a,{113}a, and {103}a surfaces. Where the lattice spacing between the oxygen atoms is small enough.

In the lowest energy positions arsenate adsorbs onto the{103}a and {113}a surfaces , in the groove running along the surface, which is much more favourable than other positions on these surfaces. The adsorbate's hydroxyl hydrogen atoms and surface oxygen atoms are close enough to allow the arsenate to hydrogen-bond with a surface oxygen atom. **Table 6.3** compares the interatomic distances of the arsenate bound to the {113}a and {103}a surfaces.

Table 6.3: Calculated bond lengths (Å) for the adsorption of arsenate in a "bidentate" mode on dehydrated maghemite {113}a and {103}a surfaces .

Surface	Structure	Bond lengths(Å)
{113}a	As-Fe(surface)	3.04
	As-O1(surface)	1.72
	As-O2(surface)	1.76
	O-Fe1(surface)	1.85
	HO-Fe2(surface)	1.99
	OH-O3(surface)	1.93
{103}a	As-Fe(surface)	3.45
	As-O1(surface)	1.72
	As-O2(surface)	1.80
	O-Fe1(surface)	2.10
	HO-Fe2(surface)	2.14
	OH-O3(surface)	1.90

We can compare the calculated As-O and Fe-O bond lengths and As-Fe distances with distances which obtained from previous experimental work by EXAFS spectroscopy (Sherman & Randall, 2003). For iron (oxyhydr) oxides As-Fe distances of 2.85 Å~3.25 Å identified a bridging bidentate mode with 3.60 Å has

indicating the formation of a monodenate geometry. The As-Fe calculated in this study towards the larger and of the bidentate range and almost intermediate between the two, indicating weak bidentate interaction. In the most favourable configuration (**Figure 6.10**), the arsenate adsorbs onto the {110}a surface in a similar way as observed on the {113}a and {103}a surfaces, but on this surface the distance between the surface oxygen atoms and the arsenate hydrogen atoms is not small enough, and the arsenate is unable to form a hydrogen-bond. The distances observed on this surface between the $O_{surface}$-As-$O_{surface}$ are very small between 1.74 Å -1.75 Å, and its close to As-O bond lengths observed on both {113}a and {103}a surfaces, whereas the O-Fe distance at 1.97 Å and HO-Fe at 2.14 Å again are also very similar. The other two hydroxyl groups point away from the surface.

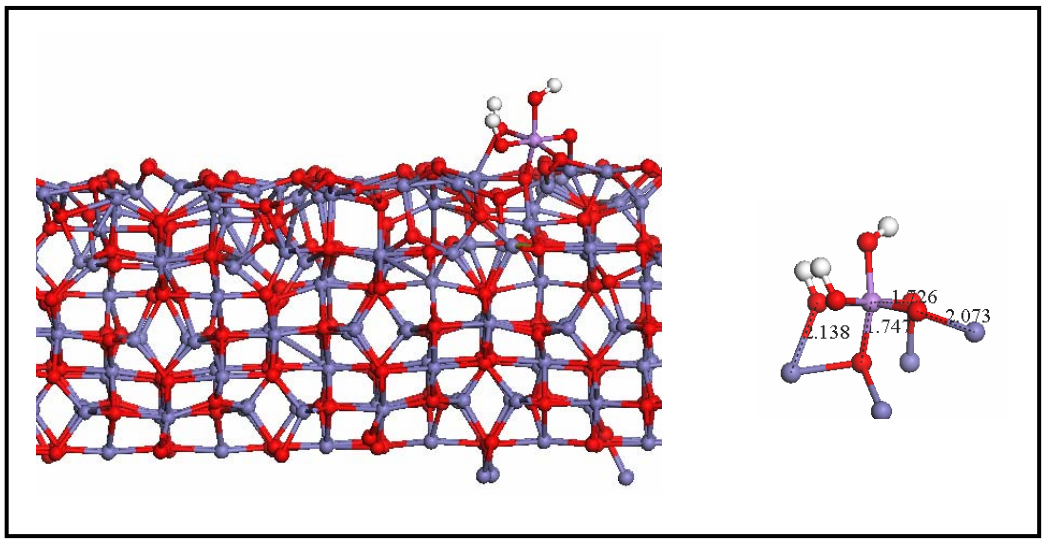

Figure 6.10: Lowest-energy optimised structure of arsenate adsorbed at the dehydrated maghemite {110}a surface, showing interatomic distances (Å) between the adsorbate and surface species. Key: (Iron = blue, Oxygen = red, Arsenate = purple, and the Hydrogen =White).

6.4.2 Hydroxylated Surfaces

Finally, we again explore the effect of hydroxylation of the maghemite surfaces on adsorption behaviour as we have done for the hydroxylated hematite surfaces. We have found that the calculated adsorption energies are highly dependant on the orientation of the molecule on the surface. In many cases, adsorption of the arsenate onto the hydroxylated surface leads to distortion the pattern of the dissociatively adsorbed water molecules. In general, the calculated adsorption energies at the hydroxylated maghemite surfaces are less negative than those on the dehydrated maghemite systems.

In the most favourable mode of adsorption of arsenate on most of the hydroxylated maghemite surfaces one hydroxy group is replaced by the doubly-bonded oxygen atom of arsenate which forms a direct at bond distances ranging from 1.91 Å to 1.96 Å. This kind of interaction is found on all surfaces considered in this study. In addition, the doubly-bonded oxygen atom can also interact with the hydrogen atoms of the surrounding surface hydroxy groups to form hydrogen-bonds, for example at a distance of 2.43 Å, on the {001}c surface, finally the surface is stabilised by hydrogen-bonded interactions between the surface hydroxy groups and the multiple hydrogen and oxygen atoms of the hydroxyl functional groups of arsenate. **Figure 6.11** shows the hydroxylated maghemite {001}a surface, with adsorbed arsenate in lowest energy position with interatomic distances (Å).

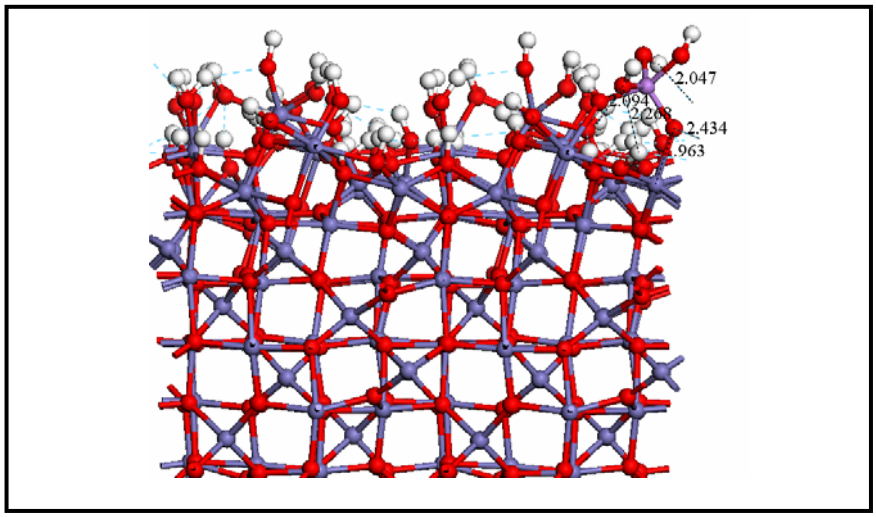

Figure 6.11: Lowest-energy optimised structure of arsenate adsorbed at the hydroxylated maghemite {001}a surface, showing interatomic distances(Å) between the adsorbate and surface species. Key: (Iron = blue, Oxygen = red, Arsenate = purple, and the Hydrogen =White).

6.4.3 Adsorption Energies

The calculated adsorption energies shown in **Table 6.2** for the adsorption of arsenate on all dehydrated maghemite surfaces are all large and negative indicating that the arsenate interacts strongly with all the surfaces. The adsorption energy for the {113}a surface (-547.3 $kJmol^{-1}$) is considerably larger than for the other dehydrated surfaces, due to the lattice spacing between the surface oxygen atoms, which is small enough to allow the arsenate to bridge two surface oxygen atoms. The adsorption energies for the {110}a and {103}a surfaces are also large (-461.7 $kJmol^{-1}$ and -529.1 $kJmol^{-1}$ respectively), again because the lattice spacing between the surface oxygen atoms allows bidentate binding, and the relative instability of these surfaces.

As in the adsorption of both methanoic acid and hydroxyethanal on the {010}a surface, it is energetically the least favourable toward the adsorption of the arsenate, because the large distance between the surface oxygen atoms makes it impossible for the arsenate to bridge two surface oxygen atoms, which as we know leads to a strong interaction between the surface and the adsorbate. The adsorption of arsenate on all dehydrated maghemite surface shows the same trend as seen before for the adsorption of methanoic acid and the two forms of hydroxyethanal on the same surfaces with the only one difference that the adsorption energy for the {113}a surface is now slightly larger than for the {103}a, in contrast to the adsorption of both methanoic acid and hydroxyethanal.

Again, the adsorption energies at the hydroxylated surfaces are smaller than at the more reactive dehydrated surfaces, due to the increased stability of the hydroxylated surfaces and fewer dangling bonds. The negative adsorption energies are due to a number of reasons. Firstly, the arsenate replaces a hydroxy group from the surface, forming a strong bond to Fe, and at the same time the arsenate forms more hydrogen-bonded interactions to the surface than the dissociatively adsorbed water molecules do, which increases the stability of the surface, and a close interaction with the adsorbate.

The adsorption energies on the {001}c, {010}a and {110}a surfaces are very similar and fall in the range of -43 to -50 $kJmol^{-1}$, indicating physisorption of the arsenate onto these surfaces.

6.5 Discussion and Conclusions

In this chapter, we have modelled the adsorption of arsenate onto the same dehydrated and hydroxylated surfaces of hematite and maghemite as were considered in previous chapters of this thesis. From the results we can make the following observations:

- Our simulations show that the strength of the interaction of the arsenate with the surfaces depends on both the stability of the surface and the capability of arsenate to form multiple interactions with the surface species, particularly if the As atom of the arsenate molecule can bridge between two or three surface oxygen atoms.
- We have found that on many hydroxylated surfaces the arsenate replaces one of the surface hydroxy group of the dissociatively adsorbed water molecules which allows to the doubly-bonded oxygen atom of arsenate to form a direct bond with the surface iron atom in that position, as where the Fe-O interaction between the adsorbate oxygen atoms and surface iron atom is similar to the interaction between the Fe-O of the replaced hydroxy group. In addition to the Fe-O interaction the arsenate forms more hydrogen-bonded interactions to the surface than the dissociative water molecules leading to an exothermic reaction when the hydroxy group of dissociative water molecule is replaced.
- On all surfaces considered, the arsenate coordinates to the surface through its doubly-bonded oxygen atom with Fe-O distances ranging from 1.80 Å to 2.08 Å. In addition, there is significant coordination between the oxygen

atoms of the hydroxyl groups of arsenate and one or two of surface iron atoms, with HO-Fe distances of between 1.80 Å to 2.14 Å.

- Generally, the hydrogen-bonding interactions are formed by the coordination of the hydrogen atoms of the hydroxyl groups of arsenate with one or more of the surface oxygen atoms, with H-O distances of between 2.040 Å to 2.50 Å.
- The nature and behavior of adsorbed arsenate species over a wide range of minerals and environmental conditions is fundamental to prediction of the migration and long-term fate of arsenate in natural environments. Spectroscopic experiments and theoretical calculations have demonstrated the potential importance of a variety of arsenate surface species on several iron and aluminum oxides. For example, spectroscopic techniques provide direct experimental observation of ion adsorption mechanisms. Arsenate was observed to form inner-sphere bidentate surface complexes on goethite using infrared (Lumsdon *et al*., 1984), Fourier Transform infrared (FTIR) (Sun & Doner, 1996), and x-ray absorption fine structure (EXAFS) spectroscopy (Waychunas *et al*., 1993; Fendorf *et al*., 1997). Inner-sphere surface complexes of arsenate were also observed on amorphous Fe oxide using FTIR (Suarez *et al*., 1998) and Raman spectroscopy (Goldberg & Johnston, 2001). Arsenite also formed inner-sphere surface complexes on goethite as observed with FTIR (Sun & Doner, 1996) and EXAFS spectroscopy (Manning *et al*., 1998). Adsorption of arsenate on amorphous Al oxide was found to occur as inner-sphere surface complexes using FTIR spectroscopy (Goldberg & Johnston, 2001). Arsenite surface species were observed on amorphous Al oxide using attenuated total reflectance

(ATR)-FTIR spectroscopy (Suarez *et al*., 1998). Parallel studies conducted recently on the mechanism of adsorption of arsenate or arsenite on iron and other oxide surfaces have resulted in different structural models. For example, (Scott *et al*., 1997) have used the Extended X-ray absorption fine structure (EXAFS) spectroscopy to study the local coordination of arsenate on the mineral goethite (R-FeOOH). Based on the As-Fe distance, it was concluded that three different surface complexes exist on goethite a monodentate complex, a bidentate-binuclear complex, and a bidentate-mononuclear complex. The different As-Fe distances were observed, and have shown that the most distance between As-Fe of 3.59 Å is characteristic of linear arrangements, corner sharing tetrahedra-octahedra, resulting from a monodentate surface complex.

Chapter 7

Conclusions and Future work

7.1 Conclusions

In this thesis, we have used atomistic simulation techniques to investigate the adsorption of different pollutants to the surfaces of the two important iron oxide minerals, namely the polymorphs, hematite (α-Fe_2O_3) and maghemite (γ-Fe_2O_3), which have important applications in many areas, including as remedial agents in the soil and catalysts. Firstly, we have compared several interatomic potential models to describe the structures and properties of the four iron oxide polymorphs, α-Fe_2O_3(hematite), β-Fe_2O_3, γ-Fe_2O_3 (maghemite) and ε-Fe_2O_3 to choose a suitable potential for these systems, where we have considered cell volume, angles, Fe-O bond distances and relative stabilities of the four polymorphs, where the calculated lattice energies of the four polymorphs with different sets of potentials all showed that hematite is the most stable polymorph, in agreement with experiment.

In **Chapter 3**, we have investigated the energetics of vacancy ordering in γ-Fe_2O_3 (maghemite), using a statistical approach to evaluate the ordering in a (1x1x3) supercell. Our results show clearly that full vacancy ordering, in a pattern with space group $P4_12_12$, is the thermodynamically preferred situation in the bulk

material. This stability arises from a minimal Coulombic repulsion between Fe^{3+} cation sites for this configuration, which confirm experimental suggestions of an ordered system.

We next extended our study to advance our understanding of the surface chemistry of hematite and maghemite. In **Chapter 4** we have simulated the dehydrated surfaces of both hematite and the ordered model structure for maghemite, where we have used low-index planes and the calculated surface energies of the important experimental surfaces, to determine the thermodynamic morphologies for both minerals. These showed the dominance of the dry hematite surfaces {0001}Fe and $\{01\bar{1}2\}a$, in agreement with their presence as cleavage planes in experimental crystals. The dominant dry maghemite surfaces were the {010}a and {001}a planes with the lowest surface energies but, in this case, we do not have experimental morphology available for comparison. We then investigated the interaction of dissociative water with all the terminations of each surface for both minerals. The simulations of the dry hematite and maghemite surfaces had identified that the stability of the hematite {0001} Fe surface and maghemite {010}a surface is due to the combination of relatively high coordination numbers of the surface species , and for the hematite {0001}Fe surface also the flat surface structure. However, when we add water to the surface, the hydroxylation stabilises all surfaces by increasing the iron- and oxygen-coordination on the surface to more bulk-like coordination environments.

In **Chapter 5** we have modelled the adsorption to the major hematite and maghemite surfaces of two organic molecules as model organic pollutants,

namely methanoic acid and two starting configurations of hydroxyethanal, eclipsed and staggered conformers according to the position of the two oxygen atoms on the hydroxyethanal molecule. We have found that on all dry hematite but only a few maghemite surfaces, the methanoic acid binds to the surface by coordinating to one surface iron atom through the carbonyl oxygen atom, but on a few maghemite surfaces, such as the {103}a surface, the methanoic acid molecule can bridge between two surface iron atoms. The molecule can also interact with the surface through hydrogen-bonding interactions, in most cases between the hydroxyl hydrogen atom of methanoic acid and the surface oxygen atoms, because the carbonyl hydrogen atom of the methanoic acid molecule is generally, directed away from the surface. When we compare the calculated adsorption energies of the methanoic acid and hydroxyethanal molecules to the dry mineral surfaces, we found that the adsorption of the two conformers of hydroxyethanal to all dehydrated surfaces is much stronger than the adsorption of methanoic acid, due to the presence of multiple interactions between the surface and the hydroxyethanal molecule, due to its greater flexibility and span. On the most reactive surfaces, the hydroxyethanal molecule is able to coordinate to the surface by bridging between two surface iron atoms through both carbonyl oxygen atom and hydroxyl oxygen atom. Adsorption of hydroxyethanal is more favourable in the eclipsed configuration where both oxygen atoms can bind to the surface.

Because of the more stable nature of the hydroxylated mineral surfaces, adsorption of organic molecules has is much less exothermic because the interaction is only through relatively weak hydrogen-bonding interactions.

However, the adsorption of hydroxyethanal onto the hydroxylated surfaces is still more favourable than the adsorption of methanoic acid.

Finally, in **Chapter 6** we have modelled the adsorption of the arsenate molecule, a toxic pollutant found in soils and groundwater. We have found that the arsenate molecule can coordinate to the surfaces in a number of different modes. In the most favourable mode at the majority of the dehydrated hematite and maghemite surfaces, the arsenate molecule coordinates to the surface through the As atom bridging between two surface oxygen atoms. In addition, to the doubly-bonded oxygen and one of the hydroxyl oxygen atoms each coordinate to one surface iron atom. On some other surfaces, the As in the molecule interacts with only one surface oxygen atom, in addition to a number of hydrogen-bonded interactions. On a few surfaces, such as the dehydaretd hematite $\{10\bar{1}1\}a$ surface, the arsenate adsorbs through the As which bridges three surface oxygen atoms.

When the arsenate molecule adsorbs onto the hydroxylated surfaces it often replaces one of the hydroxy groups of the dissociatively adsorbed water molecules allowing the doubly-bonded oxygen atom of arsenate to form a bond directly with the surface iron atom in that position, where the Fe-O bond distance between the adsorbate oxygen atoms and surface iron atom is similar to the interaction Fe-O to the surface hydroxy group. In addition to the Fe-O interaction the arsenate forms more hydrogen-bonded interactions to the surface than the dissociated water molecules leading to an exothermic reaction when the hydroxy group of the dissociated water molecule is replaced.

7.2 Future work

Future work could include the adsorption of organic molecules with different functional groups using molecular dynamics simulations to include temperature into the calculation. It would also be interested to investigate the adsorption of As (III) species on the same surfaces, which is the more toxic arsenic species, but first we would need to derive an interatomic potential for this species.

References

Albrecht, T. R., Grütter, P., Horne, D. & Rugar, D. (1991). *Journal of Applied Physics,* 69**,** 668.

Alvarez-Ramírez, F., Martínez-Magadán, J. M., Gomes, J. R. B. & Illas, F. (2004). *Surface Science,* 558**,** 4-14.

Anderson, L., Schreiber, E., Liebermann, R. C. & Soga, N. (1968). *Geophys. Space Phys,* 6**,** 491-524.

Arai, Y., Sparks, D. L. & Davis, J. A. (2004). *Environ. Sci. Technol.,* 38**,** 817-824.

Archuleta, C. M., Demott, P. J. & Kreidenweis, S. M. (2005). *Chem. Phys,* 5, 2617–2634.

Azcue, J. & Nriagu, J. O. (1993). *Environment International,* 19**,** 405-415.

Baltrusaitis, J. & Grassian, V. H. (2005). *Journal Physicas Chemistry, B 109*, 12227-12230.

Bastow, T. J., Trinchi, A., Hill, M. R., Harris, R., Muster, T. H. & (2009). *Journal of Magnetism and Magnetic Materials,* 321**,** 2677-2681.

Bauminger, E. R., Ben-Dor, L., Felner, I., Fischbein, E. & Nowik, I. (1977). *Ofer, S. Physica B,* 86-88**,** 910.

Becker, U., Hochella, M. F. & Apra, E. (1996). *American Mineralogist,* 81**,** 1301-1314.

Ben-Dor, L., Fischbein, E., Felner, I. & Kalman, Z. (1977). *Journal of The Electrochemical Society,* 124**,** 451-457.

Ben-Dor, L., Fischbein, E. & Kalman, Z. (1976). *Acta Crystallographica Section B,* 32**,** 667.

Bergermayer, W., Schweiger, H. & Wimmer, E. (2004). *Physical Review B,* 69.

Berkowitz, A. E., Goehner, R. P., Hall, E. L. & Flanders, P. J. (1985). *Journal of Applied Physics,* 57**,** 3928-3939.

Bertaut, F. (1958). *Compute Rendus,* 246**,** 3447.

Binning, G., Quate , C. F. & Gerber, C. H. (1986). *Phys. Rev. Lett,* 56**,** 930.

Born , M. & Huang, K. (1954). Dynamical Theory of crystal lattice.Oxford University Press: Oxford,England.

Bowen, L. H., De Grave, E. & Vandenberghe, R. E. (1993). Mössbauer Effect Studies of Magnetic Soils and Sediments. In Mössbauer Spectroscopy Applied to Magnetism and Materials ; Long, G. J., Grandjean, F., Eds.; Plenum Press: New York, Science. 1**,** 132−141.

Braun, P. B. (1952). *Nature,* 170**,** 1123

Buckingham, R. A. (1936). *Proc.Royal.Soc,London,* A 168**,** 264.

Burkhard, D. J. M. (1997). *Solid State Communications,* 101**,** 903-907.

Catlow, C. R. A., Corish, J., Hennessy, J. & Mackrodt, W. C. (1988). *Journal of the American Ceramic Society,* 71**,** 42-49.

Chambers, S. A. & Yi, S. I. (1999). *Surface Science,* 439**,** L785-L791.

Chamritski, I. & Burns, G. (2005). *Journal of Physical Chemistry B,* 109**,** 4965-4968.

Chang, J. S., Park, S. E. & Park, M. S. (1997). *Chemistry Letters,* 26**,** 1123.

Cooper, T. G. & De Leeuw, N. H. (2002). *Molecular Simulation,* 28**,** 539-556.

Cooper, T. G. & De Leeuw, N. H. (2003). *Surface Science,* 531**,** 159-176.

Cooper , T. G. & De Leeuw, N. H. (2004). *Langmuir,* 20**,** 3984-3994.

Coustet, V. & Jupille, J. (1994). *Surface Science,* 307-309**,** 1161-1165.

Cox, D., Takei , W., Miller , C. & Shirane , G. (1962). *J. Phys. Chem. Solids,* 23**,** 863-874.

Dauber-Osguthorpe, P., Roberts, V. A., Osguthorpe, D. J., Wolff, J., Genest, M. & Hagler, A. T. (1988). *Proteins: Structure, Function, and Bioinformatics,* 4**,** 31-47.

De Leeuw, N. H. & Cooper, T. G. (2004). *Crystal Growth & Design,* 4**,** 123-133.

De Leeuw, N. H. & Cooper, T. G. (2007). *Geochimica Et Cosmochimica Acta,* 71**,** 1655-1673.

De Leeuw, N. H., Higgins, F. M., Parker, S. C., (1999) *Journal of Physical Chemistry,* B 103**,** 1270-1277.

De Leeuw, N. H. & Parker, S. C. (1997). *Journal of the Chemical Society Faraday Transactions,* 93**,** 467.

De Leeuw, N. H. & Parker, S. C. (1998). *Journal of Physical Chemistry*, B 102**,** **2914**.

Dézsi, I. & Coey, J. M. D. (1973). *physica status solidi (a),* 15**,** 681-685.

Dick, B. G. & Overhauser, A. W. (1958). *Phys.Rev,* 112**,** 90.

Dronskowski, R. (2001). *Advanced Functional Materials,* 11**,** 27-29.

Duffy, D. M. (1986). *Journal of Physics C: Solid State Physics and Chemistry of Minerals,* 19**,** 4394-4412.

Eggleston, C. M., Stack, A. G., Rosso, K. M., Higgins, S. R., Bice, A. M., Boese, S. W., Pribyl, R. D. & Nichols, J. J. (2003). *Geochimica Et Cosmochimica Acta,* 67**,** 985-1000.

Ewald, P. P. (1921). *Annalen der Physik,* 64**,** 253.

Feenstra, R. M. (1994). *Surface Science,* 300**,** 965.

Fendorf, S., Eick, M. J., Grossl, P. & Sparks, D. L. (1997). *Environ. Sci. Technol,* 31**,** 315-320.

Fendorf, S., Eick, M. J., Grossl, P. & Sparks, D. L. (1997). *Environmental Science & Technology,* 31**,** 315-320.

Filgueiras, M. R. T., Mkhonto, D. & De Leeuw, N. H. (2006). *Journal of Crystal Growth,* 294**,** 60-68.

Finch, G. I. & Sinha, K. P. (1957). *Proceedings of the Royal Society of London,Series A:Mathematical and Physical Science,* 241**,** 1-8.

Finger, L. M. & Hazen, R. M. (1980). Crystal structure and isothermal compression of Fe_2O_3,Cr_2O_3,and V_2O_3 to 50 bars. *Geophysical Laboratory,Carnegie Institution of Washington,Washinghton,D.C.20008*.

Fletcher, R. P., M. J. D. (1963). *Computer Journal,* 6**,** 163.

Forestier, H. & Guillot-Guilbin, G. (1934). *Compt.Rend.Acad.Sci.(paris)***,** 199:720.

Fujishiro, Y., Uchida, S. & Sato, T. (1999). *International Journal of Inorganic Materials,* 1**,** 67-72.

Fukushi, K., Sasaki, M., Sato, T., Yanase, N., Amano, H. & Ikeda, H. (2003). *Applied Geochemistry,* 18**,** 1267-1278.

Fuller, C. C. & Davis, J. A. (1989). *Nature,* 340**,** 52-54.

Fysh, S. A. & Clark, P. E. (1982). *Phys Chem Minerals,* 8**,** 257-267.

Gale J.D. (1997). *J Chem Soc Faraday T,* 93**,** 629.

Gale J.D. (2005). *Z. Kristallogr,* 220**,** 552.

Gale, J. D. & Rohl, A. L. (2003). The General Utility Lattice Program (GULP). *Molecular Simulation,* 29**,** 291-341.

Garelick, H., Dybowska, A., Valsami-Jones, E. & Priest, N. (2005). *Journal of Soils and Sediments,* 5**,** 182-190.

Gibbs , J. W. (1928). *Collected works, Longman, New York*.

Gillespie, D. T. & (1977). *Journal of Physical Chemistry,* 81**,** 2340–2361.

Glotch, T. D. & Rossman, G. R. (2009). *Icarus,* 204**,** 663–671.

Godin, T. J. & Lafemina, J. P. (1994). *Physical Review B,* 49**,** 7691-7696.

Goldberg, S. & Johnston, C. T. (2001). *J. Colloid Interface Sci. ,* 234**,** 204–216.

Goniakowski, J. & Gillan, M. J. (1996). *Surface Science,* 350**,** 145-158.

González-Carreño, T., Morales, M. P. & Serna, C. J. (1994). *Journal of Materials Science Letters,* 13**,** 381-382.

Grau-Crespo, R., De Leeuw, N. H. & Catlow, C. R. A. (2003). *Journal of Materials Chemistry,* 13**,** 2848-2850

Grau-Crespo, R., Hamad, S., Catlow, C. R. A. & De Leeuw, N. H. (2007). *Journal of Physics-Condensed Matter,* 19**,** -.

Grau-Crespo, R., Peralta, A. G., Ruiz-Salvador, A. R., Gomez, A. & Lopez-Cordero, R. (2000). *Physical Chemistry Chemical Physics,* 2**,** 5716-5722.

Grau Crespo, R., Catlow, C. R. A. & De Leeuw, N. H. (2007). *Journal of Catalysis,* 248**,** 77-88.

Greaves, C. & (1983). *Journal of Solid State Chemistry,* 49**,** 325-333.

Hafner , J. (2007). *Computer physics communications,* 177**,** 6.

Hagg, G. (1935). *Z. Physik. Chem,* 29B**,** 95-103.

Hartman, P. & Chan, H. K. (1993). *Pharmaceutical Research,* 10**,** 1052-1058.

Haul, R. & Schoon, T. (1939). *Z. Physik. Chem,* 44B**,** 216-226.

Hayward, D. O. (2002). Quantum Mechanics for chemists,Royal Society of Chemistry, 140.

Henderson, M. A., Joyce, S. A. & Rustad, J. R. (1998). *Surface Science,* 417**,** 66-81.

Hendy, S. C., Laycock, N. J. & Ryan, M. P. (2005). *Journal of the Electrochemical Society,* 152**,** B271-B276.

Hering, J. G. & Stumm , W. (1990). *Rev. Miner,* 23**,** 427–465.

Hohenberg, P., Kohn, W. & (1964). *Physical Review B,* B136**,** B864.

Hopenhayn, C. (2006). *Elements,* 2**,** 103-107.

Huang, C. S., Xu, L. & Davis, B. H. (1993). . *Fuel Science & Technology International,* 11(5-6)**,** 639.

Hug, S. J. (1997). *J. Colloid Interface Sci,* 188**,** 415-422.

Ikeda, Y., Takano, M. & Bando, Y. (1986). *Chem. Res., Kyoto Univ,* 64**,** 249.

Jensen, F. (1999). Introduction to Computational Chemistry,. *Denmark,John Wiley and Sons*.

Jessen, S., Larsen, F., Koch, C. B. & Arvin, E. (2005). *Environmental Science & Technology,* 39**,** 8045-8051.

Jiang, K., Yang, J., Hu, B., Yang, X., Mao, L., Yuan, Y. & Zhang, G. (1998). *Hyperfine Interact,* 111**,** 45.

Jolivet, J.-P., Chaneac, C. & Tronc, E. (2004).*Chemical Communications,* 477-483.

Jones, F., Rohl, A. L., Farrow, J. B. & Van Bronswijk, W. (2000). *Physical Chemistry Chemical Physics,* **2,** 3209-3216.

Jorgensen, J. E., Mosegaard, L., Thomsen, L. E., Jensen, T. R. & Hanson, J. C. (2007). *Journal of Solid State Chemistry,* 180**,** 180-185.

Jung, H. & Thomson, W. J. (1993). *Journal of Catalysis,* 139**,** 375-382.

Katsoyiannis, I. A. & Zouboulis, A. I. (2002). *Water Research,* 36**,** 5141-5155.

Koch, W. & Holthausen, M. C. (2000). A Chemist's Guide to Density Functional Theory. .Weinheim.

Kohn, W. & Sham, L. J. (1965). *Physical Review* 140**,** 1133.

Kundu, M. L., Sengupta, A. C., Maiti, G. C., Sen, B., Ghosh, S. K., Kuznetsov, V. I., Kustova , G. N. & Yurchenko, E. N. (1988). *Journal of Catalysis,* 112**,** 375-383.

Lado-Touriño , I. & Tsobnang, F. (2000). *Computational Materials Science,* 17**,** 243-248.

Leach, A. R. (1996). Molecular Modelling,Principles and Applications,. *Harlow,Addison Wesley Ongman ltd*.

Lefevre, G. (2004). *Adv. Colloid Interface Sci,* 107**,** 109–123.

Lefevre, G. & Fedoroff, M. (2006). *Phys. Chem. Earth,* 31**,** 499-504.

Lei, Y., Cant, N. W. & Trimm, D. L. (2005). *Catalysis Letters,* 103**,** 133-136.

Leist , U., Ranke , W. & K., A.-S. (2003). *Physical Chemistry Chemical Physics,* 5, 2435-2441.

Levy, M., Wilhelm, C., Siaugue, J. M., Horner, O., Bacri, J. C. & Gazeau, F. (2008). *Journal of Physics-Condensed Matter,* 20.

Lewis, G. V. & Catlow, C. R. A. (1985). *Journal of Physics C-Solid State Physics,* 18**,** 1149-1161.

Lide, D. R. (2000). *CRC Handbook of Chemistry and Physics, CRC, Boca Raton,USA*

Liebermann, R. C. & Schreiber, E. (1968). *J. geophys. Res,* 73**,** 6585-6590.

Linge, K. L. & Oldham, C. E. (2004). *Applied Geochemistry,* 19**,** 1377-1389.

Liu, Q., Ma, W., He, R. & Mu, Z. (2005). *Catalysis Today,* 106**,** 52-56.

Lo, C. S., Tanwar, K. S., Chaka, A. M. & Trainor, T. P. (2007). *Physical Review B,* 75.

Lumsdon, D. G., Fraser, A. R., Russell, J. D. & Livesey, N. T. (1984).

Mackrodt, W. C. (1992). *Philos. Trans. R. Soc. London ,,* A341**,** 301.

Maeda, Y. (1978). *Techn .Publ,* 179**,** 1-7.

Manassidis, I. & Gillan, M. J. (1994). *Journal of the American Ceramic Society,* 77**,** 335-338.

Manassidis, I. & Gillan, M. J. (1994). *Journal of the American Ceramic Society,* 77**,** 335-338.

Manceau , A.(1995). *Geochim. Cosmochim. Acta.,* **59,** 3647-3653.

Manning, B. A., Fendorf, S. E. & Goldberg, S. (1998). *Environ. Sci. Technol.,* 32**,** 2383–2388.

Maruyama, T. & Kanagawa, T. (1996). *Journal of The Electrochemical Society,* 143**,** 1675-1677.

Mendoza, E. A., Sunil, D., Wolkow, E., Gafney, H. D., Rafailovich, M. H., Sokolov, J., Long, G. G., Jemian, P. R., Schwartz, S. A. & Wilkens, B. J. (1990). *Applied Physics Letters,* 57**,** 209-211.

Meskhidze, N., Chameides, W. L., Nenes, A. & Chen, G. (2003). *Geophysical Research Letters,* 30.

Mimura, N., Takahara, I. & Ando, M. (1998). *Catal.Today,* 45**,** 61.

Mitra, S. (1992). *Applied Mössbauer Spectroscopy, Series:Physics and Chemistry of the Earth; Pergamon: Oxford,* 18**,** 67−72, 313−343.

Mkhonto, D. & De Leeuw, N. H. (2002). *Journal of Materials Chemistry,* 12**,** 2633-2644.

Mkhonto, D., Ngoepe, P. E., T.G., C. & De Leeuw, N. H. (2006). *Physics and Chemistry of Minerals,* 33**,** 314-331.

Morse, P. M. (1929). *Physical Review,* 34(1)**,** 57.

Morsi, M. M. & El-Shennawi, A. W. A. (1993). *Ceramics International,* 19**,** 333-338.

Murad , E. & Schwertmann, U. (1986). *Clays and Clay Minerals,* 34.,No.1**,** 1-6.

Nakamori, T. & Shibuya, A. (1990). *Jpn. Kokai Tokkyo Koho***,** 3 pp, patent

Nygren, M. A., Gay, D. H. & Catlow, C. R. A. (1997). *Surface Science,* 380**,** 113-123.

Ozaki, M. & Matijevic, E. (1985). *Journal of Colloid and Interface Science,* 107**,** 199-203.

Pacchioni, G., Ferrari, A. M., Bagus, P. S. & (1996). *Surface Science,* 350**,** 159-175.

Pankhurst, Q. A., Connolly, J., Jones, S. K. & Dobson, J. (2003). *Journal of Physics D-Applied Physics,* 36**,** R167-R181.

Parker, S. C., De Leeuw, N. H. & Redfern, S. E. (1999). *Faraday Discuss,* 144, 381-393.

Parr, R. G. & Yang, W. (1989). Density-functional theory of atoms and molecules.New York.

Parry, D. E. (1975). *Surface Science,* 49**,** 433.

Parry, D. E. (1976). *Surface Science,* 54**,** 195.

Pauling , L. & Hendricks, S. (1925). *Journal of American Chemical Society,* 47**,** 781-790.

Payne , M. C., Teter , M. P., Allan , D. C., Arias , T. A. & Joannopulos, J. D. (1992). *Reviews of Modern Physics,* 64**,** 1045.

Pecharroman, C., Gonzales-Carreno, T. & Iglesias, J. E. (1995). *Phys. Chem. Miner,* 22**,** 21-29.

Pichler, T. & Veizer, J. (1999). *Chemical Geology,* 162**,** 15-31.

Pugh, S., Gillan, M. J. & . 320 (1994). *Surface Science,* 320**,** 331-343.

Puls, M. P., , W., C.H. & Norgett, M. J. (1977). *Philosophical Magazine,* 36**,** 1457-1472.

Quate, C. F. (1994). *Surface Science,* 299/300**,** 980.

Randall S. R., S. D. M., And & V., R. K. (2001). *Geochim. Cosmochim. Acta,* **65,** 1015-1023.

Redhead, P. A. (1962). *Vacuum,* 12**,** 203-211.

René P Schwarzenbach., P. M. G., Dieter M Imboden (2003). Environmental organic chemistry . New York [u.a.] Wiley

Rohrbach, A., Hafner, J. & Kresse, G. 2004. *Physical Review B,* 70**,** 125426.

Rohrer, H. (1994). *Surface Science,* 299/300**,** 956.

Rustad, J. R., Wasserman, E. & Felmy, A. R. (1999). *Surface Science,* 424**,** 28-35.

Sakaguchi, I., Yurimoto, H. & Sueno, S. (1992). *Solid State Communications,* 84**,** 889-893.

Schrader, R. & Büttner, G. (1963). Eine neue Eisen(III)-oxidphase: ϵ-Fe2O3. *Zeitschrift für anorganische und allgemeine Chemie,* 320**,** 220-234.

Schroer, P., Kruger, P. & Pollman, J. (1994). *Physical Review,* B 49**,** 17092-17101.

Schwertmann, U. & Cornell , R. M. (2003). The Iron Oxides structure , Properties , Reactions , Occurences and Uses .Wiley-VCH.

Sherman D.M., A. & S.R., R. (2003). *Geochim,Cosmochim .Acta,* 67, 4223-4230.

Sherman, D. M. & Randall, S. R. (2003). *Geochimica Et Cosmochimica Acta,* 67**,** 4223-4230.

Shin, H.-S. (1998). *Yoop Hakoechi,* 35**,** 1113-1119.

Shirane, G., Pickart, S. J., Nathans , R. & Ishikawa, Y. (1959). *Journal of Physics and Chemistry of Solids,* 10**,** 35-43.

Shmakov, A. N., Kryukova, G. N., Tsybulya, S. V., Chuvilin, A. L. & Solovyeva, L. P. (1995). *Journal of Applied Crystallography,* 28**,** 141-145.

Somogyvari, Z., Svab, E., Meszaros, G., Krezhov, K., Nedkov, I., Sajo, I., Bouree, F. & (2002). *Applied Physics a-Materials Science & Processing,* 74**,** S1077-S1079.

Stumm , W. (1992). *Chemistry of the Solid–Water Interface,* . John Wiley and Sons.

Stumm, W. (1997). *Colloids Surf,* A 120**,** 143–166.

Suarez, D. L., Goldberg, S. & Su, C. (1998). *Am. Chem. Soc. Symp. Ser. ,* 715**,** 136–178.

Suber, L., Imperatori , P., Ausanio , G. & Fabbri, F., Hofmeister , H. (2005). *J. Phys. Chem,* B 109**,** 7103–7109.

Sun, X. & Doner, H. E. (1996). *Soil Sci,* 161**,** 865–872.

Syvinski, W. & Mccarthy, G. (1990). *North Dakota State University, Fargo, ND, ICDD Grant-in-Aid*.

Tasker, P. W. (1979). *Philosophical Magazine a-Physics of Condensed Matter Structure Defects and Mechanical Properties,* 39**,** 119-136.

Thirunavukkarasu, O. S., Viraraghavan, T. & Subramanian, K. S. (2003). *Water, Air, & Soil Pollution,* 142**,** 95-111.

Trainor, T. P., Chaka, A. M., Eng, P. J., Newville, M., Waychunas, G. A., Catalano, J. G. & Brown, G. E. (2004). *Surface Science,* 573**,** 204-224.

Trautmann, J. M. & Forestier, H. (1965). *Compt. Rend.,* 261**,** 4423.

Tronc, E., Chanéac, C. & Jolivet, J. P. (1998). *Journal of Solid State Chemistry,* 139**,** 93-104.

Twigg, M. V. (1989). *Catalyst Handbook Wolfe Publishing,* London.

Van Hien, N., Kolchanov, V. A., Ryzhonkov, D. I. & Filipov, S. I. (1971). *Izv . Vyssh. Ucheb. Zaved., Chern. Met.,* 14**,** 5.

Van Oosterhout, G. W. & Rooijmans, C. J. M. (1958). *Nature,* 181**,** 44.

Vandenberghe, R. E., De Grave, E., Landuydt, C. & Bowen, L. H. (1990). *Hyperfine Interactions,* 53**,** 175-195.

Verwey, E. J. W. (1935). *Z. Krist. A,* 91**,** 65-67.

Vitre, R. D., Nelson, B. & Tessier, A. (1991). *Limnology and Oceanography,* 36**,** 1480-1485.

Wang, J. & Rustad, J. R. (2006). *Geochimica Et Cosmochimica Acta,* 70**,** 5285-5292.

Wasserman, E., Rustad, J. R. & Felmy, A. R. (1999). *Surface Science,* **424,** 19-27.

Wasserman, E., Rustad, J. R., Felmy, A. R., Hay, B. P. & Halley, J. W. (1997). *Surface Science,* 385**,** 217-239.

Watanabe, H. & Seto, J. (1988). *Bulletin of the Chemical Society of Japan,* 61**,** 3067-3072.

Watson, G. W., Kelsey, E. T., Deleeuw, N. H. & Harris, D. J. P., S. C. (1996). *J Chem Soc Faraday T,* T 92**,** 433-438.

Waychunas G. A., D. J. A., And & C., F. C. (1995). *Geochim. Cosmochim. Acta,* **59,** 3655-3661.

Waychunas G. A., F. C. C., Rea B. A., And & A., D. J. (1996). *Geochim. Cosmochim. Acta,* **60,** 1765-1781.

Waychunas G. A., R. B. A., Fuller C. C., And & A., D. J. (1993). *Geochim. Cosmochim. Acta,* **57,** 2251-2269.

Waychunas, G. A. & (1991). Crystal chemistry of oxides and oxyhydroxides. In: Lindsley, D. H. (ed.) Oxide Minerals petrolic and magnetic significance. Miner. Soc. Am.

Waychunas, G. A., Rea, B. A., Fuller, C. C. & Davis, J. A. (1993). *Geochim. Cosmochim.Acta* 57**,** 2251–2269.

Wiarda, D., Wenzel, T., Uhrmacher, M. & Lieb, K. P. (1992). *Journal of Physics and Chemistry of Solids,* 53**,** 1199-1209.

Wiarda, D. & Weyer, G. (1993). *Int. J. Mod. Phys. B,* 7**,** 353.

Wiemann, J. A., Carpenter, E. E., Wiggins, J., Zhou, W. L., Tang, J. K., Li, S. C., John, V. T., Long, G. J. & Mohan, A. (2000). *Journal of Applied Physics,* 87**,** 7001-7003.

Woodley, S. M., Battle, P. D., Gale, J. D. & Catlow, C. R. A. (1999). *Physical Chemistry Chemical Physics,* 1**,** 2535-2542.

Wulff, G. (1901). *Z. Kristallogr. Kristallgeom,* 34**,** 449.

Xiong, Y., Ye, J., Gu, X. & Chen, Q. (2008). *Journal of Magnetism and Magnetic Materials,* 320**,** 107-112.

Xu, L., Bao, S., O'brien, R. J., Houpt, D. J. & Davis, B. H. (1994). *Fuel Science & Technology International,* 12(10)**,** 1323-53

Zboril, R., Mashlan, M. & D., K. (1999). The Mechanism of β-Fe_2O_3 Formation by Solid-State Reaction between NaCl and $Fe_2(SO_4)_3$. In Mössbauer Spectroscopy in Materials Science;Miglierini, M., Petridis, D., Eds.;Kluwer Academic Publishers: Dordrecht. 49-56.

Zboril, R., Mashlan, M., Krausova, D. & Pikal, P. (1999). *Hyperfine Interact,* 121-122**,** 497.

Zscherpel, D., Weiss, W. & Schlogl, R. (1997). *Surf. Sci,* 382**,** 326.